

AD-A084 029

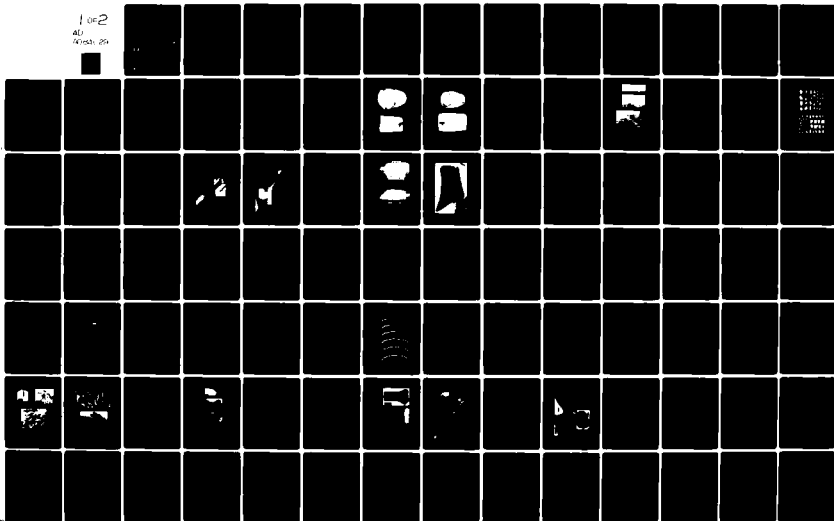
SRI INTERNATIONAL MENLO PARK CA F/G 12/1  
DEVELOPMENT AND APPLICATION OF A COMPUTATIONAL SHEAR BAND MODEL--ETC(U)  
MAR 80 D C ERLICH, L SEAMAN, D A SHOCKEY DAAD05-76-C-0762

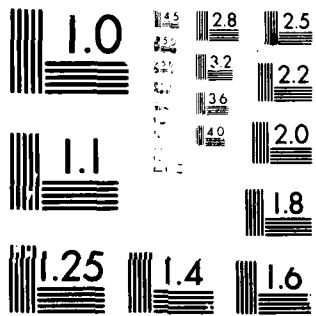
UNCLASSIFIED

ARBRL-CR-00416

NL

1 of 2  
AD  
000000 20





MICROCOPY RESOLUTION TEST CHART  
NATIONAL BUREAU OF STANDARDS-1963-A

AV-E 430 412

# LEVEL

III  
A

12

AD

ADA 084029

CONTRACT REPORT ARBRL-CR-00416

## DEVELOPMENT AND APPLICATION OF A COMPUTATIONAL SHEAR BAND MODEL

Prepared by

SRI International  
333 Ravenswood Avenue  
Menlo Park, CA 94025

March 1980

DTIC  
ELECTE  
MAY 6 1980  
S B D



US ARMY ARMAMENT RESEARCH AND DEVELOPMENT COMMAND  
BALLISTIC RESEARCH LABORATORY  
ABERDEEN PROVING GROUND, MARYLAND

Approved for public release; distribution unlimited.

DDC FILE COPY

80 4 18 017

Destroy this report when it is no longer needed.  
Do not return it to the originator.

Secondary distribution of this report by originating  
or sponsoring activity is prohibited.

Additional copies of this report may be obtained  
from the National Technical Information Service,  
U.S. Department of Commerce, Springfield, Virginia  
22151.

The findings in this report are not to be construed as  
an official Department of the Army position, unless  
so designated by other authorized documents.

*The use of trade names or manufacturers' names in this report  
does not constitute indorsement of any commercial product.*

UNCLASSIFIED

SECURITY CLASSIFICATION OF THIS PAGE (When Data Entered)

REPORT DOCUMENTATION PAGE		READ INSTRUCTIONS BEFORE COMPLETING FORM
1. REPORT NUMBER CONTRACT REPORT ARBRL-CR-00416	2. GOVT ACCESSION NO. AD-A084029	3. RECIPIENT'S CATALOG NUMBER
4. TITLE (and Subtitle) DEVELOPMENT AND APPLICATION OF A COMPUTATIONAL SHEAR BAND MODEL	5. TYPE OF REPORT & PERIOD COVERED Final Report 7 Apr 76 - 7 Apr 77	
	6. PERFORMING ORG. REPORT NUMBER PYU 5084	
7. AUTHOR(s) D. C. Erlich, L. Seaman, D. A. Shockey, and D. R. Curran	8. CONTRACT OR GRANT NUMBER(s) DAAD05-76-C-0762 <sup>NEW</sup>	
9. PERFORMING ORGANIZATION NAME AND ADDRESS SRI International 333 Ravenswood Avenue Menlo Park, CA 94025	10. PROGRAM ELEMENT, PROJECT, TASK AREA & WORK UNIT NUMBERS	
11. CONTROLLING OFFICE NAME AND ADDRESS US Army Armament Research and Development Command US Army Ballistic Research Laboratory (DRDAR-BL) Aberdeen Proving Ground, MD 21005	12. REPORT DATE MARCH 1980	
	13. NUMBER OF PAGES 117	
14. MONITORING AGENCY NAME & ADDRESS (if different from Controlling Office)	15. SECURITY CLASS. (of this report) UNCLASSIFIED	
	15a. DECLASSIFICATION/DOWNGRADING SCHEDULE	
16. DISTRIBUTION STATEMENT (of this Report)  Approved for public release; distribution unlimited.		
17. DISTRIBUTION STATEMENT (of the abstract entered in Block 20, if different from Report)		
18. SUPPLEMENTARY NOTES		
19. KEY WORDS (Continue on reverse side if necessary and identify by block number) Shear Banding Fragmenting Rounds Long-Rod Penetrators Oblique Rod Impact		
20. ABSTRACT (Continue on reverse side if necessary and identify by block number) A computational shear band model has been developed and used to predict the fragmentation response of explosively-loaded cylinders and munitions. The model is based on the physical processes occurring in the material that lead to fragmentation, as observed in experiments in which the fragmentation process was stopped at various stages of development. Good agreement was obtained between measured and computed fragment size distributions for two widely different steels, which suggests that the model can be used to predict		

DD FORM 1473 1 JAN 73 EDITION OF 1 NOV 65 IS OBSOLETE

UNCLASSIFIED

SECURITY CLASSIFICATION OF THIS PAGE (When Data Entered)



## CONTENTS

LIST OF ILLUSTRATIONS	v
LIST OF TABLES	vii
ACKNOWLEDGMENTS	ix
I SUMMARY	1
II INTRODUCTION AND OBJECTIVES	3
III SHEAR BAND MODEL DEVELOPMENT - EXPERIMENTAL PHASE	5
A. Contained Fragmenting Round Experimental Technique	5
B. Experimental Results - Shear Band Nucleation	9
C. Experimental Results - Shear Band Orientation, Growth, and Coalescence	16
D. Conclusions and Recommendations	30
IV SHEAR BAND MODEL DEVELOPMENT - COMPUTATIONAL PHASE	31
A. Derivation of the Model	31
1. Nucleation	32
2. Growth	37
3. Effects of Damage	38
4. Stress-Strain Relations	42
B. Simulations of Fragmenting Round Experiments	44
C. Conclusions and Recommendations	55
V OBLIQUE ROD IMPACT - EXPERIMENTAL PHASE	59
A. LLL Experiments	59
B. SRI Experiments	63
C. BRL Experiments	65
D. Conclusions	69
VI OBLIQUE ROD IMPACT - COMPUTATIONAL PHASE	71
A. Code Modifications	72
B. Simulations	76
APPENDIX A: EQUIVALENT PLASTIC STRAIN FOR A RADIALLY EXPANDING CYLINDRICAL TUBE	87
APPENDIX B: USE OF THE SHEAR BANDING SUBROUTINE IN WAVE PROPAGATION CALCULATIONS	91
REFERENCES	113

## ILLUSTRATIONS

1.	Cross-Section Diagram of Contained Fragmenting Round Experiments	7
2.	HF-1 Steel Cylindrical Tube Damaged in Shot 5084-2	10
3.	HF-1 Steel Cylindrical Tube Damaged in Shot 5084-3	11
4.	Outlines of HF-1 Steel Tube Walls Before and After Deformation in Contained Fragmenting Round Experiments	13
5.	Incipient Shear Band Formation in HF-1 Steel Showing (a) Surface Dimpling, (b) Initial Shear Motion at a Dimpling Site, and (c) Subsequent Growth	14
6.	HF-1 Steel Fragments Recovered from (a) Shot 5084-4 and (b) Shot 5084-5	17
7.	Fragment Size Distributions from (a) Shot 5084-4 and (b) Shot 5084-5	18
8.	Geometry and Nomenclature for Shear Bands in Cylindrical Round Experiments	19
9.	Detailed Photomicrograph of Crack 9A on Cut 7, with Inset Showing High Magnification of Shear Band Region	21
10.	Detailed Photomicrograph of Crack 3A on Cut 4, Showing Various Relationships Between Shear Banding and Subsequent Cracking	22
11.	HF-1 Steel Fragment from Shot 5084-4 Selected for Use in Quantitative Shear Band Study, Photographed from (a) Direction A and (b) Direction B	24
12.	Composite Photomicrographs of Cut 4, Showing Various Positions and Orientations of Shear Bands and Cracks within HF-1 Fragment	25
13.	Depth Distributions of Shear Bands in HF-1 Steel Fragment	27
14.	Shear Band Depth ( $d$ ) Versus Displacement ( $B$ ) Data	28
15.	Shear Band Length ( $L$ ) Versus Depth ( $d$ ) Data	29
16.	Four Cylindrical Fragmenting Round Configurations Treated with SRI PUFF and the Shear Band Model	46
17.	Schematic of Crowe's Sample Fragmenting Projectile	47
18.	Comparison of Experimental and Computed Fragment Size Distributions for HF-1 and Armco Iron Cylinders	48

19.	Cell Layout for Two-Dimensional Simulation of Crowe's Sample Fragmenting Projectile	51
20.	Progress of Detonation and Shear Band Damaged Computed in the Two-Dimensional Simulation of Crowe's Sample Fragmenting Projectile	52
21.	Comparison of Computed and Observed Fragment Size Distributions for Crowe's Sample Fragmenting Projectile	53
22.	Specimen (a) from Distal End of Obliquely Impacted Tool Steel Long-Rod Penetrator Fired at Lawrence Livermore Laboratory with Photomicrographs (b) and (c) Showing Shear Banding	60
23.	Photomicrographs of Distal Half of Obliquely Impacted Tungsten Alloy Long-Rod Penetrator Showing (a) Undeformed Region, (b) Region of Primarily Homogeneous Shear Deformation, and (c) Region of Large Inhomogeneous Shear Deformation Resulting in Shear Crack	61
24.	Fragment (a) Recovered from Obliquely Impacted Tungsten Alloy Long-Rod Penetrator Fired at Lawrence Livermore Laboratory with Photomicrographs Showing Evidence of Large Homogeneous (b) and Nonhomogeneous (c) Shear Deformations	63
25.	HF-1 Steel Long-Rod Projectiles Recovered from Oblique Impact Tests at SRI	65
26.	Polished Section (a) Through BRL Tungsten Alloy Long-Rod Penetrator, with Close-Up (b) of Shear Band	66
27.	Detailed Photomicrographs of Shear Band in BRL Tungsten Alloy Long-Rod Penetrator	67
28.	Polished Section (a) Through Fragment from BRL Tungsten Alloy Long-Rod Penetrator Impact, with Close-ups (b) and (c) of Shear-Banding Regions	69
29.	Sliding or Sticking Conditions at Oblique Target	73
30.	Geometry for Simulations of Projectile Plate Impacting a Wall at an Oblique Angle	77
31.	Distortion and Damage near Front of Projectile Plate for 30° Obliquity, No Slipping	78
32.	Distortion and Damage near Front of Projectile Plate for 30° Obliquity, Slipping	79
33.	Distortion and Damage near Front of Projectile Plate for 45° Obliquity, No Slipping	80

34.	Distortion and Damage near Front of Projectile Plate for 45° Obliquity, Slipping	81
35.	Distortion and Damage near Front of Projectile Plate for 55° Obliquity, No Slipping	82
36.	Distortion and Damage near Front of Projectile Plate for 55° Obliquity, Slipping	83
37.	Force Transmitted by the Impacting Plate as a Function of Distance Along the Plate	85
38.	Bending Moments in the Impacting Plate as a Function of Distance Along the Plate	86
39.	Geometry and Nomenclature for Equivalent Plastic Strain Derivation	88
40.	Sample Output from SHEAR2 for Four Cells Containing Shear Band Damage	102
41.	Input Data for Four Cylindrical PUFF Calculations of Fragmenting Rounds Including Shear Banding	105
42.	Listing of Subroutine SHEAR2	107

#### TABLES

1.	Contained Fragmenting Round Experimental Parameters	8
2.	Shear Stress Components Acting on Shear Band Planes	35
3.	Definition of Formal Parameters in SHEAR2	94
4.	Input Data for SHEAR2	96

#### ACKNOWLEDGMENTS

The authors are grateful to G. Moss and J. Zukas of BRL, R. Crowe of NSWC, and J. Mescall of AMMRC for useful technical discussions; J. Scudder and L. Hoard of LLL for providing us with penetrator fragments; C. G. Hayes, B. Lew, R. E. Tokheim, and R. Trottier for computational assistance; P. De Carli and R. W. Gates for designing and performing the rod impact experiments; D. Petro for preparing the metallographic specimens; and A. F. Rehbock for preparing and firing the contained fragmenting round experiments.

## I SUMMARY

A computational shear band model has been developed and used to predict the fragmentation response of explosively-loaded cylinders and munitions. To provide a basis for the model, an experimental technique was developed for arresting the dynamic expansion of exploding cylinders at desired loads (see Figure 1). The technique was used to infer the phenomenology and to obtain quantitative data for shear instabilities. Shear instabilities were found to nucleate and to grow in HF-1 steel at equivalent plastic strains of about 15% and 30%, respectively. Shear instability surfaces are roughly semicircular, and the surface displacement is proportional to the depth of the shear band surface (see Figure 14).

The computational model for shear instabilities was used in conjunction with a two-dimensional wave propagation code to compute fragment size distributions from exploding cylinders. The model produces fragments by accounting for the nucleation, growth, and coalescence of shear bands according to mathematical expressions inferred from experimental observations and data. Shear surfaces form anisotropically in the deforming material according to the three-dimensional strain state; moreover, as the shear surfaces form, they relax the stresses. The resulting fragment size distributions (Mott plots) are obtained by summing the contributions from all the computational cells.

Four fragmenting cylinder experiments and one fragmenting projectile experiment differing in material, geometry, and explosive, were simulated computationally (see Figures 16 and 17). Good agreement was obtained between computed and observed fragment size distributions (see Figures 18, 20, and 21). These results indicate the basic correctness of the model and suggest that the model can account for effects of variation of geometry, strain rate, and pressure. Further model development should

focus on early stages of shear band nucleation and growth, and on the stress-strain relations of shear-banded material.

Metallographic examination of fragments from HF-1 and tungsten-nickel-iron long-rod penetrators showed that shear banding was a principal mode of projectile failure under oblique and normal impact conditions (see Figures 22 and 27). Computational simulations with the two-dimensional wave propagation code TROTT were made of a plate impacting on edge a second plate at angles of  $30^{\circ}$ ,  $45^{\circ}$ , and  $55^{\circ}$ . Both high tensile and high shear stresses are produced near the impacting edge of the projectile plate, indicating potential fracture and shear banding regions. These stresses are significantly larger if no slippage occurs between the impacting surfaces. Future computations should be performed with shear banding and fracture subroutines and the results should be compared with metallographic observations of impacted projectiles.

## II INTRODUCTION AND OBJECTIVES

Shear banding, the development of internal regions of intense plastic strain, is a prominent mechanism of deformation and fracture leading to the disintegration of exploding rounds, long-rod penetrators, and armor plates.<sup>1</sup> The Ballistics Research Laboratory, the Navy Surface Weapons Center, and the Advanced Research Projects Agency are therefore seeking to acquire an understanding of the phenomenon, and have contracted SRI to develop a computational model that can be used to predict the failure behavior of ordnance structures and materials by this mechanism. The model could be used to predict results of given projectile/target encounters and the effectiveness of fragmenting rounds in given scenarios, thus allowing more accurate vulnerability and lethality assessments. Furthermore, a computational shear band model would be useful in the design of improved weapons and armors and in the development of improved ordnance materials.

SRI efforts to construct a shear band model began in 1974 under contract with the Naval Surface Weapons Center.<sup>2</sup> The resulting model, called SNAG for Shear Nucleation and Growth, treated the competing work-hardening and thermal-softening effects of plastically deforming material, and included plastic threshold strain, shear band velocity, and critical internal energy as parameters. Reasonable predictions of the fragmentation behavior of cylinders of HF-1 steel and Armco iron were realized. The goal of the research program described here was to refine this preliminary model and apply it to compute the fragmentation behavior of exploding rounds and long-rod penetrators.

Our approach was to:

- Conceive and perform experiments in which shear bands were produced and arrested at various stages of their development.

- Observe shear band phenomenology and make quantitative measurements of such properties as shear band numbers, sizes, and spacings.
- Develop a computational model incorporating mathematical expressions describing shear band behavior.
- Incorporate the shear band model in wave propagation codes.
- Test the model by computationally simulating experiments and comparing computed and measured results.

The following section describes the interrupted exploding cylinder experiments and presents the resulting data on shear band behavior. Section IV describes development of a computational model based on the observations and data from Section III. Metallographic evidence for shear band activity in long-rod penetrators is presented in Section V, and Section VI presents two-dimensional slab-slab impact calculations indicating the distribution of shear, bending, and tensile stresses expected in obliquely impacting rods.

### III SHEAR BAND MODEL DEVELOPMENT - EXPERIMENTAL PHASE

Our goal for this phase of the program was to devise experimental techniques that would allow us to study the shear banding phenomena from nucleation through growth to coalescence and ultimate fragmentation, and to quantitatively measure parameters that would be important in any realistic predictive model.

We devised the "contained fragmenting round" technique that enabled us to load HF-1 cylinders at pressures and strain rates high enough to induce shear banding, but to contain the cylinder in such a manner as to arrest the shear banding process at a level before full fragmentation occurs. We were then able to examine the material metallographically, observe the shear bands, and relate them to the loading histories.

In the following paragraphs, we discuss the experimental techniques in greater detail, examine the results from the experiments, and draw conclusions regarding the shear banding process.

#### A. Contained Fragmenting Round Experimental Technique

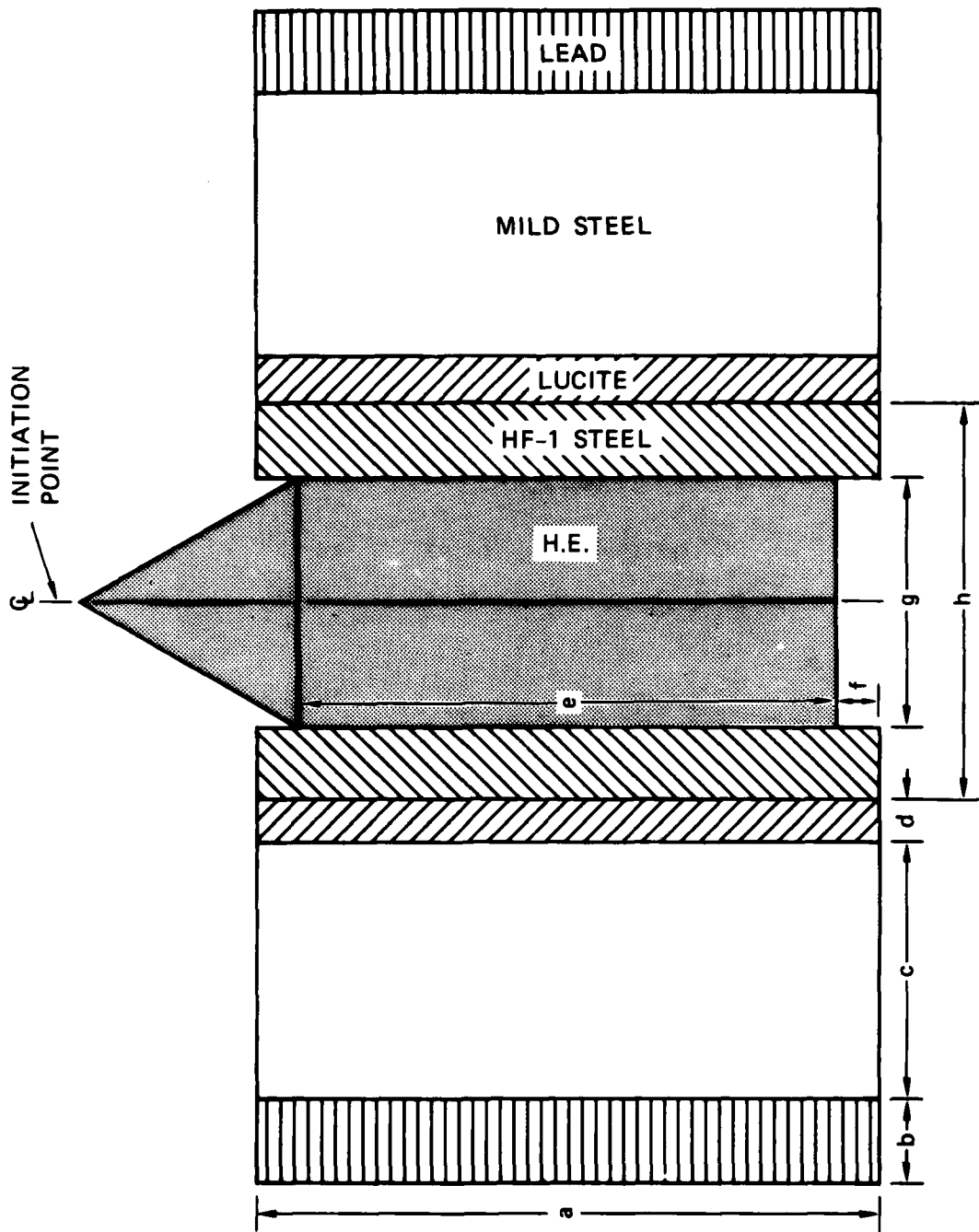
To study the shear banding process through its nucleation-growth-coalescence cycle, we needed a technique somewhat analogous to the plate-impact technique developed at SRI for study of ductile and brittle fracture.<sup>3</sup> The latter technique allows independent variation of tensile stress magnitude and duration, which are the principal parameters controlling the nucleation and growth of ductile voids or brittle cracks. For shear banding, we expected that the principal controlling parameters would be shear strain magnitude and duration, or alternatively, shear strain and strain rate. Thus, we needed a method that would apply a known shear load on a specimen and then remove the load after a known time.

We chose a cylindrical geometry, as it appeared to us to be the simplest geometry for producing shear bands and also the most relevant to the fragmenting round problem.

The geometry is shown schematically in Figure 1. Dimensions and other parameters are given in Table 1. The specimen material is HF-1 steel, a material that has been used in naturally fragmenting rounds as well as in previous shear banding studies. The HF-1 steel tubes were provided by the Naval Surface Weapons Center.<sup>4</sup>

The specimen tube is filled with a high explosive and detonated through an H.E. cone to produce a relatively planar detonation wave through most of the tube. The high internal pressures from the H.E. deform the tube outward, inducing a state of strain that has a large compressive radial component, a large tensile hoop component, and a negligible axial component (ignoring end effects). We thus have a state of high shear strain.

The specimen tube is surrounded by a series of concentric containment pipes. The relatively thin-walled, soft Lucite buffer tube allows the specimen tube to expand radially and prevents a sharp high-pressure impact with the main containment tube, which is a very thick-walled mild steel pipe. The outermost lead tube serves as a momentum trap; it is pre-cut in the axial direction to enable it to fly off in several pieces in the radial direction, taking most of the radial momentum with it and reducing the inward-going tensile wave. Because of the thickness of the containment tubes, the specimen tube experiences no radial tensile stress for at least 40  $\mu$ sec, by which time the internal pressures produced by the H.E. are greatly reduced, due to escape of explosive gases from the open ends of the tube. The lack of radial tensile stresses inhibits brittle fracture, leaving shear banding as the predominant failure mode.



MA-5084-9

FIGURE 1 CROSS-SECTION DIAGRAM OF CONTAINED FRAGMENTING ROUND EXPERIMENTS  
 Letters refer to dimensions used in Table 1.

Table 1

## CONTAINED FRAGMENTING ROUND EXPERIMENTAL PARAMETERS

Dimensions (cm)	Shot No.			
	5084-2	5084-3	5084-4	5084-5
HF-1 steel tube				
I.D. (g)	7.68	7.68	7.68	7.68
O.D. (h)	12.07	12.07	12.07	12.07
Length (a)	18.73	19.05	19.05	18.42
Lucite sleeve				
thickness (d)	1.27	1.27	2.86	1.27
Steel containment pipe				
wall thickness (c)	7.94	7.94	6.35	7.94
Lead thickness (b)	2.54	2.54	2.54	2.54
Explosive column				
Length (e)	17.78	13.97	14.60	12.06
Setback (f)	0	2.54	2.22	2.22
Explosive parameters				
H.E. used	PETN/ $\mu$ -spheres †	Nitro- methane	PETN/ $\mu$ -spheres	PETN/ $\mu$ -spheres
Explosive density (gm/cm <sup>3</sup> )	0.98	1.135	1.05	1.34
Expected detonation				
Velocity (mm/ $\mu$ sec)	5.45	*	5.75	6.9
Pressure (kbar)	75	*	90	160

Note: (a)-(h) refer to dimensions shown in Figure 1.

\* Data uncertain due to impurities in nitromethane, but was similar to that in Shot No. 5084-2.

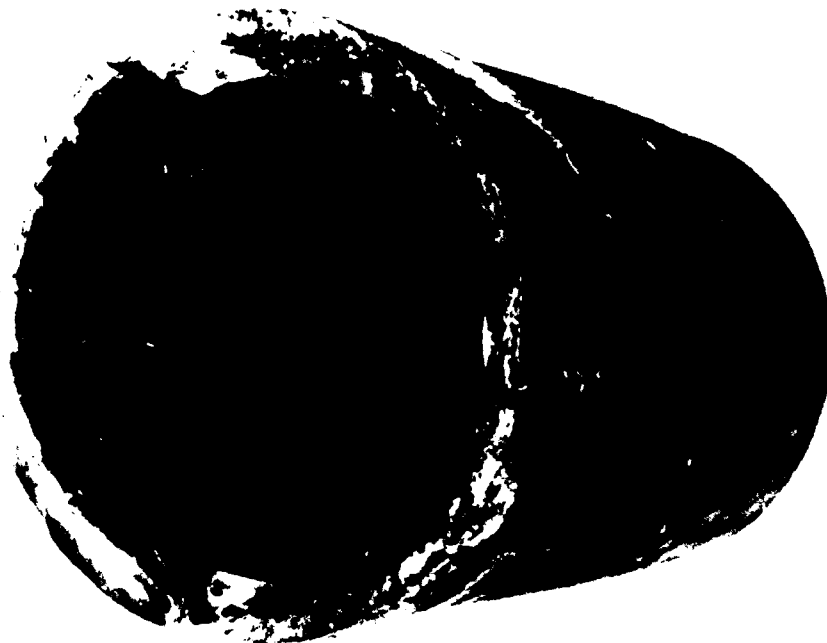
† Pentaerythritol tetranitrate ( $C_5H_8O_{12}N_4$ )/hollow plastic micro-spheres manufactured by Emerson & Cuming, Inc., Canton, Mass.; - 2%  $\mu$ -spheres by weight.

The strain and strain rate to which the specimen tube is subjected can be varied by changing the explosive mixture and the thickness of the Lucite buffer tube. A higher pressure detonation will induce higher strain rates in the specimen tube, and a thicker buffer will allow the specimen tube to attain larger strains. However, the controlling parameters are not orthogonal with respect to the material response parameters. For example, a higher detonation pressure will produce larger strains even if the buffer tube thickness remains the same. Furthermore, there is a complicated pattern of stress waves and reflections while the various containment tubes are "ringing up" to their peak pressures and then unloading. Hence, the loading history of the specimen tube cannot be predicted easily without the aid of computer simulations.

#### B. Experimental Results - Shear Band Nucleation

After running several computer simulations (using Cylindrical PUFF), and one proof test using a 4142 steel specimen tube (so as not to deplete our limited supply of HF-1 steel) to establish the geometry of the experiment, we performed four contained fragmenting cylinder experiments with HF-1 steel, as shown in Table 1.

The first two experiments (Shots 2 and 3) resulted primarily in incipient shear band formation, while the latter two (Shots 4 and 5) resulted in substantial shear band growth and partial fragmentation. The specimen tube recovered from Shot 2 is shown in Figure 2. The partially fragmented shear lip and substantial shear cracking at the upper end of the tube is caused by the large axial strain resulting from the H.E. extending axially to the very edge of the tube. Such end effects were eliminated in subsequent shots by setting the H.E. back from the tube edge. The tube recovered from shot 3, shown in Figure 3, exhibits a radial deformation that is greater near the center



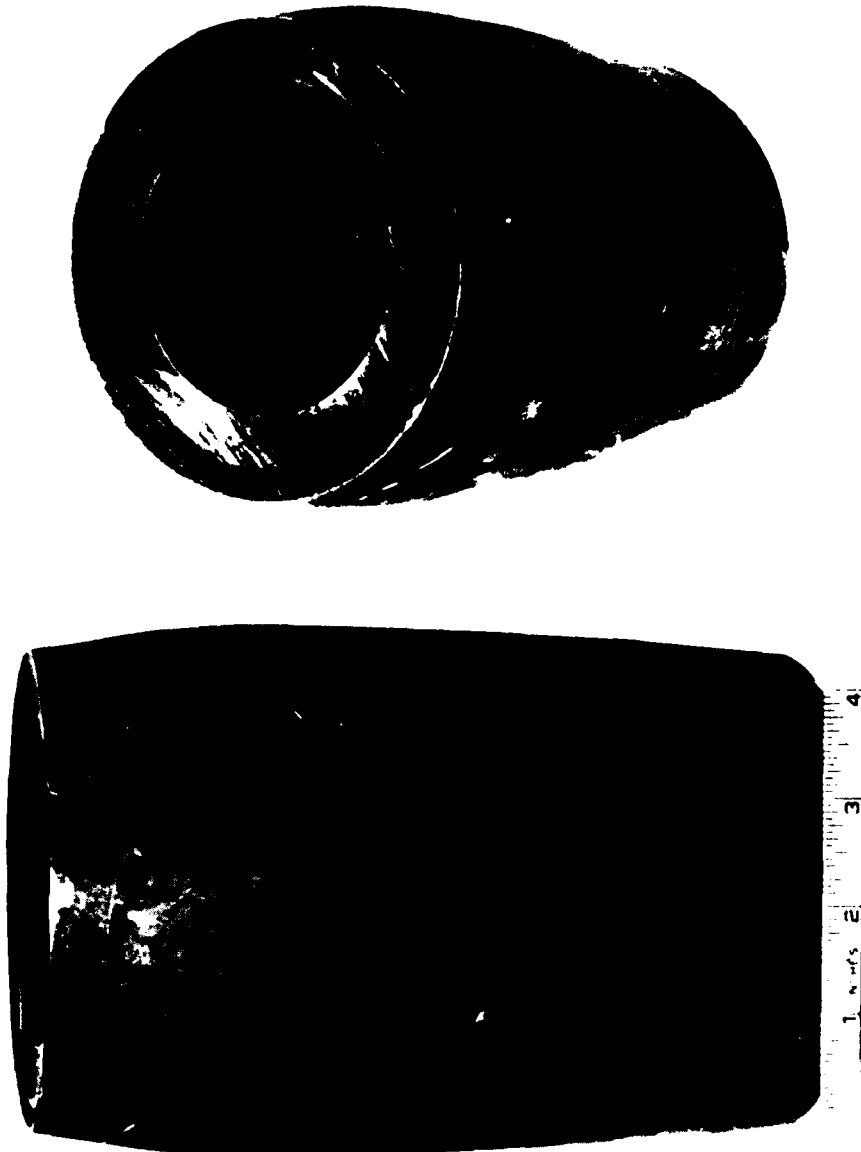
(b) TOP VIEW

MP-5084-2



(a) SIDE VIEW

FIGURE 2 HF-1 STEEL CYLINDRICAL TUBE DAMAGED IN SHOT 5084-2



(a) SIDE VIEW

(b) TOP VIEW

MP-5084-3

FIGURE 3 HF-1 STEEL CYLINDRICAL TUBE DAMAGED IN SHOT 5084-3

of the tube than at the ends because of the explosive set-back and because the internal pressure at the center remains high for a longer period of time.

The wall thickness and diameter of the recovered tubes were measured as a function of axial position and plotted to show the final shapes as shown in Figure 4. The equivalent plastic strain undergone by the tube at different axial positions was then calculated assuming negligible axial strain. A definition of equivalent plastic strain and details of this calculation can be found in Appendix A. Equivalent plastic strain was selected as a parameter relevant to the shear banding process that could be compared with computer simulations. For Shot 3, the strain at the position of maximum deformation was  $\approx 28\%$ .

Other than the edge effect damage discussed above, the only visible sign of material failure in Shots 2 and 3 was the presence of minute axial striations on the inner tube surface, as can be seen in Figures 2(b) and 3(b). These striations appear after the tubes have deformed to an equivalent plastic strain of  $\approx 15\%$  and often extend for an inch or more along the cylinder axis. We hypothesized that these striations are the sites for subsequent shear banding. To test the hypothesis, we made a cut in the tube recovered from Shot 3, perpendicular to the cylinder axis near the point of maximum deformation. Photomicrographs of the polished and etched surface are shown in Figure 5, and these pictures clearly show the incipient stages of shear band formation. The first stage appears as surface striations, as the material experiences non-uniform radial deformation. Further radial expansion causes shear motion to concentrate at the striations. Once this nonuniform shear deformation has begun, the local material becomes hotter and weaker, and the shear band continues to propagate into the material along the  $45^\circ$  plane of maximum shear stress, provided that the internal pressures remain high enough to continue radial expansion. The material along the

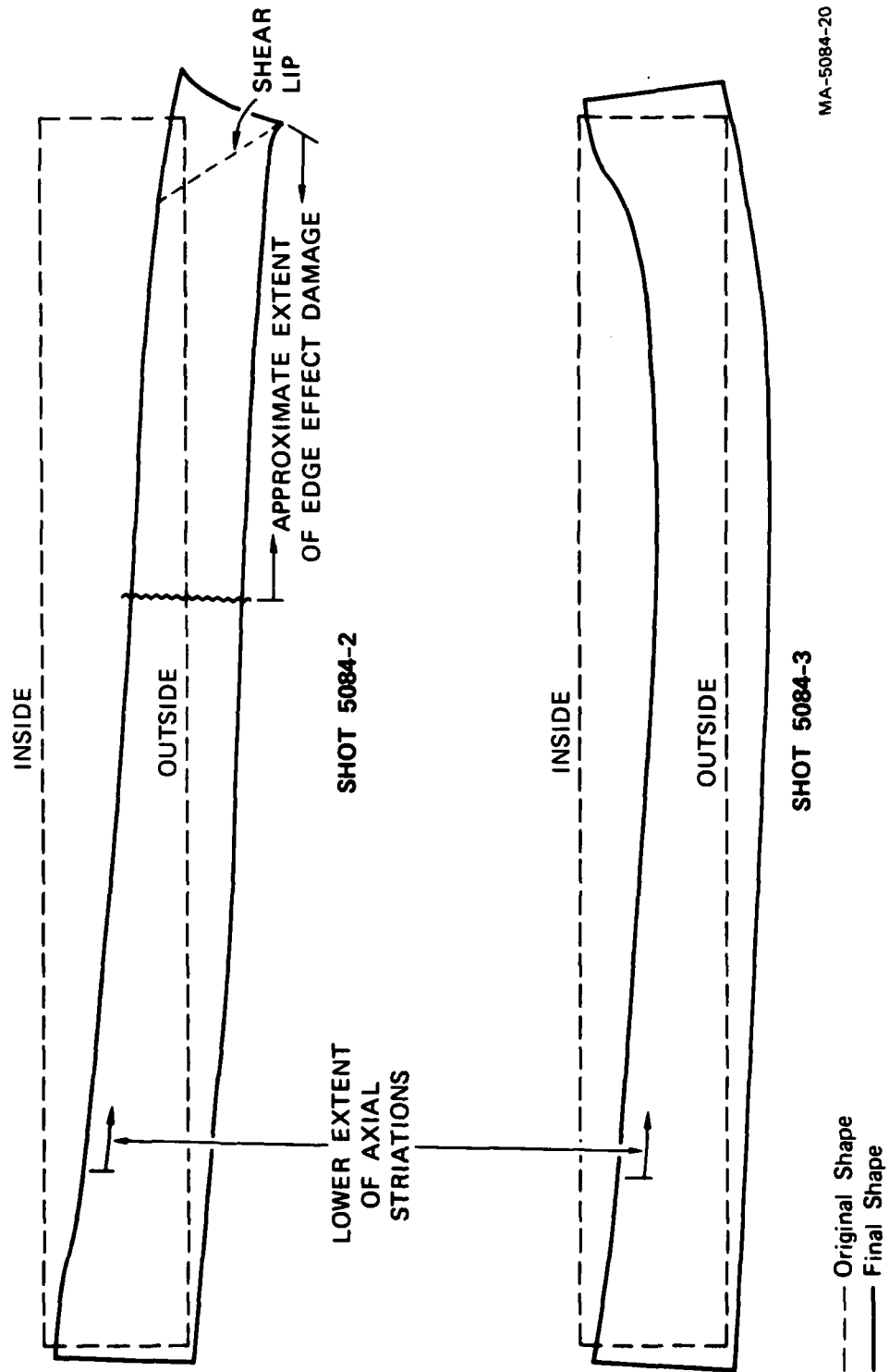


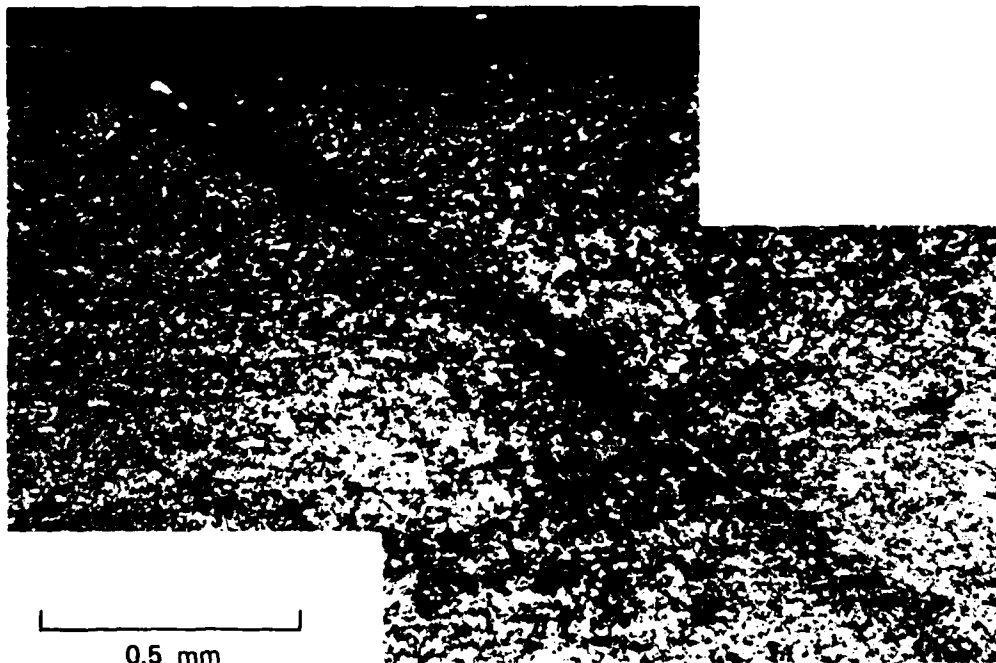
FIGURE 4 OUTLINES OF HF-1 STEEL TUBE WALLS BEFORE AND AFTER DEFORMATION IN CONTAINED FRAGMENTING ROUND EXPERIMENTS



(a)



(b)



(c)

MP-5084-15

**FIGURE 5** INCIPIENT SHEAR BAND FORMATION IN HF-1 STEEL SHOWING (a) SURFACE DIMPLING, (b) INITIAL SHEAR MOTION AT A DIMPLING SITE, AND (c) SUBSEQUENT GROWTH

shear band has a reduced tensile strength, so that subsequent tensile stresses can produce a crack in the shear-banded zone, as seen in Figure 5(c).

Other cuts were made in the HF-1 steel tubes recovered from Shot 3 and from the regions of Shot 2 unaffected by edge effect damage, but metallographic observation revealed no damage other than the type shown in Figure 5--incipient shear band formation and band growth to a depth of only a few millimeters. Thus we can conclude that in this geometry and at the strain rates produced by H.E. detonation pressures on the order of 100 kbar, shear bands begin to nucleate at equivalent plastic strains greater than  $\approx 15\%$ , but have not grown to significant size (the size where coalescence or fragmentation may take place) at equivalent plastic strains of 28%.

### C. Experimental Results - Shear Band Orientation, Growth, and Coalescence

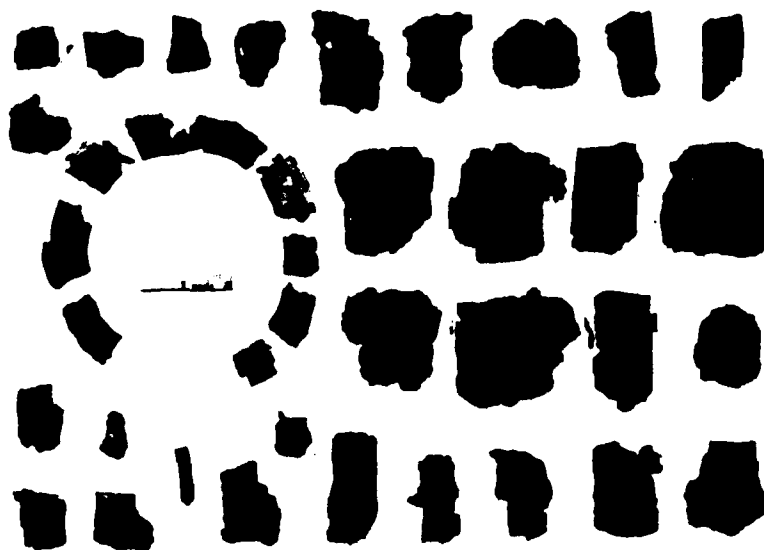
Contained fragmenting round experiments 4 and 5 resulted in much greater levels of damage to the specimen tube than the earlier shots. This was caused by higher detonation pressures of the H.E. (Shot 5) or by thicker Lucite buffer tubes (Shot 4). In both cases the containment system was not strong enough to keep the specimen tube intact. As a result, the HF-1 steel fragmented into many relatively large pieces, most of which were recovered. Figure 6 is a photograph of recovered fragments from Shots 4 and 5; recovered fragment size distributions are shown in Figure 7. (The equivalent radius ( $R_E$ ) is the radius of a sphere having the same mass as the fragment.)

Figure 8 depicts cylindrical tube elements containing shear bands of the three possible orientation types for cylindrical symmetry. For every shear band, the material on one side of the band slips with respect to the material on the other side. If a shear band intersects a material surface, part of the slip plane is exposed above the surface (the shaded regions in Figure 8). We define  $l$  as the length of this exposed region, or, more generally, as the length of the band in the direction perpendicular to the slip direction. If we cut the material along a plane perpendicular to the shear band length, we see the band edge-on and can define the parameters  $d$  as the depth of the band in the slip direction, or the average depth of the material on opposite sides of the band, and  $B$  as the shear displacement or slip magnitude at the surface. ( $B$  corresponds to Burger's vector in atomic dislocation theory.)

For orientation type 1,  $l$  is in the axial direction; for type 2,  $l$  is in the circumferential direction; and for type 3,  $l$  is in the radial direction. Within each orientation type, there are two possible directions-- $90^\circ$  with respect to each other--representing planes of shear strain symmetry. All six of these directions represent slip along planes of maximum shear strain. For a radially expanding



(a)

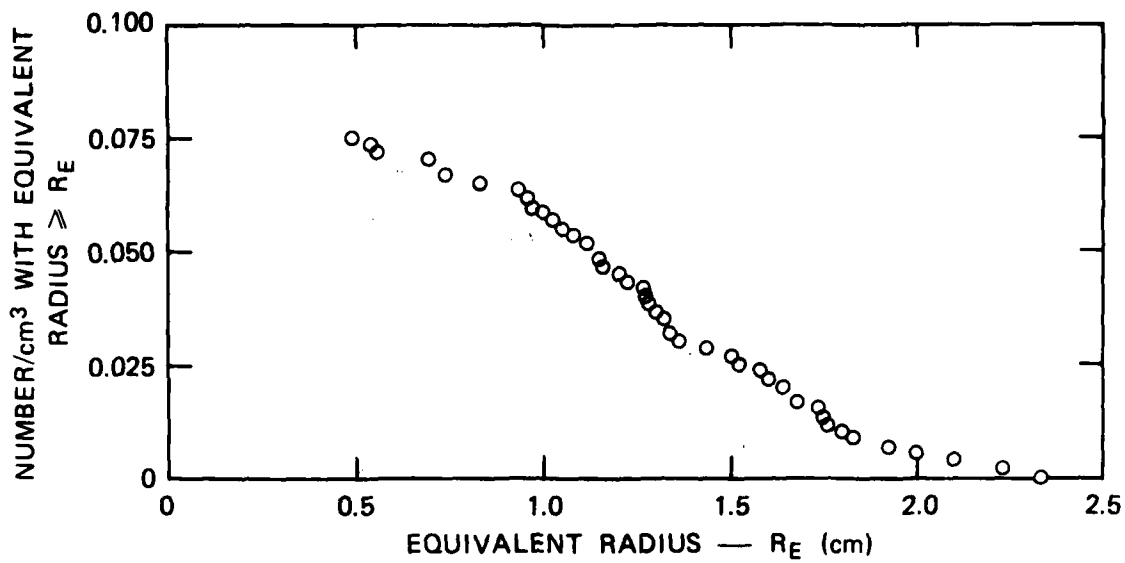


(b)

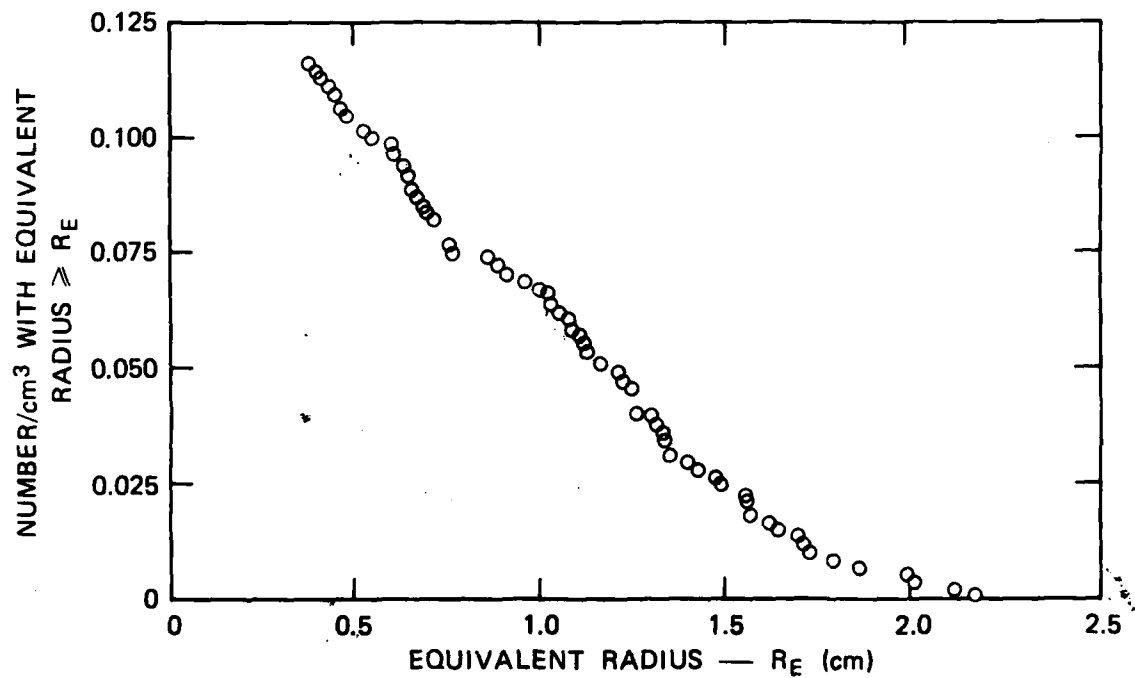
MP-5084-4

FIGURE 6 HF-1 STEEL FRAGMENTS RECOVERED FROM (a) SHOT 5084-4 AND (b) SHOT 5084-5

Arrow shows fragment used for quantitative shear band study.



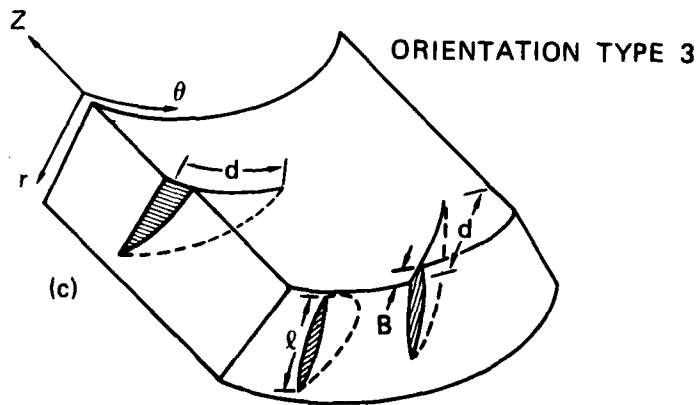
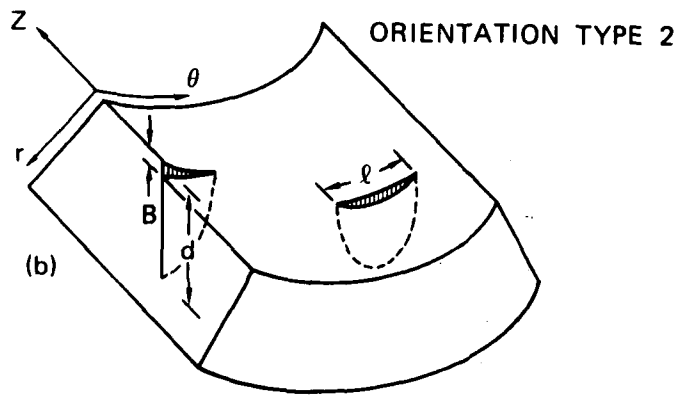
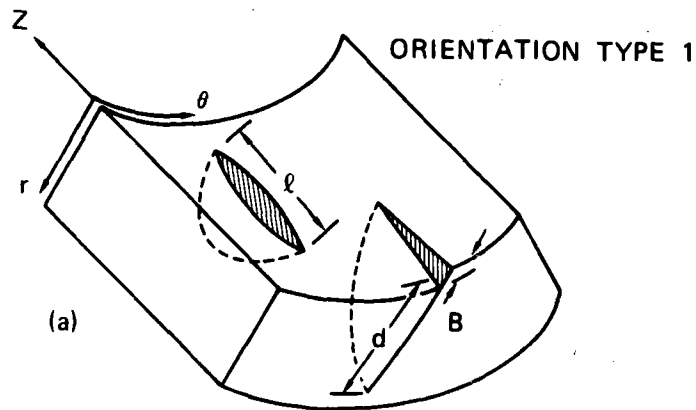
(a)



(b)

MA-5084-13

FIGURE 7 FRAGMENT SIZE DISTRIBUTIONS FROM (a) SHOT 5084-4 AND (b) SHOT 5084-5



- |          |  |
|----------|--|
| $l$      | – Length in Direction<br>Perpendicular to<br>Slip Motion |
| $d$      | – Depth Along $45^\circ$<br>Slip Plane                   |
| $B$      | – Shear Displacement<br>Along Slip Plane                 |
| $Z$      | – Axial Direction  |
| $r$      | – Radial Direction                                       |
| $\theta$ | – Circumferential<br>Direction                           |

FIGURE 8 GEOMETRY AND NOMENCLATURE FOR SHEAR BANDS IN CYLINDRICAL ROUND EXPERIMENTS

MA-5084-21

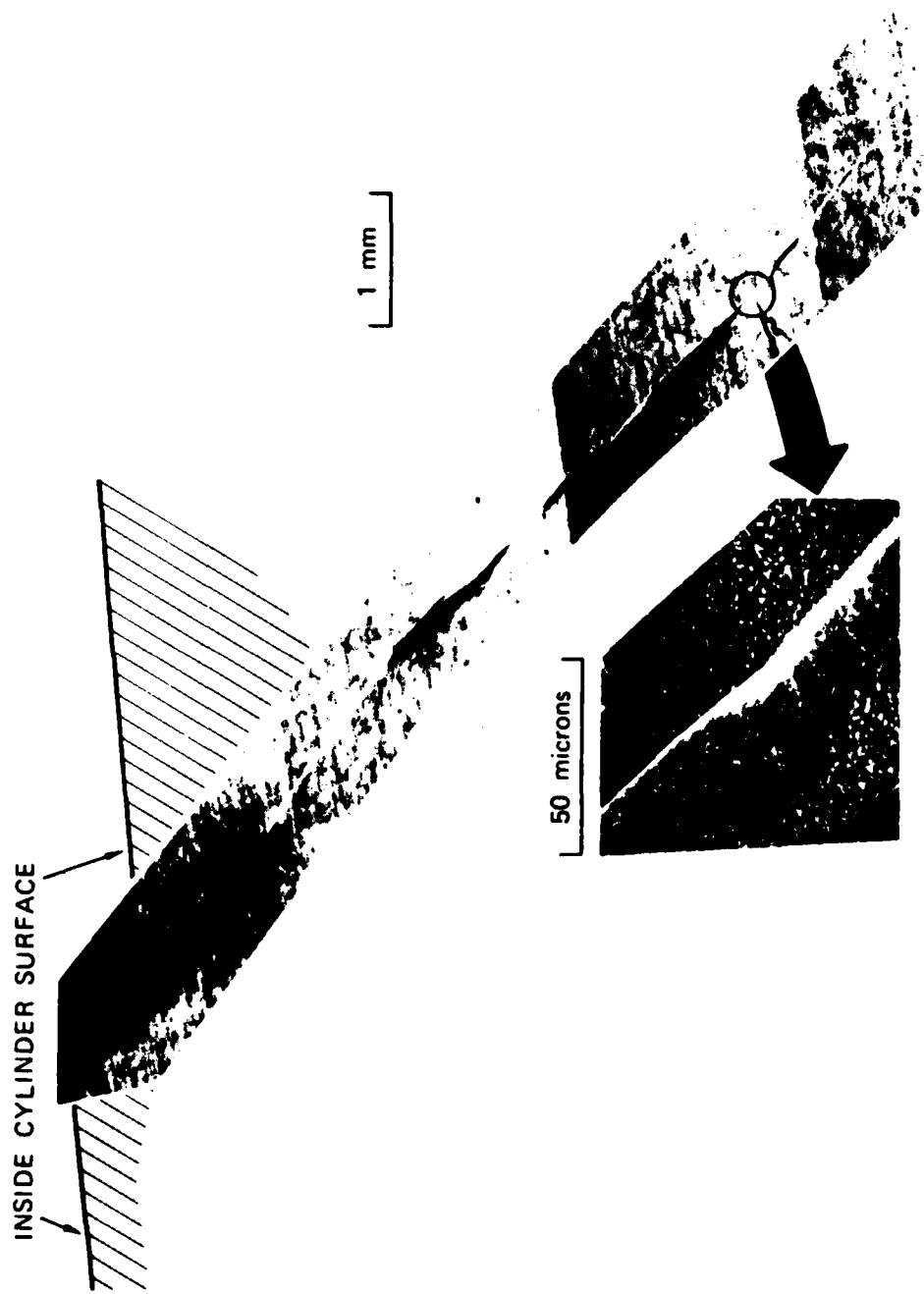
cylindrical tube, the largest of these shear strains are in the plane perpendicular to the axial direction, so shear bands of orientation type 1 are predominant in the fragmenting cylinder experiments. Type 1 accounts for all of the shear band damage in Shot 4, as well as most of the damage in Shot 5.

Figure 9 shows a band\* that, for much of its length, has not separated in tension, although the material on opposite sides of the transformed band has slipped distances that are orders of magnitude greater than the  $\approx 5\text{-}\mu$  band thickness. Large displacements, therefore, do not in themselves cause the shear band to crack. Figure 10, on the other hand, shows a band that has almost completely separated. This separation occurs sometimes entirely within the transformed band, sometime adjacent to the band but parallel to it, and sometimes across the band at a slight angle. Whether a crack lies entirely within a shear band is probably determined by the time elapsed between band formation and subsequent tensile failure. If the hot shear band has had time to be quenched by the surrounding material and thus regain some of its strength, the crack will more likely lie partially outside the band. In any case, shear cracking is seen only in the vicinity of shear banding in the fragmenting cylinder experiments, and so for the quantitative damage assessment discussed below, shear bands and shear cracks are considered the same.

The fragments recovered from Shot 4 were created almost entirely by the shear banding process; the lateral edges of the fragments were all shear bands of orientation type 1. The fragments recovered from Shot 5, on the other hand, showed shear band damage only in the region from the inner surface to about halfway through the wall thickness, and showed

---

\*The band appears white after etching because the steel has been metallographically transformed by the heat generated in the band formation process.



MP-5084-8

FIGURE 9 DETAILED PHOTOMICROGRAPH OF CRACK 9A ON CUT 7, WITH INSET SHOWING HIGH MAGNIFICATION OF SHEAR BAND REGION



MP-5084-7

FIGURE 10 DETAILED PHOTOMICROGRAPH OF CRACK 3A ON CUT 4, SHOWING VARIOUS RELATIONSHIPS BETWEEN SHEAR BANDING AND SUBSEQUENT CRACKING

primarily brittle fracture the remainder of the way toward the outer surface.\* We therefore chose to study in detail a fragment from Shot 4 and selected the one denoted by an arrow in Figure 6, as it appeared to contain a large number of shear bands that intersected the inner surface.

Photographs of the fragment from two different directions are seen in Figure 11. The two directions A and B highlight the shear bands that intersect the inner surface at the two different  $45^\circ$  planes. For identification purposes, the shear bands are labelled by a number and a letter (e.g., band 1B is the band numbered 1 that is visible from direction B). To allow examination of internal damage, the fragment was cut into thin layers perpendicular to the axial direction along the lines shown in Figure 11. The cut surfaces were then polished, etched, and examined metallographically. Figure 12 is a composite photomicrograph of the surface of cut 4, showing clearly how the shear bands visible on the inner surface extend into the material, and also revealing internal shear bands.

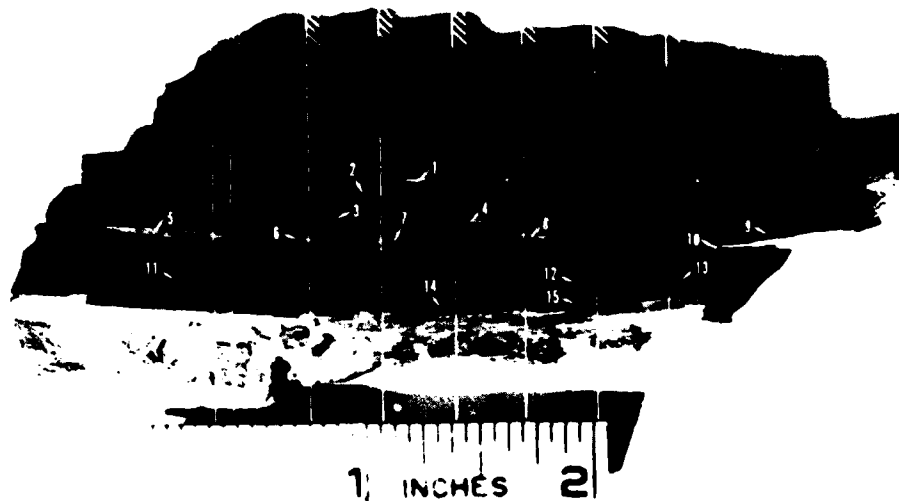
Examination of the composite photomicrographs taken from each of the eight cuts revealed that more than two-thirds of the shear bands intersected the inner surface of the cylinder. Two bands extended from the interior to the outer surface, and the remainder lay entirely within the interior. We believe that the bands originated at their innermost edge where the shear strains were larger and occurred earlier, and proceeded to grow outward; however, we cannot be certain of that in each case. Although most of the bands in this fragment stopped without interacting with any other bands, some bands did intersect others. Some short bands intersected and stopped at the middle of a longer band, indicating that the short band was formed at a later time than the longer band.

---

\* This was probably caused by the premature failure of the containment system, which allowed radial relief waves to propagate into the HF-1 tube, causing tensile failures.



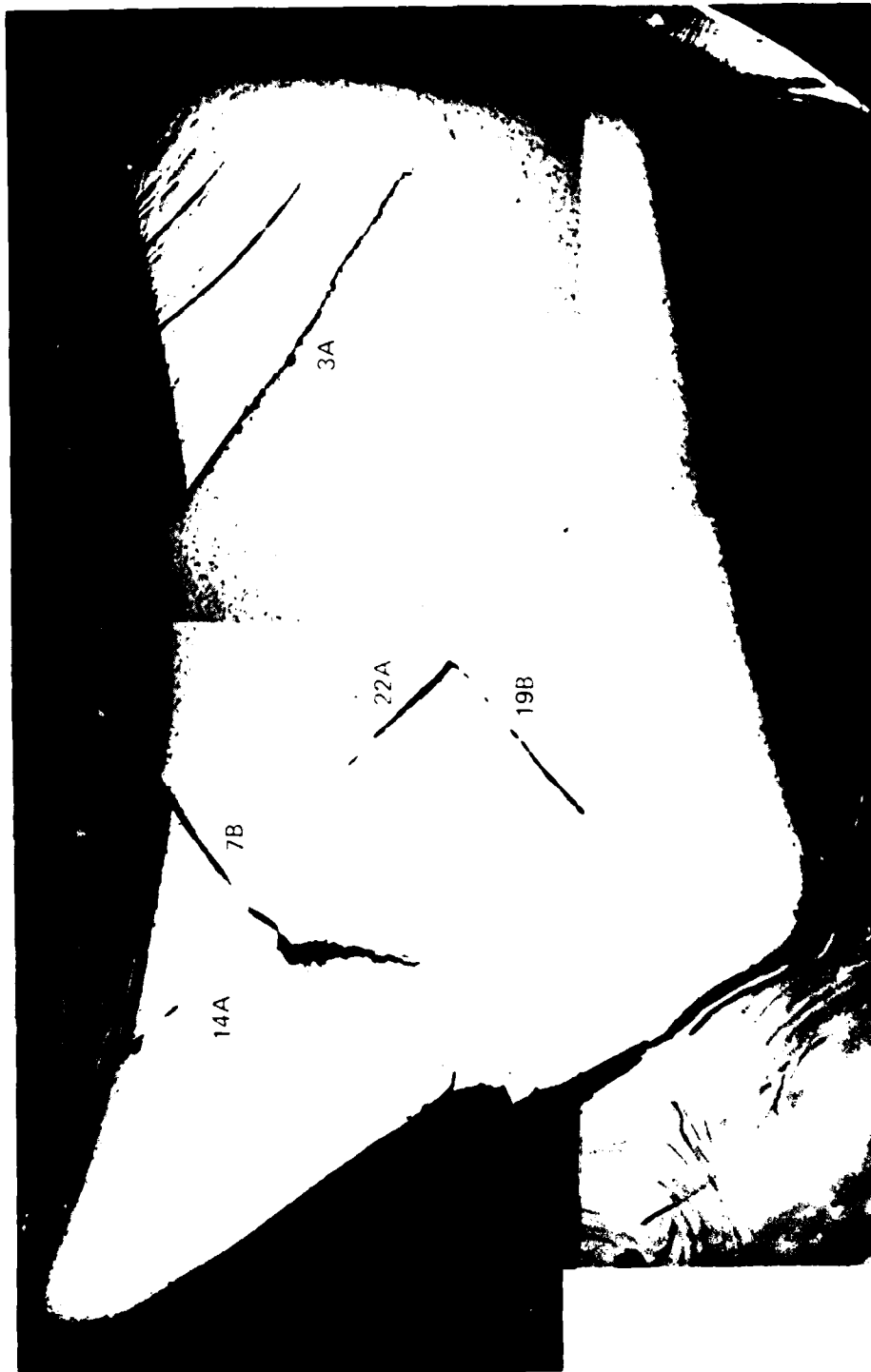
(a)



(b)

MP-5084-5

FIGURE 11 HF-1 STEEL FRAGMENT FROM SHOT 5084-4 SELECTED FOR USE IN QUANTITATIVE SHEAR BAND STUDY, PHOTOGRAPHED FROM (a) DIRECTION A AND (b) DIRECTION B



MP-5084-6

FIGURE 12 COMPOSITE PHOTOMICROGRAPHS OF CUT 4, SHOWING VARIOUS POSITIONS AND ORIENTATIONS OF SHEAR BANDS AND CRACKS WITHIN HF-1 FRAGMENT

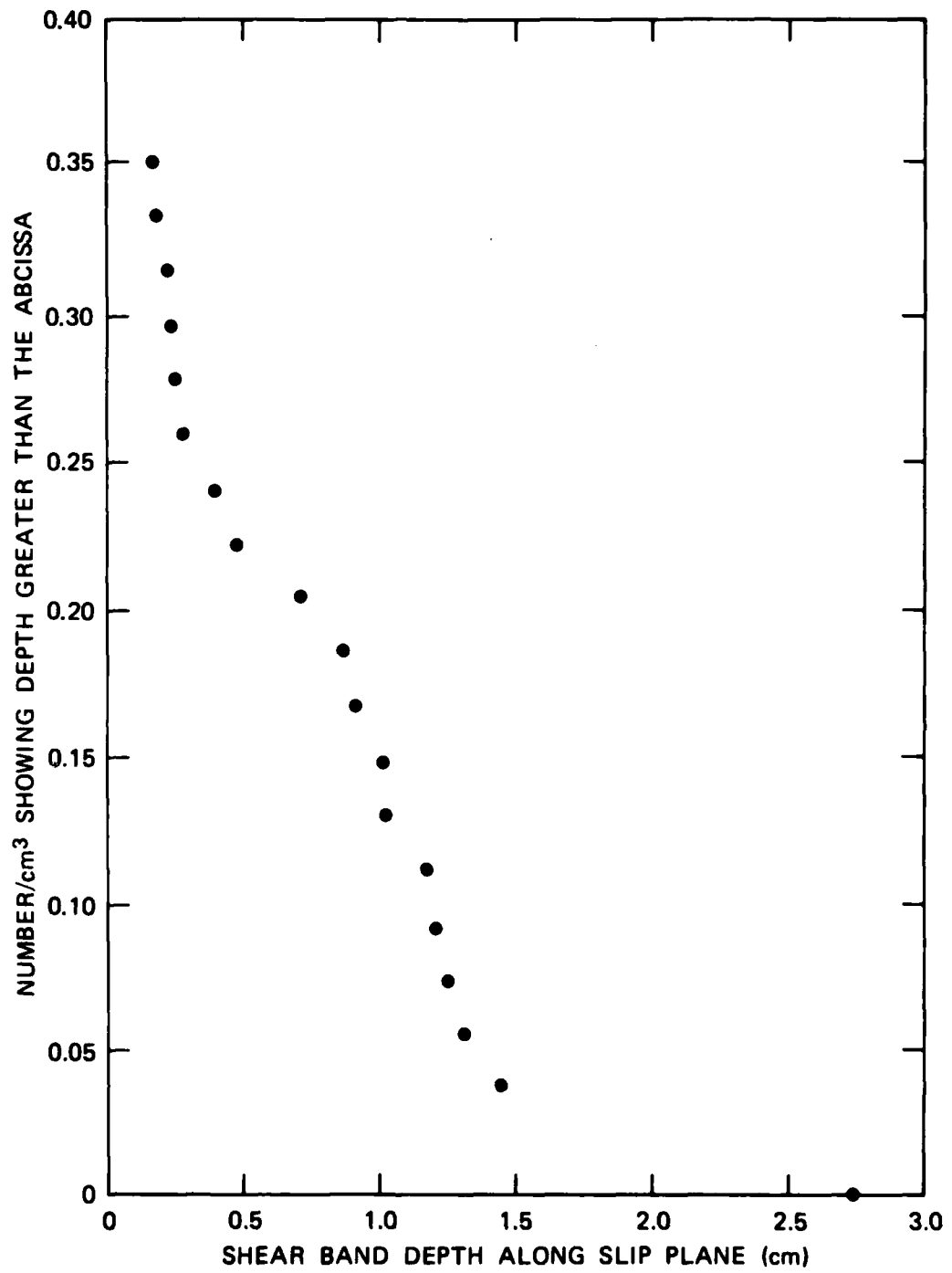
Note shear bands 14A and 7B intersect to form tensile crack.

Other intersecting bands, such as bands 14A and 7B in Figure 12 appeared to grow simultaneously and interact to form a tensile crack beginning at their point of intersection.

The depth ( $d$ ) of all of the bands revealed on the eight composite photomicrographs was measured, yielding the distribution shown in Figure 13. Since the cuts did not necessarily intersect the bands at their point of maximum depth, the depth values measured are only lower bounds. If we examined a greater number of bands, a statistical transformation similar to that used for tensile failure analysis<sup>4</sup> could be used to determine the actual distribution.

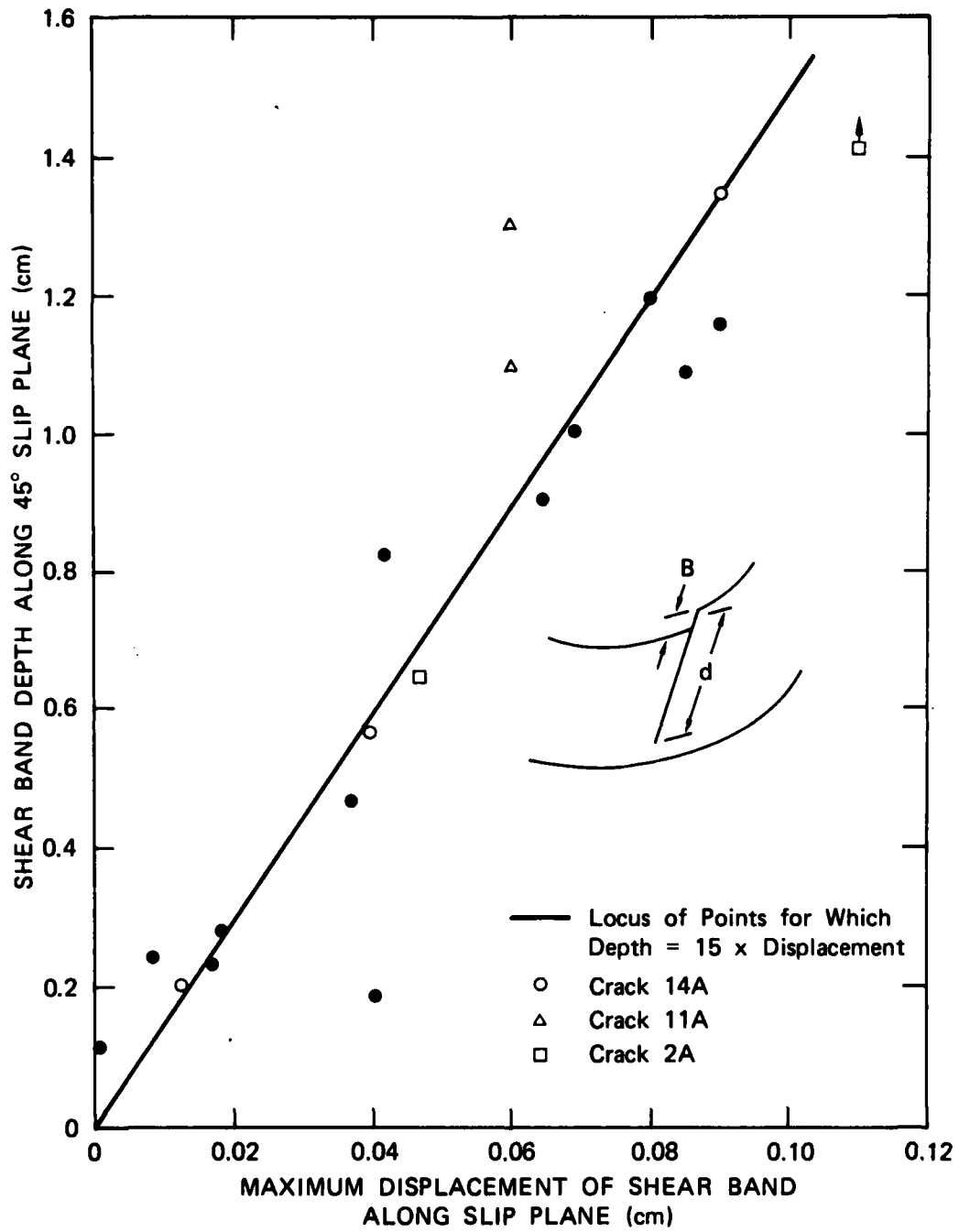
The surface shear displacement ( $B$ ) for all the bands intersecting the surface was measured and the relationship between  $d$  and  $B$  for all of those bands is plotted in Figure 14. Three bands that extended over several cuts are identified by special symbols. Most of the points lie close to the line  $d = 15B$ , indicating a direct proportion between the shear band depth and surface displacement.

The shear band depths were compared with the length at the inner surface so as to determine the approximate shape of the shear band in its slip plane. The results are plotted in Figure 15, along with the locus of points for a semicircular shear band shape. Again, noting that the depth values are only lower bounds, it appears that  $l$  is on the order of twice  $d$ . If a shear band is assumed to start growing at a single point, then it appears to grow in depth about as much as it grows in surface length on each side of its starting point. Without an extensive program of successive cycles of grinding, polishing, etching, and photography, we cannot observe the precise shape of the outer edges of the shear bands. However, since  $d \approx 15B$ , we can get an approximate idea by observing the shape of the slip plane exposed above the inner surface in Figure 11 (or in other words, how  $B$  varies along the length).



MA-5084-12

FIGURE 13 DEPTH DISTRIBUTIONS OF SHEAR BANDS IN HF-1 STEEL FRAGMENT



MA-5084-10

FIGURE 14 SHEAR BAND DEPTH (d) VERSUS DISPLACEMENT (B) DATA

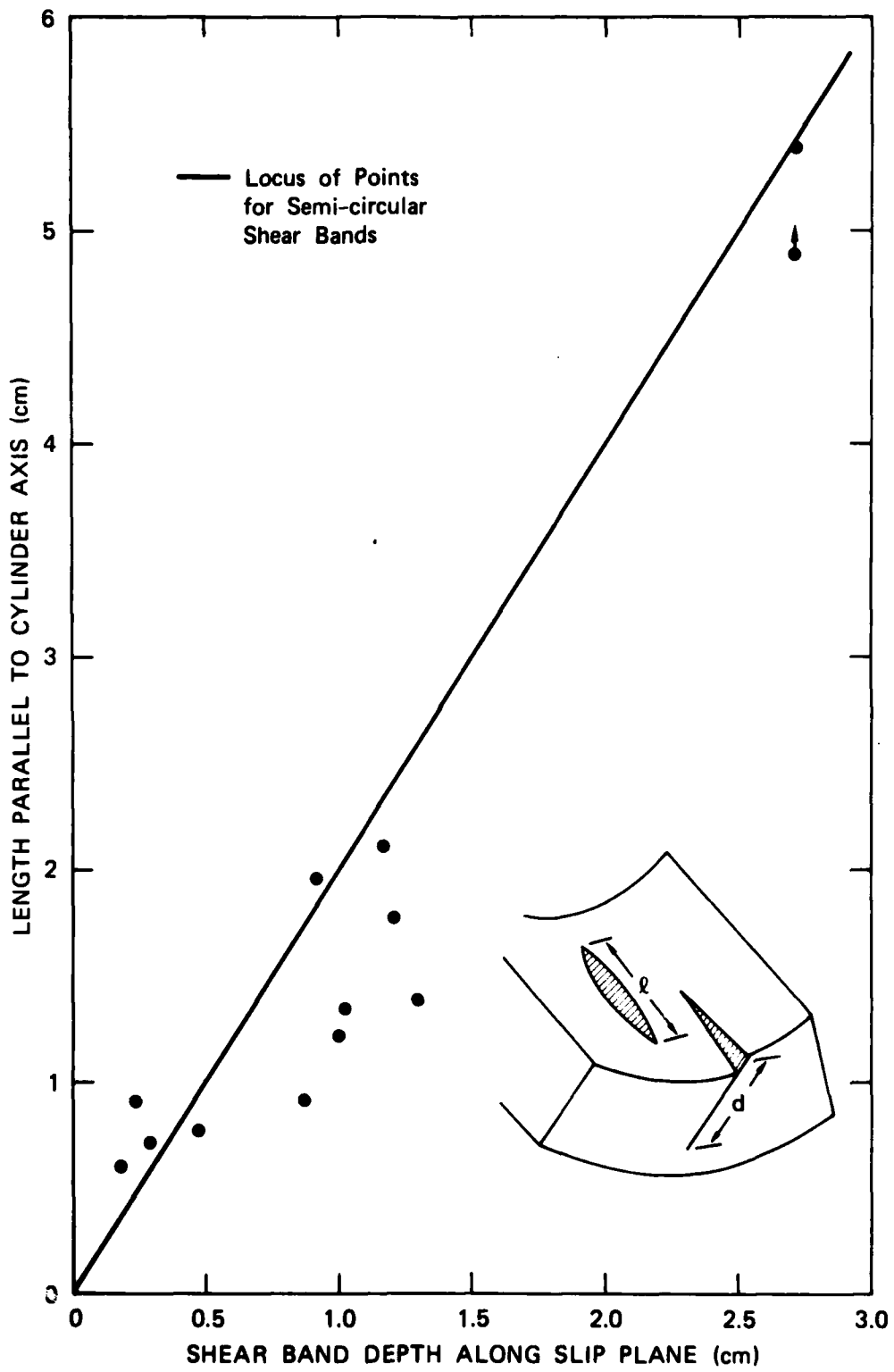


FIGURE 15 SHEAR BAND LENGTH ( $\rho$ ) VERSUS DEPTH ( $d$ ) DATA

Using this method, we find that some shear bands appear semicircular, others seem elliptical, and others have more complex shapes. But for computational modeling, it appears that the bands can be represented as semicircles.

#### D. Conclusions

The above work has lead to the following experimental observations:

- Multiple waves of tension and compression propagate through the thickness of a fragmenting cylinder.
- Shear bands nucleate and grow in proportion to the amount of shear strain.
- Bands usually appear to start at the inner diameter of fragmenting rounds, but often they appear at some depth within the material.
- For bands with large displacement, the radial and axial extent of the bands are comparable; hence, bands are approximately circular.
- The maximum dislocation of material across a band occurs at the center and is 5 to 10% of the radial or axial extent of the band.
- Bands form at  $45^{\circ}$  to the principal directions; that is, in the directions of maximum shear stress.
- During plastic flow, many small ripples or striations appear on the inner surface at a strain of about 15%. At larger strains, a small number of these striations form shear bands.
- Brittle cracks often form along the bands at a late stage.

In conclusion, the contained fragmenting round technique has proven successful in increasing our knowledge of shear banding phenomena. However more experiments are required to better establish the nucleation criteria and the band growth velocities.

#### IV SHEAR BAND MODEL DEVELOPMENT - COMPUTATIONAL PHASE

The computational model for shear banding is a detailed description of the processes by which shear bands form and grow in a material undergoing large deformation. This section contains a review of the phenomena, an analysis relating the nucleation and growth to material properties, and a discussion of additional features needed to implement the model in a subroutine. A listing of the subroutine and further information about the parameters are given in Appendix B.

The subroutine containing shear banding acts as a stress-strain relation in a one- or two-dimensional wave propagation computer program. The program computes strain increments in a cell of material and then calls the shear band subroutine to calculate the corresponding stresses. If a threshold criterion has been exceeded, the subroutine also calculates the growth of existing bands and the nucleation of new bands, and checks whether coalescence and fragmentation are occurring. For each cell of material, there are data arrays containing the size, number, and orientation of all bands.

The shear band model is intended to account for the experimental observations listed at the end of the previous section. In addition to those features, the model includes rate-dependent elastic-plastic stress-strain relations.

##### A. Derivation of the Model

The model includes nucleation of shear bands, growth of the bands, coalescence to form fragments, and relaxation of the stresses in accordance with the growth of damage. In the following discussion, the physical processes of failure by shear banding are outlined. Then each process is examined and equations are derived to represent the process in the model.

Under a high shear strain, materials first deform uniformly, following approximately the usual assumptions of homogeneity and isotropy. But as the plastic strains become large, inhomogeneities may develop. At these inhomogeneities, a slip like a small crack can occur parallel to the direction of maximum shear stress and strain. With continued straining, the slipped region or shear band grows in a circular fashion. That is, the growth rate in the direction of the shear slip is approximately equal to that in the direction perpendicular to the slip. Following nucleation of the bands, growth can occur until the bands coalesce. On a cross section the band is observed as a narrow strip of highly deformed material. Probably the strip is heated approximately to melting during growth of the band. At the end of growth, the band material remains welded together, but with a reduced tensile strength. Hence, subsequent tensile stresses in the material will fracture in or along the band.

#### 1. Nucleation

The nucleation process includes several features: a threshold for nucleation, the rate of nucleation, the size of bands at nucleation, and the orientation of the bands. When the plastic shear strain exceeds a threshold value, nucleation begins. In the HF-1 material there is a threshold at about 15% at which small irregularities appeared in the surface. But since significant slipping begins at 30%, this value of plastic strain serves as the threshold criterion. Thus, the threshold is an observed quantity and probably varies from one material to the next.

The derivation conducted by Seaman et al.<sup>2</sup> indicated that the rate should be proportional to the square of the yield strength and to the applied strain rate; the resulting calculations correlated fairly well with the measured fragment size distributions. In that study the orientation of the shear bands was not considered, so nucleation referred

to the sum of the bands in all directions and the shear strain was a scalar (undirected) quantity.

Here a nucleation rate function is proposed to account for the observed relationships to plastic shear strain and yield strength and to provide an orientation dependence for the shear band process. The major assumption in the following proposed expression is that the nucleation rate in a direction is proportional to the plastic shear strain in the same direction.

$$\frac{dN_{\varphi\theta}}{dt} = C_n F_n \left( \frac{1}{E_{cr}} \frac{dE^P}{dt} \right)^2 \frac{d\epsilon_{\varphi\theta}^{ps}}{dt} \quad (1)$$

Here  $E_{cr}$  is a critical energy, taken to be the melt energy;  $dE^P/dt$  is the rate of increase of plastic strain energy;  $N_{\varphi\theta}$  is the number of shear bands per unit volume in the  $\varphi\theta$  direction; \* and  $\epsilon_{\varphi\theta}^{ps}$  is the plastic shear strain in the same direction.  $C_n$  is a coefficient with the units of time squared, and  $F_n$  is a factor representing the fraction of solid angle assigned to the  $\varphi\theta$  orientation. Orientation effects are treated in more detail later. The factor  $dE^P/dt$  is proportional to the product of the shear strain rate and the yield strength; hence, the nucleation rate is proportional to the cube of the strain rate.

The plastic strain energy is calculated as follows.

$$dE^P = V \sum \sigma'_{ij} d\epsilon_{ij}^P \quad (2)$$

where  $V$  is specific volume,

---

\* Here  $\varphi$  is the polar angle and  $\theta$  is the angle of rotation about the pole.

$\sigma'_{ij}$  is the deviator stress in the  $ij$  direction, and  
 $d\epsilon_{ij}^p$  is the plastic strain increment in the  $ij$  direction.

The plastic strains in any orientation are given by the flow rule

$$d\epsilon_{ij}^p = \frac{\sigma'_{ij}}{\bar{\sigma}} d\bar{\epsilon}^p \quad (3)$$

$$\text{where } \bar{\sigma} = \sqrt{1.5} \sqrt{[(\sigma'_{11})^2 + (\sigma'_{22})^2 + (\sigma'_{33})^2 + 2(\sigma'_{12})^2]} \quad (4)$$

$$d\bar{\epsilon}^p = \sqrt{1.5} \sqrt{[(d\epsilon_{11}^p)^2 + (d\epsilon_{22}^p)^2 + (d\epsilon_{33}^p)^2 + 2(d\epsilon_{12}^p)^2]}. \quad (5)$$

With the  $\sqrt{1.5}$  factor in the definition of  $d\bar{\epsilon}^p$ ,  $d\bar{\epsilon}^p$  is the shear strain in any geometry where two strain components are equal. The plastic shear strains in the six orientations,  $d\epsilon_{ij}^{ps}$ , are obtained by using for  $\sigma'_{ij}$  in Eq. 3 only the shearing component of the deviator stress acting on each of the six planes. These shear stress components are listed in Table 2.

Table 2

## SHEAR STRESS COMPONENTS ACTING ON SHEAR BAND PLANES

Direction <sup>a</sup>		S.B. Type <sup>b</sup>	Shear Stress Component
Index	Direction <sup>c</sup>		
1	axial	-	$\sigma'_{12}$
2	radial	-	$\sigma'_{12}$
3	circumferential	-	none
4	45° between axial and radial	2	$\frac{1}{2}(\sigma'_{11} - \sigma'_{22})$
5	45° between axial and circumferential	3	$\frac{1}{2}\sqrt{(\sigma'_{11} - \sigma'_{33})^2 + 2\sigma'^2_{12}}$
6	45° between radial and circumferential	1	$\frac{1}{2}\sqrt{(\sigma'_{22} - \sigma'_{33})^2 + 2\sigma'^2_{12}}$

## Notes

- a The direction index indicates one of 6 stress directions.  
 b Shear band orientation type as shown in Figure 8.  
 c Orientations used in a two-dimensional, axisymmetric code (TROT).

Shear bands may appear in many orientations and with many sizes. However, for one- and two-dimensional problems, we have chosen six specific orientations to represent the continuum of all orientations. The orientations provided are for bands normal to three perpendicular coordinate directions and for three more at  $45^\circ$  to the first three. The latter three lie in the x-y plane, x-z plane, and y-z plane, respectively. For each of these orientations a fraction of all possible orientations is assigned. Each of the first three orientations represents two points on the unit sphere (for example,  $x = \pm 1$ ) whereas each of the  $45^\circ$  orientations represents four points. Therefore, it seemed reasonable to weigh the six points with factors,  $F_n = 1/9, 1/9, 1/9, 2/9, 2/9, \text{ and } 2/9$ , respectively.

For each orientation there is a set of size groups consisting of a number of bands per cubic centimeter  $N_i$  with a radius  $R_i$ . Initially these size groups represent the continuous distribution

$$N_g = N_o \exp(-R/R_n) \quad (6)$$

where  $N_g$  is the number of bands/cm<sup>3</sup> greater than R

$N_o$  is the total number

$R_n$  is a nucleation size parameter.

This continuous distribution is divided into size groups such that the  $i^{\text{th}}$  group contains  $\Delta N_i$  bands given by the following formula:

$$\Delta N_i = \dot{N} \Delta t [\exp(-R_i/R_n) - \exp(-R_{i+1}/R_n)] \quad (7)$$

By using size groups that are discrete in size and orientation it is possible to represent growth and nucleation processes that are strongly dependent on shear band size and plastic strain tensors that vary greatly with orientation.

## 2. Growth

The growth of a shear band refers to the increase in radius of the slipped area. Following Seaman, et al.,<sup>2</sup> we have assumed that the velocity of the shear band is proportional both to its radius and to the plastic shear strain rate; that is,

$$\frac{dR_i}{dt} = C_G \left[ \frac{d\epsilon_{\varphi\theta}^{ps}}{dt} R_i \right] \quad (8)$$

where  $C_G$  is a growth coefficient,  $d\epsilon_{\varphi\theta}^{ps}/dt$  is the plastic shear strain rate on the  $\varphi\theta$  plane, and  $R_i$  is the radius of the  $i^{\text{th}}$  band in a size distribution. The growth in Eq. (8) is limited by two additional requirements: The velocity cannot exceed the shear wave velocity, and the total distortion of all the bands in the  $\varphi\theta$  orientation cannot exceed the total plastic shear strain on the orientation. The first of these requirements is simply stated as

$$R_2 \leq R_1 + V_{\max} \Delta t$$

where  $V_{\max}$  is the shear wave velocity. The second requirement is based on a restatement of the Orowan equation used in dislocation dynamics. The appropriate expression here is

$$\frac{d\epsilon^P}{dt} = \frac{d}{dt} \left( \pi \sum_i N_i R_i^2 B_i \right) \quad (9)$$

where  $B_i$  is the average shear slip over the area  $\pi R_i^2$  of the band. If  $N_i$  (the number of shear bands) is replaced by the band edge length  $n_i = 2\pi R_i N_i$ , and  $N_i$  is presumed constant during differentiation, the usual Orowan equation is obtained. Over a finite time interval and for

a fixed number of bands, Eq. 9 takes the form

$$\Delta\epsilon^P = \pi \sum N_i (B_{2i} R_{2i}^2 - B_{1i} R_{1i}^2) \quad (10)$$

where subscripts 1 and 2 indicate quantities before and after the time step. If  $\Delta\epsilon^P$  from Eq. 10 exceeds the total imposed increment in plastic strain, then  $R_2$  is reduced to meet the requirement.

From the experimental data of our fragmentation tests 4 and 5, the dislocation in a circular shear band appears to be 5 to 10% of the radius. That is,

$$B = bR \quad (11)$$

Thus, the dislocation increases in proportion to the radius. Eq. 10 then takes the form

$$\Delta\epsilon^P = \pi b \sum N_i (R_{2i}^3 - R_{1i}^3) \quad (12)$$

### 3. Effects of Damage

Damage caused by shear bands leads to a relaxation of the stresses as well as to eventual separation of the material into fragments. The relaxation effect is produced when damage reduces the area across which stress can be transmitted. The average stress  $\sigma$  over the total or gross section is then related to the stress  $\sigma^S$  in the intact or solid material through a damage quantity  $D$ . In tension the relation is

$$\sigma = \sigma^S(1-D) \quad (13)$$

The gross section  $A_g$  is composed of a solid area and a damaged area  $A_g(1-D)$ . The next step is to derive an appropriate expression for  $D$  that will approach 1.0 for full fragmentation and account for the anisotropy of damage.

To determine an appropriate damage function, we examine two quantities: the total plastic strain taken by the bands and the fraction of the material that has fragmented. The total plastic strain in any orientation is, according to Eq. 12,

$$\epsilon^p = \pi b \sum_i N_i R_i^3 \quad (14)$$

When the material breaks into fragments, the volume of fragments is

$$V = T_F \sum_i N_i^f (R_i^f)^3 = 1.0 \quad (15)$$

where  $T_F$  is a dimensionless volume factor (about 4.0)

$N_i^f$  and  $R_i^f$  are number and radius of fragments in the  $i^{\text{th}}$  size group.

The numbers of fragments are related to the numbers of bands through the factor  $\beta$ :

$$N_i^f = \beta N_i \quad (16)$$

Chunky fragments usually have six or eight sides that were each formed by a band or crack. Because each crack forms a side of two fragments, three or four cracks must be associated with each fragment. Therefore,  $\beta$  equals 1/3 or 1/4. Similarly, the fragment sizes are related to the band sizes through the factor  $\gamma$ :

$$R_i^f = \gamma R_i \quad (17)$$

Here  $R_i^f$  is defined so that the fragment volume is  $T_F (R_i^f)^3$  where  $T_F$  is about  $4\pi/3$ . The cracks forming the fragment sides have about the same area as the sides, so  $\gamma$  is approximately equal to 1. Now Eq. 15

can be rewritten as a double sum of shear bands over orientations and size groups:

$$V = T_F \beta \gamma^3 \sum_{\theta} \left[ \sum_i N_{\theta i} R_{\theta i}^3 \right] = 1 . \quad (18)$$

A comparison of Eqs. 14 and 18 shows that damage appears to be related to  $NR^3$  at all times during the calculation. We will use Eq. 18 as our definition of complete fragmentation ( $V = 1$ ) and let  $V$  be the fragmented fraction for values less than full fragmentation. Then the quantity  $T_F \beta \gamma^3 \sum_i N_{\theta i} R_{\theta i}^3$  is a measure of the damage associated with the bands in the  $\theta$  orientation. We can assume that the damage felt in any direction is proportional to  $\cos^2 \psi$  where  $\psi$  is the angle between the stress direction and the damage orientation. Then the damage in the  $x$  direction is

$$D_{xx} = 3T_F \beta \gamma^3 [\tau_{xx} + 0.5(\tau_{xy} + \tau_{xz})] \quad (19)$$

where

$$\tau = \sum_i N_i R_i^3 \quad (20)$$

and the subscripts on  $\tau$  identify one of the six orientations considered. The factor 3 in front of the expression for  $D_{xx}$  permits  $D_{xx}$  to reach 1.0 when  $V$  reaches 1.0 with all  $\tau$ 's equal. The 0.5 in the expression for  $D_{xx}$  is  $\cos^2 45^\circ$ . The damage quantity in the  $y$  and  $z$  directions are computed by Eq. 19 with a natural permutation of the subscripts. For the  $xy$  direction the damage is

$$D_{xy} = 3T_F \beta \gamma^3 [\tau_{xy} + 0.5(\tau_{xx} + \tau_{yy})] . \quad (21)$$

With the foregoing definitions of damage  $D$ , we can examine in more detail the relaxation process in Eq. 13. That equation must be modified for compression where we can expect the deviators to reduce with damage but the pressure should not be affected. Toward this end, the gross pressure  $P$  is related to the solid stresses  $\sigma_{ii}^s$  for the tensile case. Then the gross stress  $\sigma_{ii}$  is

$$\sigma_{ii} = \sigma_{ii}^s (1 - D_{ii}) \quad (22)$$

$$P = \frac{\sum \sigma_{ii}^s (1 - D_{ii})}{3} = \frac{\sum \sigma_{ii}'^s (1 - D_{ii}) + P_s [3 - (D_{11} + D_{22} + D_{33})]}{3}$$

$$= \frac{1}{3} \sum \sigma_{ii}'^s (1 - D_{ii}) + P_s (1 - D) \quad (23)$$

where  $\sum D_{ii} = 3D$ ,  $P_s$  is the solid pressure,  $\sigma_{ii}$  is stress on the gross section and  $\sigma_{ii}'^s$  is deviator stress on the intact or solid material. For the compression case a suitable modification of Eq. 23 is obtained by deleting the factor  $(1 - D)$  and defining a modified pressure  $P'$ :

$$P' = \frac{1}{3} \sum \sigma_{ii}'^s (1 - D_{ii}) + P_s = \frac{1}{3} \sum \sigma_{ii}^s (1 - D_{ii}) + P_s D$$

$$= P + P_s D$$

Then for tension let  $P' = P$  and use Eq. 24 to define  $P'$  in compression. With these definitions of  $P'$ , the solid stresses are related to the gross stresses as follows in both tension and compression:

$$\sigma_{ii}^s = \frac{\sigma_{ii}' + P'}{1 - D_{ii}} \quad (25)$$

At the beginning of a strain increment calculation,  $\tau$  and  $P_s$  are computed from the existing shear bands and density, and  $P'$  is calculated from the old gross stresses,  $\sigma_{ii}$  and from  $P_s$  for compression. Then the  $\sigma_{ii}^s$  are calculated from Eq. 25. At the end of the increment, Eqs. 24 and 25 are again used to obtain the gross stresses.

The criterion for full fragmentation is given in Eq. 18. This criterion is reached simultaneously with the condition that all gross deviator stresses have relaxed to zero.

#### 4. Stress-Strain Relations

In preparation for the stress calculations, the gross stresses from the calling program are transformed to stresses in the intact material using Eq. 13. These stresses are then separated into pressure and deviator components. The pressure is given by the Mie-Gruneisen equation:

$$P = P_H \left(1 - \frac{\Gamma \mu}{2}\right) + \Gamma \rho E \quad (26)$$

where  $\mu = \rho/\rho_0 - 1$

$\Gamma$  is Gruneisen ratio

$\rho$  is the current density

$\rho_0$  is the zero pressure density

$E$  is the internal energy

and  $P_H = K_1 \mu + K_2 \mu^2 + K_3 \mu^3$  is the pressure on the Hugoniot.  $K_1$  is the bulk modulus, and  $K_2$  and  $K_3$  are coefficients in the Hugoniot expansion.

The deviator stresses are computed from elastic, plastic, work-hardening, rate-dependent relations. For the elastic case the deviator stresses are computed as

$$\sigma'_{ij} = 2G\Delta\epsilon'_{ij} + \sigma'_{ij0} \quad (27)$$

where  $G$  is the shear modulus,

$\Delta\epsilon'_{ij}$  is the deviator strain increment and

$\sigma'_{ij0}$  is the deviator stress on the previous cycle.

For yield calculations, the effective stress from von Mises plasticity theory is used

$$\bar{\sigma} = \sqrt{\frac{3}{2} \sum_{i,j} \sigma'_{ij} \sigma'_{ij}} \quad (28)$$

Yield occurs for  $\bar{\sigma} \geq Y$ , the yield strength.

A linear work-hardening is assumed such that

$$Y = Y_0 + Y_D \bar{\epsilon}^{-p} \quad (29)$$

where  $Y_D$  is the work-hardening modulus

and  $\bar{\epsilon}^{-p} = \int \sqrt{\frac{3}{2} \sum_{i,j} d\epsilon_{ij}^p d\epsilon_{ij}^p}$ , the equivalent plastic strain, defined in terms of the plastic strain deviator increments  $d\epsilon_{ij}^p$ .

Strain-rate effects are treated with the linear viscous, one-parameter model

$$\frac{d\sigma'_{ij}}{dt} = 2G \frac{d\epsilon'_{ij}}{dt} - \frac{\sigma'_{ij} - Y \frac{d\epsilon_{ij}^p}{d\bar{\epsilon}^{-p}}}{T} \quad (30)$$

where  $T$  is a time constant. This equation is presumed to govern only when the stresses exceed yield. When work-hardening is combined with

the rate effects, the solution must be obtained numerically for general cases. The solution for stress derived by Seaman et al.<sup>2</sup> is

$$\sigma'_{ij} = \sigma'_{ijo} \exp[-(t - t_0)/T] \quad (31)$$

$$+ \left[ \frac{Y_1 + \frac{Y_D \bar{\sigma}^{-N}}{4G}}{1 + \frac{Y_D}{4G}} \cdot \frac{\sigma'_{ij}}{\bar{\sigma}^{-N}} + \frac{T}{t - t_0} (\sigma'_{ij}{}^N - \sigma'_{ijo}) \right] \left\{ 1 - \exp[-(t - t_0)/T] \right\}$$

where  $t - t_0$  is the duration of the time increment

$Y_1$  is the yield strength at the beginning of the increment

$\sigma'_{ij}{}^N$  and  $\bar{\sigma}^{-N}$  are elastically computed deviator stress and

effective stress from Eqs. 27 and 28. The plastic deviator strain increments govern the nucleation and growth processes. These strains are computed as the difference between the total deviator strains and the elastic values.

#### B. Simulations of Fragmenting Round Experiments

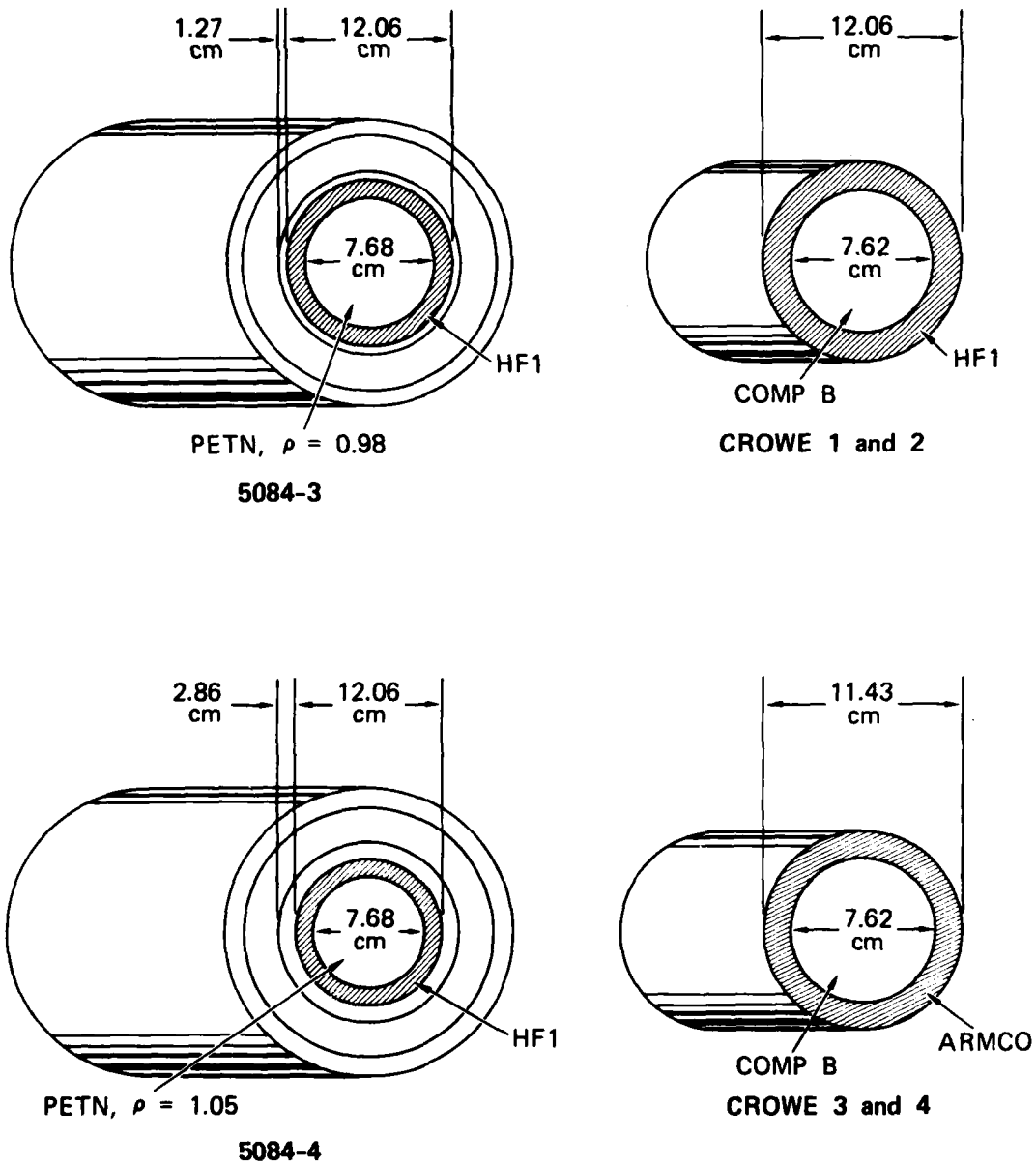
Computer simulations were made for three fragmenting cylinders of HF-1 high fragmentation steel, one cylinder of Armco iron, and one HF-1 fragmenting round of standard munition geometry. The shear band subroutine SHEAR2 was used as the stress-strain relation in all cases. Four of the cases were considered to be cylindrically symmetric, and therefore calculations were made with the one-dimensional wave propagation code PUFF. Since the fifth round (of HF-1) had the shape of a standard munition, a two-dimensional wave propagation code, TROTT, was used for that case. Adjustments were made in the two codes so that the identical SHEAR2 subroutine was used with each. The dimensionality of the codes

refers to the number of directions along which quantities can vary (radial in PUFF, radial and axial in TROTT). In both cases the stresses, strains, and damage have components in all three dimensions.

The geometries of the five experiments are shown in Figures 16 and 17. Three are configurations used by Crowe et al.;<sup>4</sup> the other two are part of this work. Experiment 5084-3 was simulated first with TROTT and SHEAR2 (with no damage permitted), and the pressure history at mid-length on the inner radius of the round was fitted to an exponential. This exponential pressure history was used for the SRI PUFF simulations of that experiment. For all other calculations, the explosive was simulated as a detonating material. In the cylindrically symmetric cases (SRI PUFF calculations), the explosion was treated as a simultaneous detonation. For the TROTT problem, (the fragmenting projectile) the explosive was simulated with a running detonation. All explosives were treated as polytropic gases except the PETN in 5084-4, which was handled with a tabular (pressure-volume) equation of state. The tabular values were obtained from a TIGER detonation calculation.<sup>5</sup> More details about these calculations, including the data decks for the calculations, are given in Appendix B.

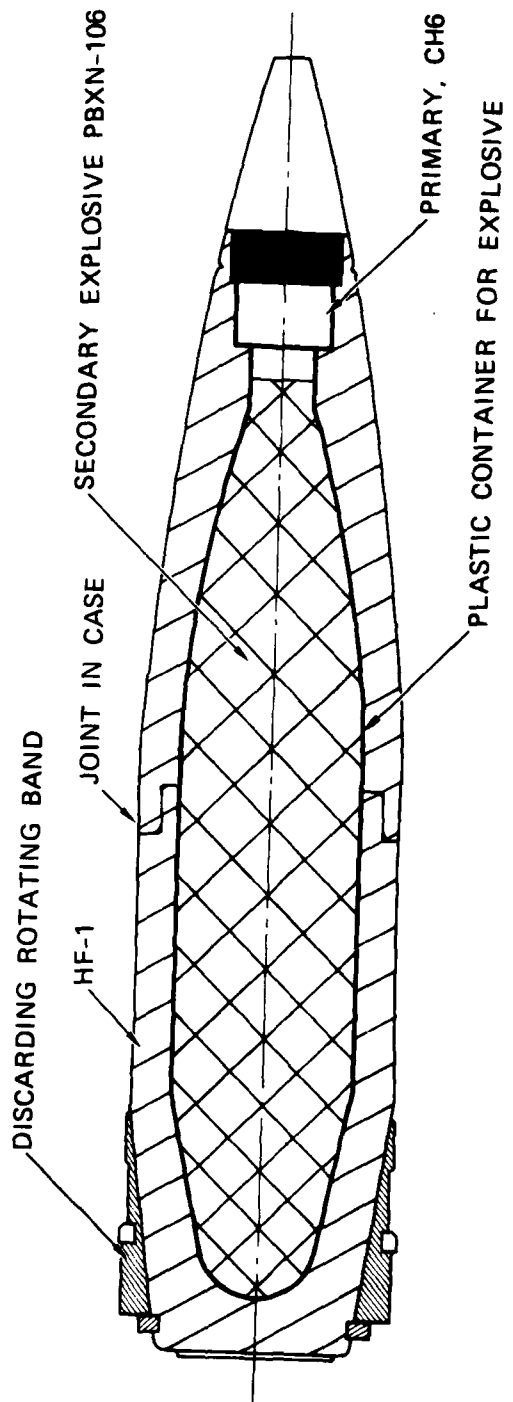
The results of the simulation of 5084-3 were simply that the maximum plastic shear strain was 1.15 times the threshold value. Because the experiment showed only slight evidence of the beginning of shear banding, there seems to be a satisfactory correlation of test and calculation.

The fragment size distributions for the three cylinders that showed complete separation are shown in Figure 18. The computed results are also shown. The two tests of Crowe occurred at a strain rate of about  $2 \times 10^4$ /sec through the period of high damage while experiment 5084-4 occurred at a strain rate of  $6 \times 10^3$ /sec. The experimental results with HF-1 show that an increase in strain rate leads to a much larger



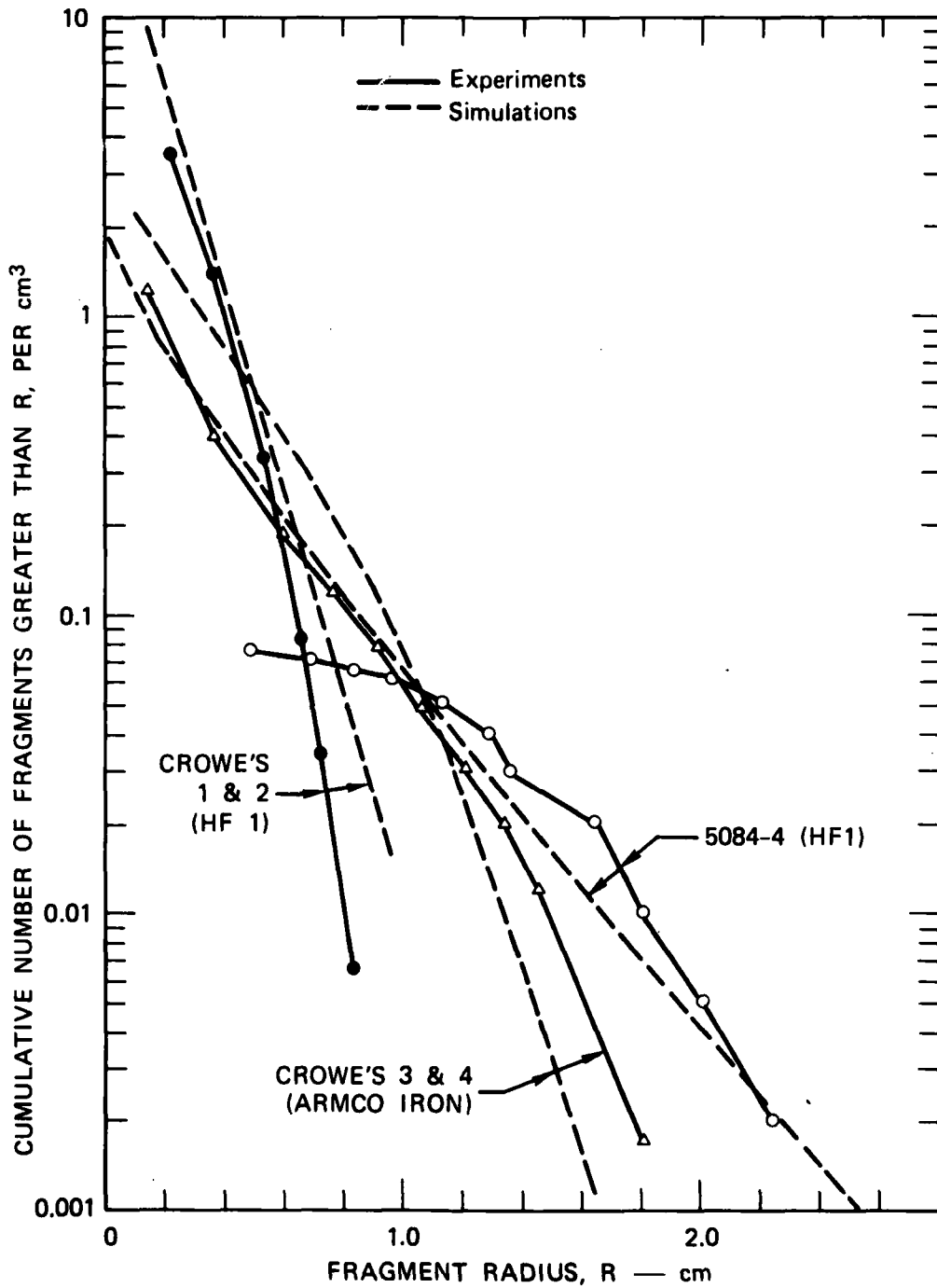
MA-5084-26

FIGURE 16 FOUR CYLINDRICAL FRAGMENTING ROUND CONFIGURATIONS TREATED WITH SRI PUFF AND THE SHEAR BAND MODEL



MA-5084-27

FIGURE 17 SCHEMATIC OF CROWE'S SAMPLE FRAGMENTING PROJECTILE



MA-5084-28

FIGURE 18 COMPARISON OF EXPERIMENTAL AND COMPUTED FRAGMENT SIZE DISTRIBUTIONS FOR HF-1 AND ARMCO IRON CYLINDERS

number of fragments, and consequently to smaller fragments. The Armco iron test, while conducted at the high strain rate, shows a fragment size distribution more like that from experiment 5084-4, which was conducted at the lower strain rate. This difference may be associated with the smaller number of inclusions in Armco iron, or with the lower yield strength; the data base is not yet adequate to provide such an association.

The marked difference in the distributions measured in the two HF-1 experiments provide a good test of the model. The same parameters were used in both HF-1 calculations. The correspondence between computed and observed distributions indicates that the model can account for the differences in strain rate, geometrical layout, and explosive pressure. The Armco iron calculation was run with a nucleation coefficient one-third that for HF-1 ( $C_n = 10^{-3}$  for HF-1,  $3 \times 10^{-4}$  for Armco). This difference in parameters probably arises because of the fewer nucleation sites in Armco iron. The nucleation plastic strain threshold probably should also have been changed for Armco iron, but no value was known.

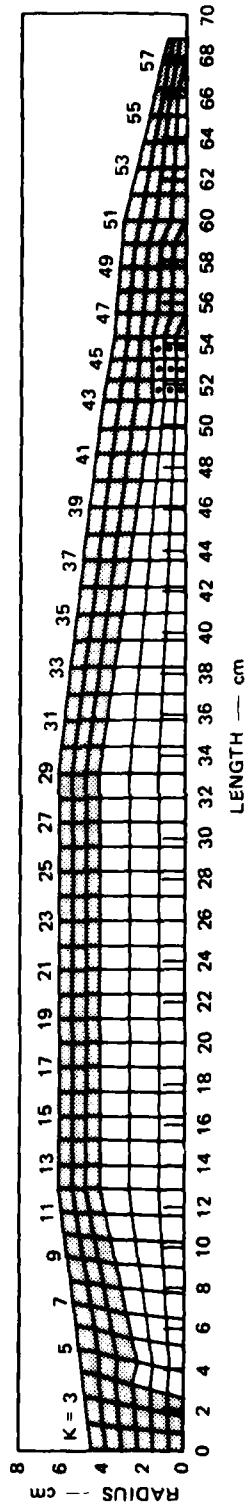
The PUFF simulations of the three cylinder experiments showed that the contained rounds required much longer to reach full fragmentation than the unconfined rounds. Crowe's experiments took about 45  $\mu$ sec to reach full fragmentation,<sup>4</sup> according to the calculations, while the contained cylinder required over 200  $\mu$ sec. In all three cases the shear banding began at the inner radius and gradually moved out. All computational cells showed shear banding in all three of the active orientations illustrated in Figure 8. However, in each case, orientation 1 was the first one activated; the others began to nucleate bands much later. When the bands from the three orientations were added, orientations 2 and 3 contributed only a few percent at most. This result agrees with the experiments, which indicate that most bands are in the first orientation.

The two-dimensional simulation of Crowe's sample fragmenting projectile was performed with the cell layout shown in Figure 19. All the metal parts are of HF-1 steel. No provision was made for the joint in the two parts of the case. The primary explosive in the fuse is CH6 and the secondary explosive is PBXN 106. The simulation includes treatment of a running detonation that starts in the primary and sweeps at the C-J velocity through the secondary explosive. The progress of the running detonation is evident from the cell motion in Figure 20, which shows a series of plots from the two-dimensional calculations. The indicators in the figure show the attendant progress of fracturing in the HF-1 cells.

Figure 21 shows a comparison of the computed fragment size distribution with the measured distribution. The computed distribution was obtained by summing the fragment size distributions from all computational cells, accounting for the relative mass associated with each cell. Cells that did not fragment were mainly in the nose, and all unfragmented masses were added in as a single large chunk. In this two dimensional simulation, the first shear band mode activated was usually orientation 1 at  $45^{\circ}$  between radial and circumferential directions. Usually this mode also dominated at the time of fragmentation. Considerable shear strain also occurred along planes of constant radius or axial distance, and if bands had been permitted on these orientations, some shear bands would have occurred in the calculations. The duration of detonation was about 65  $\mu$ sec. By 110  $\mu$ sec, nearly all the shear banding cells were completely fragmented. No shear banding occurred forward of K-row 48.

Having completed these simulations of the fragmenting rounds, we then examined ancillary aspects of the computed results to see how these aspects matched the data. Among these aspects were the amount of homogeneous plastic strain, the effect of microcracking, the relative importance of the nucleation process, and the information that can be obtained from the shape of the fragment size distribution.

- MF-1
- PBXN-106
- CH 6



MA-5084-29

FIGURE 19 CELL LAYOUT FOR TWO-DIMENSIONAL SIMULATION OF CROWE'S SAMPLE FRAGMENTING PROJECTILE

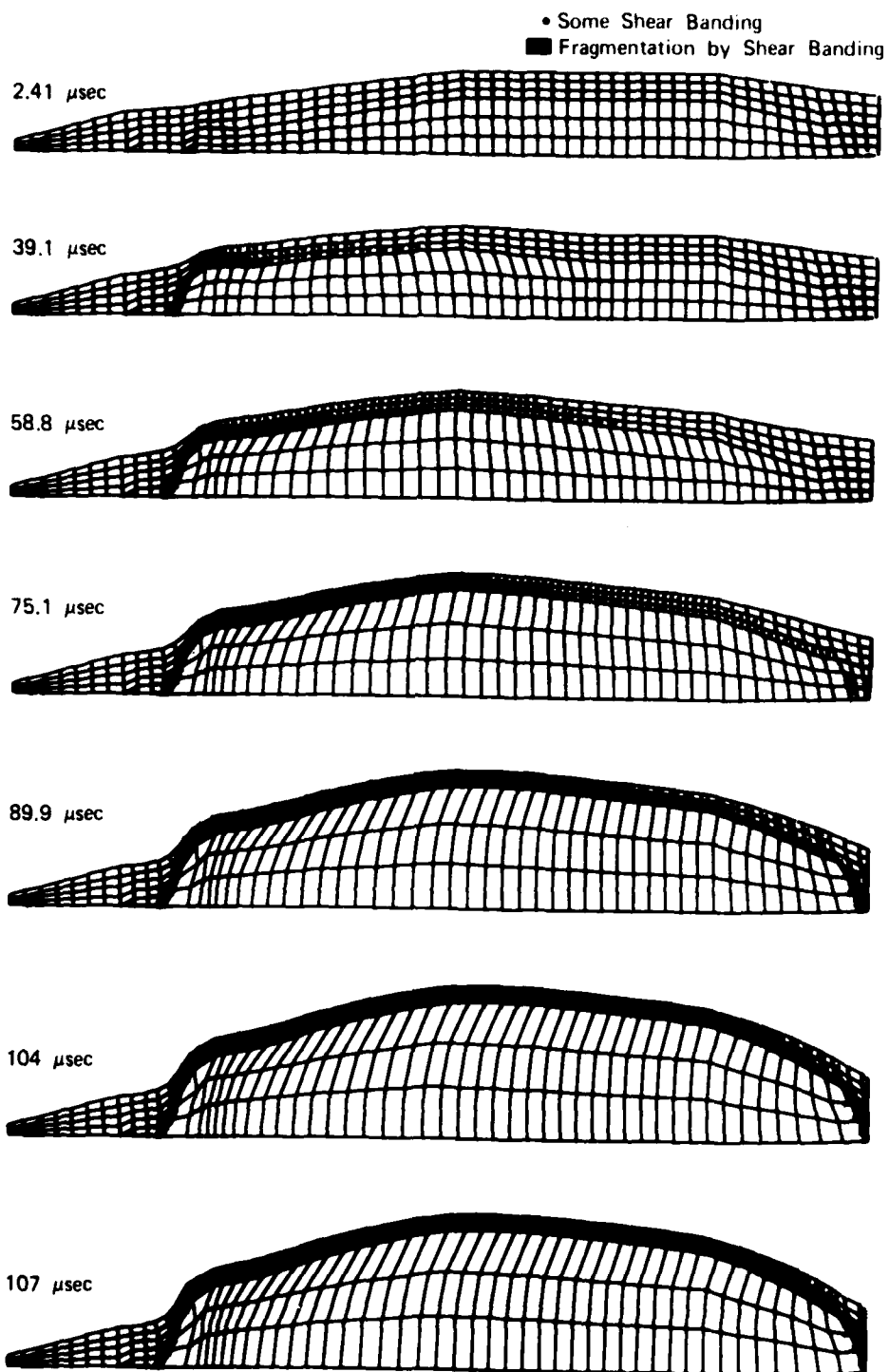


FIGURE 20 PROGRESS OF DETONATION AND SHEAR BAND DAMAGE COMPUTED IN THE TWO-DIMENSIONAL SIMULATION OF CROWE'S SAMPLE FRAGMENTING PROJECTILE

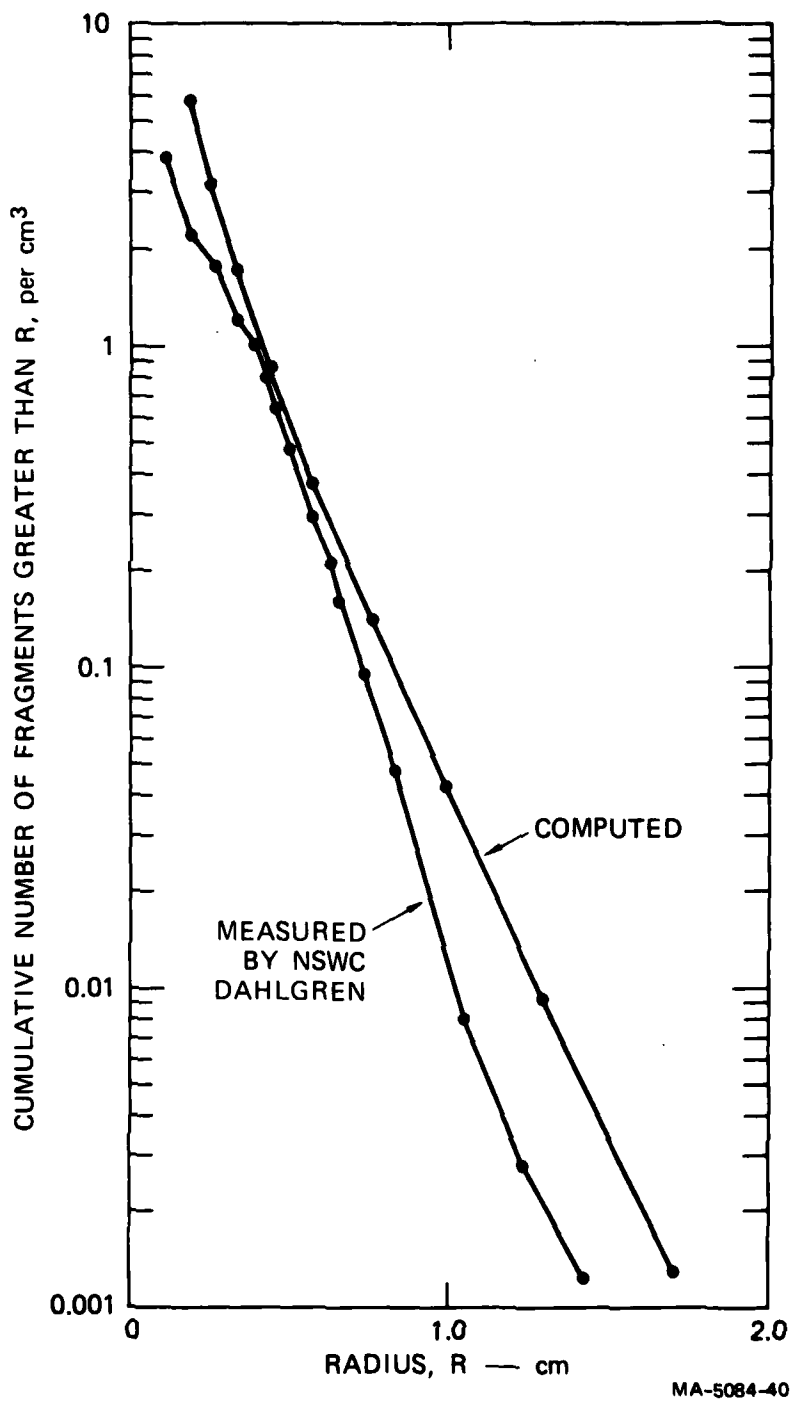


FIGURE 21 COMPARISON OF COMPUTED AND OBSERVED FRAGMENT SIZE DISTRIBUTIONS FOR CROWE'S SAMPLE FRAGMENTING PROJECTILE

In the model calculations, it was assumed that the shear band nucleation and growth gradually takes a larger portion of the total plastic strain until all is being absorbed by the bands. This means that after the threshold of 30% equivalent plastic strain is reached, the plastic strain taken in homogeneous deformation will continue to increase until fragmentation occurs. In our computed results the total equivalent plastic strain imposed is 60 to 80%. But the homogeneous plastic strain at the time of fragmentation is about 40%--the rest is used in producing bands. Experimental measurements indicate that there was only 35% homogeneous strain in the fragments. It may be necessary to reexamine the nucleation and growth processes to find means whereby the band formation mechanism can absorb a larger fraction of the induced plastic strain.

In the calculations, fragmentation was assumed to occur only by shear banding, whereas in some of the experiments microcracking in the outer layer participated in the fragmentation process. In future work the effects of microcracking must be included in the computations.

The computed fragment size distributions were obtained by varying mainly the nucleation rate coefficient. The Orowan equation appears to force a balance between nucleation and growth so that an increase in nucleation automatically results in less growth.

The fragment size distributions generally are linear on a semilog graph of cumulative number versus fragment radius. However, there are some interesting deviations from linearity in the calculations and the experiments. A concave upward portion for small radii results from the nucleation of more bands at a late stage. A concave downward portion at the large radius end results from reaching a fixed velocity limit such as the shear wave velocity.

### C. Conclusions and Recommendations

A constitutive model was developed to provide elastic-plastic stress-strain relations and to represent the shear banding phenomena observed in a series of fragmentation experiments in HF-1 steel. The model includes the nucleation of shear bands, growth of bands, and coalescence of bands to form fragments. The model accounts for stress, strain, and damage quantities in three dimensions, although it is used in one- and two-dimensional wave propagation codes. The model permits bands to grow in six specific orientations; these include the three that can occur in exploding cylinders plus three more that may be activated in impacts. The developing damage causes relaxation of the stress in directions normal to the planes of the bands; hence, growth of bands develops an anisotropy in the material.

The results of calculations with the shear band model include stress histories, and the size and number of bands in each orientation. The band distributions can be transformed to a fragment size distribution and summed over all the material to form a Mott plot.

Five experiments were simulated: four of HF-1 steel and one of Armco iron. Three cylinders of HF-1 showed good correspondence between experimental and computed fragment size distributions although the strain rates, geometry, and explosive power were significantly different for the three cases. The shell in the shape of a standard round of HF-1 and the Armco iron cylinder also showed good correspondence between experimental and computed fragment size distributions. The model gave the correct orientation for most of the bands, and partitioned the plastic strain between homogeneous strain and that absorbed during shear banding. These results indicate that the nucleation and growth processes of the model are appropriate and are able to account for strain rate, geometry, and pressure differences.

The present shear band model was developed for the current experimental data on HF-1 steel, and has been verified only for those data. These data are for cylindrical geometry which is not sensitive to many features of the model: hence, those features are not constrained by the data. To develop a model representing a wide range of material types, loading conditions, and geometries will require more experiments and coordinated model development. Specific areas of the model that are recommended for further study are the following:

- (1) The nucleation law requires verification experimentally, or modifications to match experiments. Associated experiments should be conducted for a broad range of strain rates and for various levels of damage. Especially important are experiments at the level of incipient damage, because at that point the nucleation process has been little affected by the development of damage.
- (2) The growth process should be examined in the light of the experimental data obtained in (1) above. The low-damage experiments should guide selection of a new function, if necessary, and evaluation of the parameters. Band motion may also be examined analytically by studying the behavior of a single band in homogeneous material. Band width should be determined as a function of strain rate, thermal conductivity, thermal strength reduction, and work hardening. These width calculations can probably be performed with a one-dimensional shear wave propagation code. Growth of the bands may be treated in the same way with a two-dimensional code. If both width and growth velocity are governed by homogeneous processes, these computational studies could aid greatly in defining some of the micro-mechanisms of the shear band process.

- (3) In impacts and fragmenting rounds, brittle fracture and shear bands combine to form fragments, and this combined process is not yet incorporated into the NAG (Nucleation and Growth) models. \* For this process, fragments as well as material at incipient damage levels should be examined. Then analytical techniques for joining the two damage processes should be developed.
- (4) In the model, both nucleation and growth in any direction are presumed proportional to the plastic shear strain in the relevant direction. This hypothesized relationship should be examined in the light of data from incipient damage experiments.

---

\* The combined process was accounted for in the work reported in Ref. 2 by permitting cells to undergo either brittle fracture or shear banding, but not both. In that study only one orientation of shear bands was permitted.

## V OBLIQUE ROD IMPACT - EXPERIMENTAL PHASE

The mechanisms for fracture of a long-rod penetrator under high velocity impact (either oblique or perpendicular) with an armor plate are inadequately understood. Large pressures and large shear deformations at high strain rates make this a difficult problem to analyze or model.

In a preliminary effort to establish the key penetrator failure modes, we performed the following tasks:

- (1) Examined metallographically the distal ends of steel and tungsten alloy long-rod penetrators recovered from experiments at Lawrence Livermore Laboratories (LLL).
- (2) Examined metallographically fragments that LLL recovered from the proximal end of obliquely-impacted tungsten alloy rods.
- (3) Performed a series of oblique-angle long-rod penetrator experiments using HF-1 steel to study break-up characteristics as a function of velocity.
- (4) Examined the fragments recovered from a long-rod tungsten alloy penetrator perpendicular impact performed at the Ballistic Research Laboratory.

These activities are described in detail in the following pages.

### A. LLL Experiments

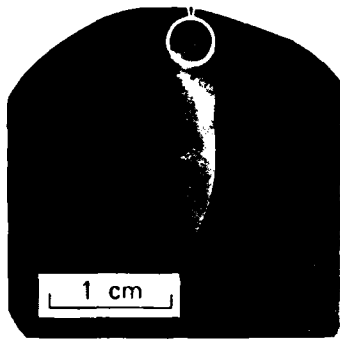
From Dr. John Scudder and Mr. Leroy Hoard of LLL, we obtained fragments recovered from scale-model long-rod penetrator oblique-impact tests performed in their laboratories. The projectiles all had a diameter of 3.9 mm, a length of 39 mm, and a hemispherical nose, and were impacted at a velocity of  $\approx 1$  km/sec and a  $55^\circ$  angle of obliquity into a target of mild steel with an overlay of AD85\* alumina ceramic.

---

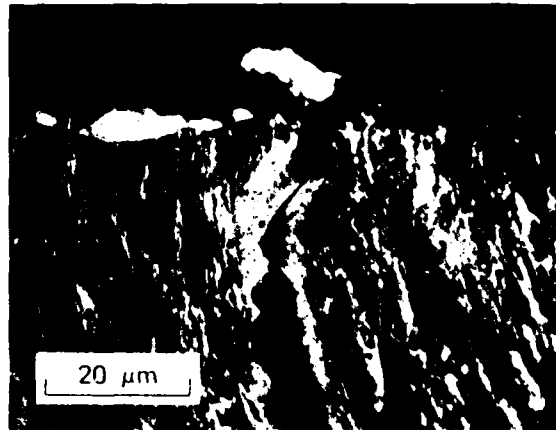
\* Product of Coors Porcelain Co., Golden, Colorado.

We first examined the distal halves of the projectiles---the only fragments large enough to be recovered without any special recovery techniques. Figure 22(a) shows a metallographic specimen made by cutting through the axis of the specimen parallel to the plane of greatest bending (all subsequent specimens were cut in the same way). The material is Saratoga AISI-01 oil hardened tool steel ( $R_c \approx 48$ ). Photomicrographs of a region near the forward edge of the specimen show clearly a shear band intersecting the edge and a tensile crack extending part way down the length of the shear band. Since this was the only internal crack visible in this specimen and since there was also a transformed region (indicating a shear band) along the fractured forward edge of the specimen, there is evidence that shear banding and subsequent tensile failure along a shear band is an important failure mechanism for a steel long-rod penetrator, at least in the distal regions.

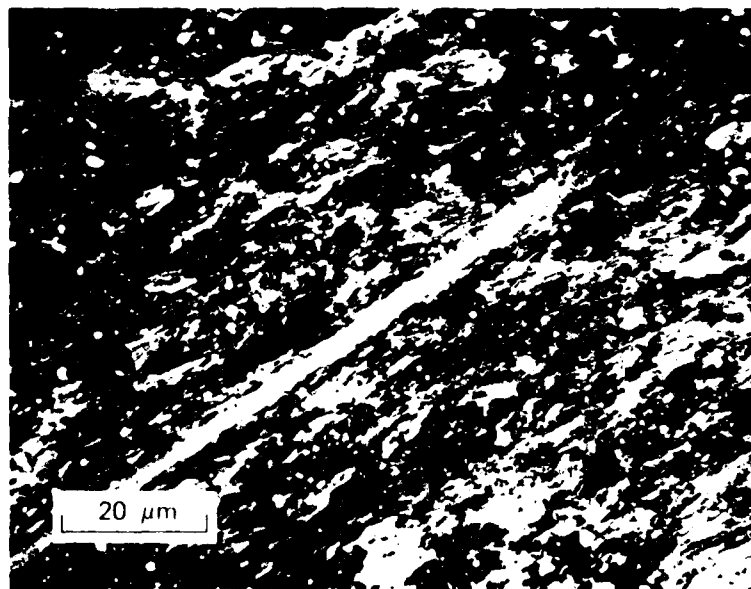
We next examined the distal halves of tungsten alloy projectiles. The alloy contained 90% tungsten, 7% nickel, and 3% iron by weight, and was composed of nearly spherical tungsten grains  $\approx 5 \mu\text{m}$  in diameter in a matrix. Unlike steel, tungsten does not exhibit a readily observed phase change under high temperatures, which can be used as a clear indicator of shear banding. However, this tungsten alloy does have an advantage over some steel in that strain deformation is indicated by grain elongation. Figure 23 shows three photomicrographs from a tungsten penetrator---one taken from an undeformed region, showing largely circular grain cross sections; one from a region of large but primarily homogeneous shear deformation, showing grain cross sections with aspect ratios of around 4 to 1; and one from a region along the proximal edge where inhomogeneous shear deformations have elongated grains to aspect ratios as high as 20 to 1, and caused shear cracking.



(a)



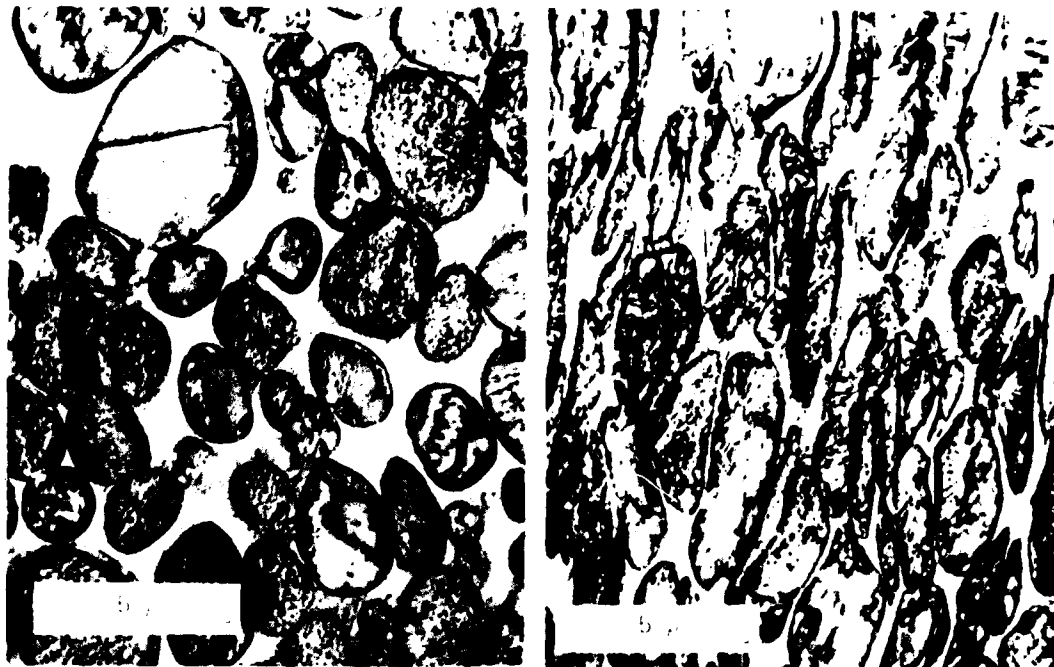
(b)



(c)

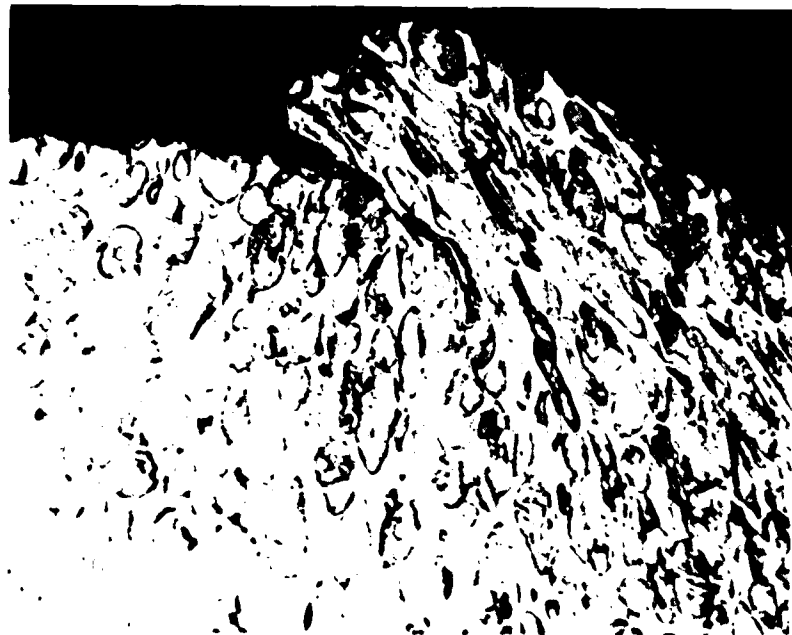
MP-5084-16

FIGURE 22 SPECIMEN (a) FROM DISTAL END OF OBLIQUELY IMPACTED TOOL STEEL LONG-ROD PENETRATOR FIRED AT LAWRENCE LIVERMORE LABORATORY WITH PHOTOMICROGRAPHS (b) AND (c) SHOWING SHEAR BANDING



(a)

(b)



(c)

MP-5084-19

FIGURE 23 PHOTOMICROGRAPHS OF DISTAL HALF OF OBLIQUELY IMPACTED TUNGSTEN ALLOY LONG-ROD PENETRATOR SHOWING (a) UNDEFORMED REGION, (b) REGION OF PRIMARILY HOMOGENEOUS SHEAR DEFORMATION, AND (c) REGION OF LARGE INHOMOGENEOUS SHEAR DEFORMATION RESULTING IN SHEAR CRACK

We have thus seen evidence of failure due to shear banding or inhomogeneous shear deformations in the distal region of both steel and tungsten alloy long-rod penetrators. Since the shear strains and strain rates would be higher near the proximal ends, this type of failure mechanism should be even more important there. To test this belief, we suggested to Dr. Scudder and Mr. Hoard a means of recovering fragments from the proximal halves of obliquely impacted long-rod penetrators by capturing them in a relatively soft rubber-like substance. They subsequently performed such experiments, and we examined several recovered tungsten alloy specimens one of which is shown in Figure 24. The structure is very similar to that shown in Figure 23. In Figure 24(b), a gradual transition from no shear deformations to large shear deformations takes place across the width of the specimen. And in Figure 24(c), narrow bands of extremely high shear deformation are seen between regions of moderate shear deformation. We cannot know precisely where in the penetrator this fragment originated, but it was within the proximal half.

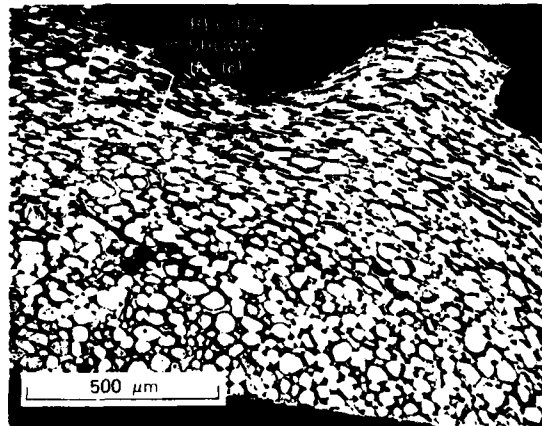
Our conclusion is that failure by shear banding or inhomogeneous shear deformation occurs over a large region in a long-rod penetrator.

#### B. SRI Experiments

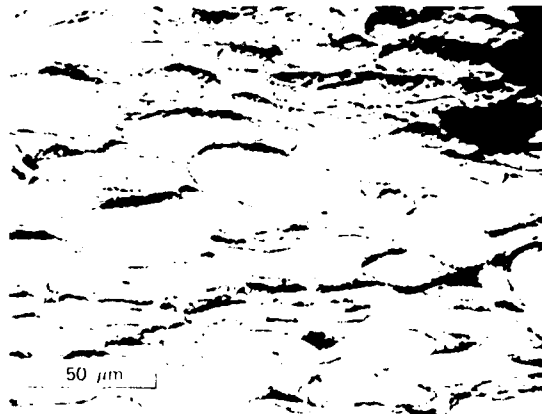
SRI's smooth-bore-gun facility, which had been used in previous armor penetration experiments,<sup>1</sup> was modified for use in scale-model long-rod penetrator oblique impact experiments. Hemispherical-nosed HF-1 steel projectiles 3.175 mm in diameter and 38.1 mm long were fired at a 55° angle of obliquity into 1-cm-thick steel armor plates. The relatively thick armor was chosen so as to minimize damage to the target, and thereby make the projectile failure easier to model computationally. HF-1 steel was chosen because it is a material for which dynamic fracture parameters are known.



(a)



(b)



(c)

MP-5084-17

**FIGURE 24** FRAGMENT (a) RECOVERED FROM OBLIQUELY IMPACTED TUNGSTEN ALLOY LONG-ROD PENETRATOR FIRED AT LAWRENCE LIVERMORE LABORATORY WITH PHOTOMICROGRAPHS SHOWING EVIDENCE OF LARGE HOMOGENEOUS (b) AND NONHOMOGENEOUS (c) SHEAR DEFORMATIONS

We fired a series of shots at impact velocities ranging from 0.17 to 0.97 km/sec, and the results are shown in Figure 25. As the impact velocity increases to about 2/3 km/sec, the projectiles become more and more bent, eventually separating into several pieces. However, at higher velocities, the bending decreases and the projectiles undergo large cross-sectional deformations in their proximal regions. In all cases, target damage was negligible.

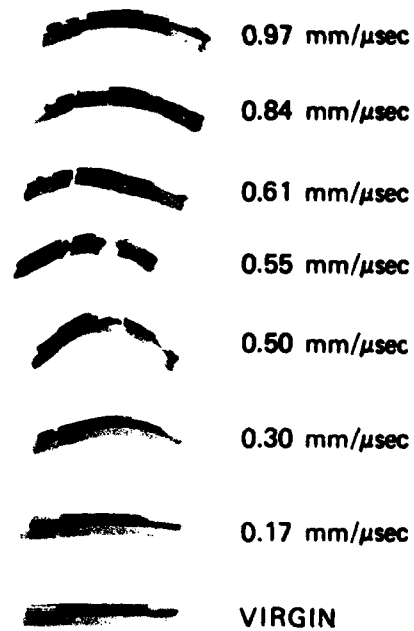
The damaged projectiles were sliced in half along their plane of maximum bending, polished, etched, and examined metallographically. The surfaces of separation appeared to result from brittle, or tensile failure, but there was no evidence of either shear banding or tensile failure in the proximal region. The higher velocity shots exhibited a transformed region along the outer, flattened surface, which undoubtedly resulted from the projectile sliding along the surface of the target as it was being deflected.

#### C. BRL Experiments

Late in the program Dr. Zukas of Ballistics Research Laboratory sent us material recovered from a long-rod penetrator impact experiment performed at BRL. The material was the same tungsten alloy used in the LLL penetrators; however, the scale was larger--the hemispherical-nosed projectile was 0.79 cm in diameter and 7.9 cm in length, and the impact occurred at 0.850 km/sec with a  $0^\circ$  angle of obliquity into a 2.54-cm-thick steel target.

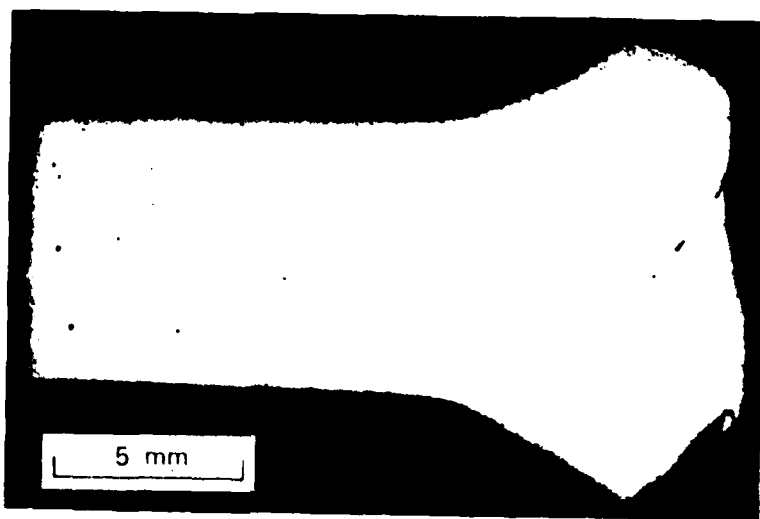
The recovered fragments included the distal quarter and an assortment of small fragments. Figure 26 shows a slice through the large fragment, with a close-up of the area that contains what appears to be a long partially separated shear band. Detailed photomicrographs, seen in Figure 27, prove that it is indeed a shear band. The high magnification insets clearly show bands less than 10  $\mu\text{m}$  wide, across which the two opposite surfaces

55° IMPACT HF-1 PROJECTILES



MP-5084-18

FIGURE 25 HF-1 STEEL LONG-ROD PROJECTILES  
RECOVERED FROM OBLIQUE IMPACT  
TESTS AT SRI INTERNATIONAL



(a)



(b)

MP-5084-24

**FIGURE 26** POLISHED SECTION (a) THROUGH BRL TUNGSTEN ALLOY LONG-ROD PENETRATOR, WITH CLOSE-UP (b) OF SHEAR BAND

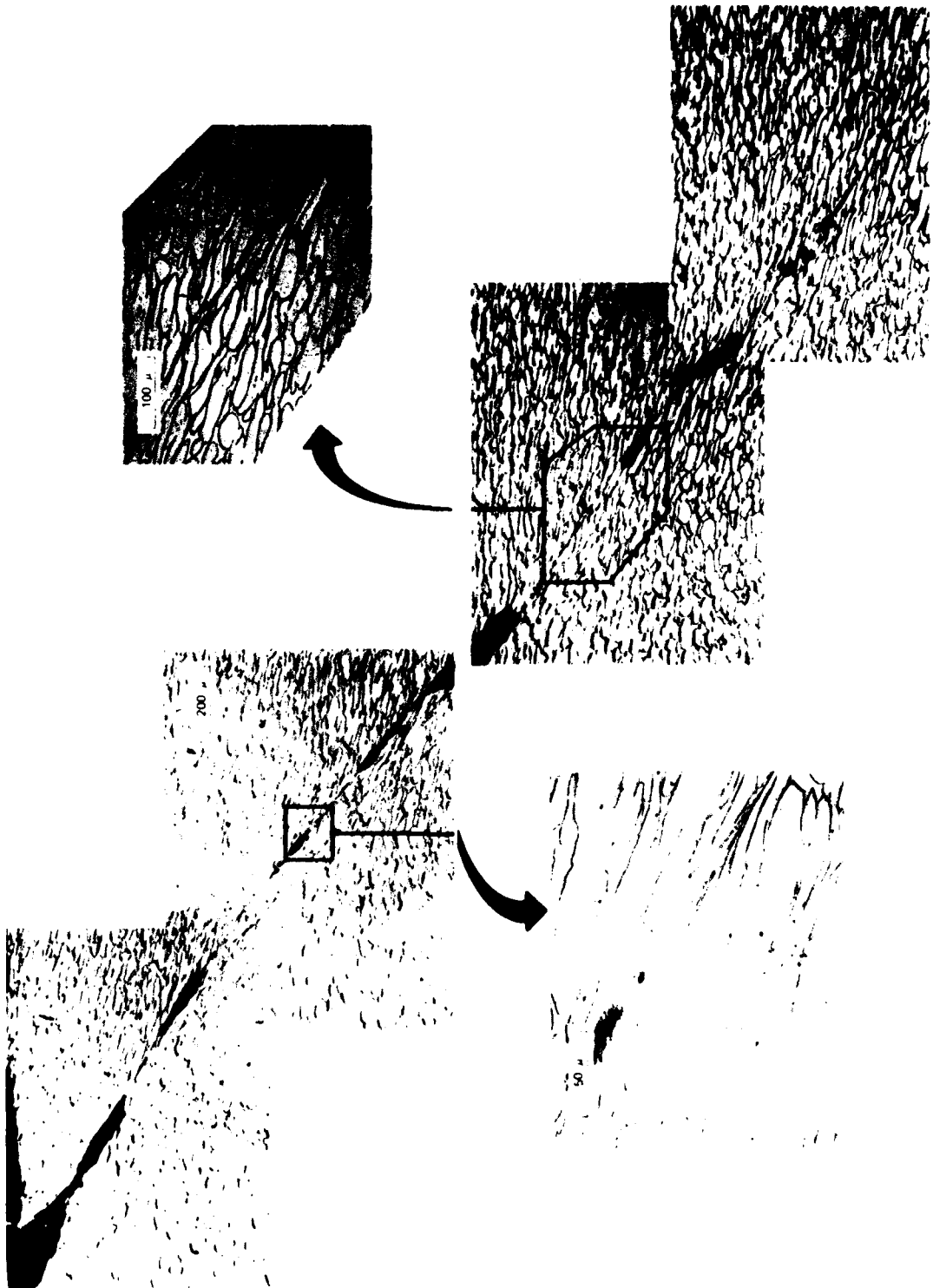


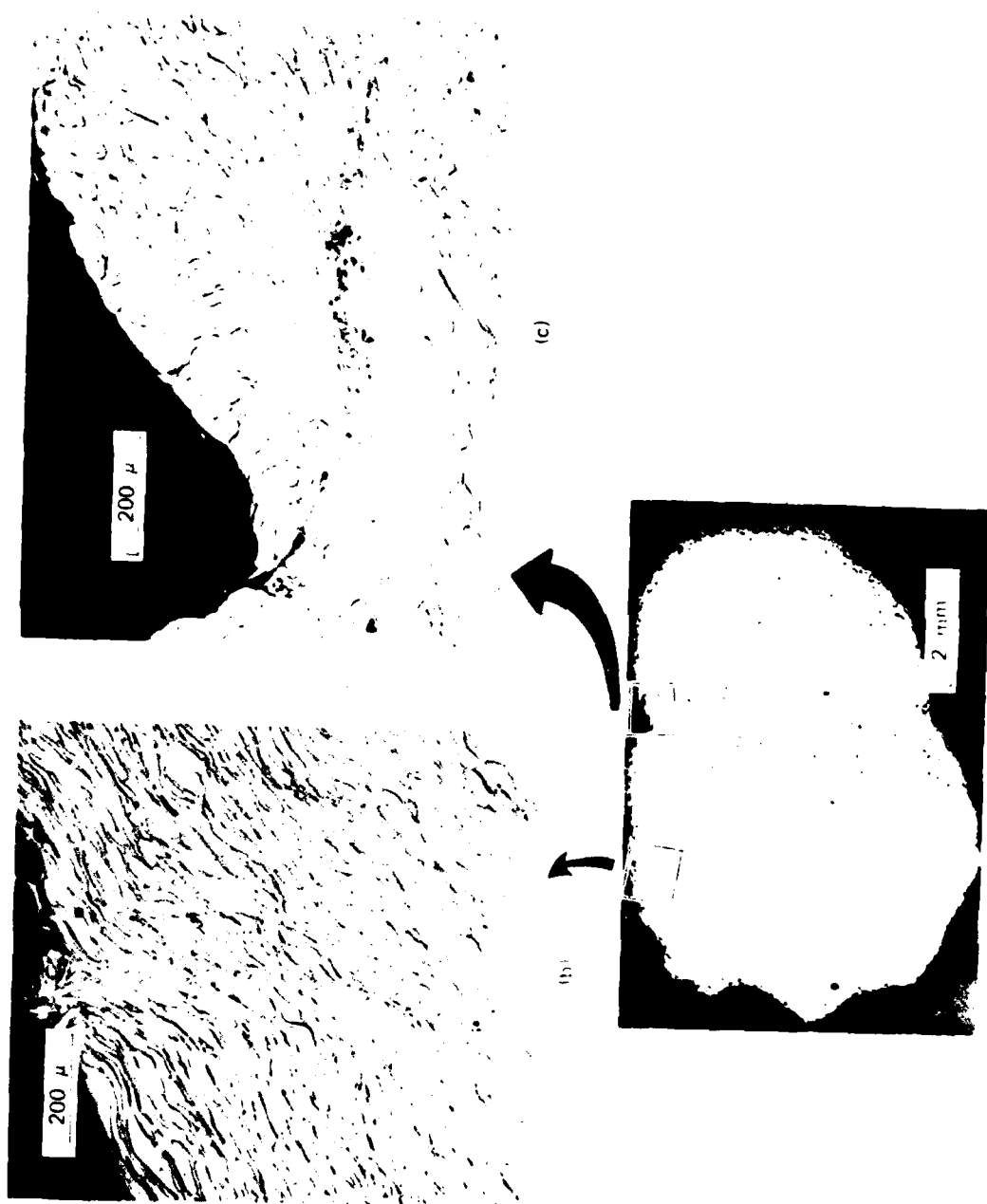
FIGURE 27 DETAILED PHOTOMICROGRAPHS OF SHEAR BAND IN BRL  
TUNGSTEN ALLOY LONG-ROD PENETRATOR

have slid as much as 50  $\mu\text{m}$  or more. The inset at lower left shows two such bands running parallel to each other about 60  $\mu\text{m}$  apart.

A polished section through one of the smaller fragments is seen in Figure 28, along with two high magnification insets revealing shear-banded regions. These particular bands are quite curved, which indicates either that the material was in a highly nonuniform state of shear strain prior to the banding or that the material continued to undergo large homogeneous shear deformations after the band formed. Also, the highly deformed grain that exists away from the banded regions is indicative of the toughness of this alloy, which will sustain large amounts of shear strain before banding.

D. Conclusions

Shear banding is a principal mode of material failure in high-velocity impacts of tungsten alloy and steel long-rod penetrators, although the SRI experiments indicate that tensile fracture may also be important, particularly at larger impact angles.



MP-5084-25

FIGURE 28 POLISHED SECTION (a) THROUGH FRAGMENT FROM BRL TUNGSTEN ALLOY LONG-ROD PENETRATOR IMPACT, WITH CLOSE-UPS (b) AND (c) OF SHEAR-BANDED REGIONS

## VI OBLIQUE ROD IMPACT-COMPUTATIONAL PHASE

Oblique impact calculations were conducted with a two-dimensional wave propagation computer program. The calculations simulate a plate impacting on edge another plate at an oblique angle. Both the conditions in which the projectile sticks to the target and in which it slips were treated. For each condition, impact angles of  $30^\circ$ ,  $45^\circ$ , and  $55^\circ$  to normal were considered.

The purpose of the calculations was to examine the phenomena associated with oblique impacts to gain insight into the reasons for breakup of the projectile and the mechanism of damage in the impact region. We examined the regions of fracture damage and locations near the point of impact where shear, compression, and bending stresses occurred, and we noted how these locations changed with the degree of slip along the target. We used an active fracture damage model (with stress-relaxation associated with damage) to see whether the damage would significantly affect subsequent bending and projectile breakup.

The computer program used is called TROTT. It is a two-dimensional, finite-difference Lagrangian code, and is similar to HEMP and TOODY.

Three features made it attractive for this problem:

- (1) TROTT is small; all storage is in core.
- (2) The array storage is arranged to permit very large data storage for cells undergoing fracture.
- (3) The code is simple and easy to modify for the special impact boundary conditions.

During the project, modifications were made to allow improved treatment of the impact problem.

The remainder of this section treats the special modifications made to the code TROTT, the geometries used in the calculations, and the results of the simulations.

A. Code Modifications

The TROTT code was altered to include a special nonnormal impact condition and triangular cells. The projectile is divided into the usual discrete finite-difference cells, whereas the target is treated as rigid and immovable. The rigid target was used for simplicity because the main interest was in breakup of the projectile at some distance back from the impact plane. It was felt that the conditions of sticking and slipping would bracket the boundary conditions actually experienced by a projectile.

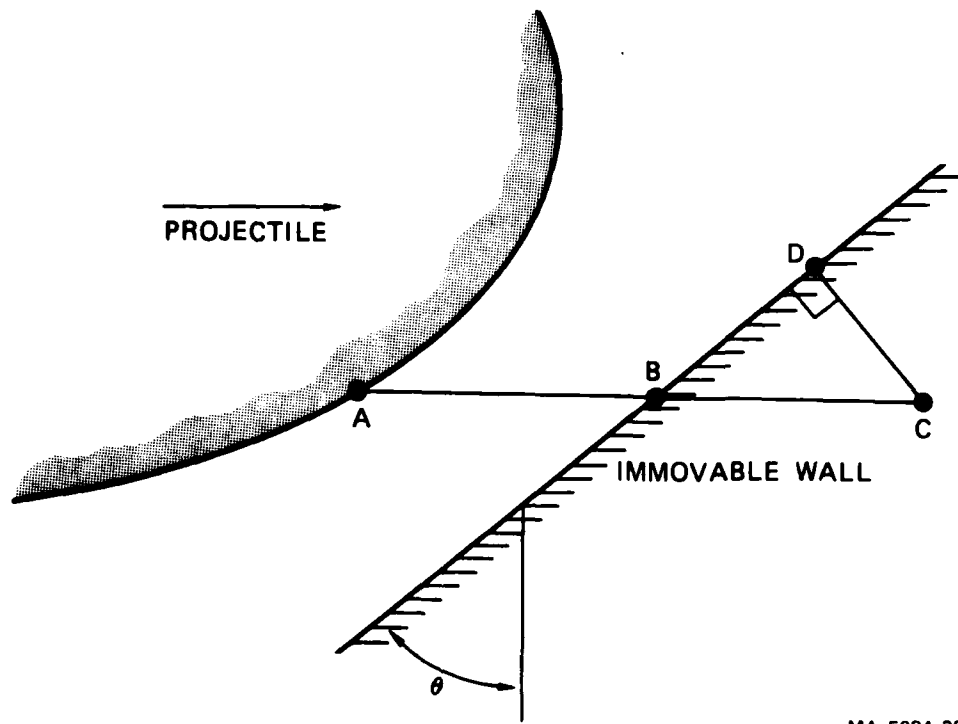
For the slipping boundary condition, coordinate motion was permitted as usual until the point reached the target. Thereafter only tangential motion along the target face was allowed. For example, in Figure 29, Point A moves until it strikes the target at B and then slips to point D. Let  $(x_1, y_1)$  represent one point on the target. Then the equation of the target is

$$x = x_1 + (y - y_1) \tan \theta \quad (33)$$

where  $\theta$  is the angle of the target measured so that  $\theta = 0$  is a normal impact. Then if a coordinate with the initial position  $(x_A, y_A)$ , that is point A in Figure 29, moves with velocities  $\dot{x}, \dot{y}$ , impact occurs at point B at a time

$$\delta t = \frac{x_1 - x_A + (y_A - y_1) \tan \theta}{\dot{x} - \dot{y} \tan \theta} \quad (34)$$

If  $\delta t$  is less than the current time step in the wave propagation calculations (i.e., point C is beyond point B), then the impact coordinate locations are at B



MA-5084-30

FIGURE 29 SLIDING OR STICKING CONDITIONS AT OBLIQUE TARGET

$$\begin{aligned}x_B &= x_A + \dot{x} \delta t \\y_B &= y_A + \dot{y} \delta t\end{aligned}\tag{35}$$

After the impact, cell motion is tangential. The tangential velocity is

$$V_T = \dot{x} \sin \theta + \dot{y} \cos \theta .$$

The x and y coordinates of this velocity are

$$V_x = V_T \sin \theta$$

$$V_y = V_T \cos \theta .$$

The final coordinate locations are then

$$x_D = x_B + V_x (\Delta t - \delta t)$$

$$y_D = y_B + V_y (\Delta t - \delta t)$$

where  $\Delta t$  is the current time step.

The sticking boundary condition required that no motion occurs after impact. First, the coordinate motions were computed in the usual way. If a point had penetrated the target plane (i.e., point C in Figure 29), it was repositioned at the point where it first touched the target, point B, using Equation 35. Velocities of the impacting coordinates were set to zero.

A triangular cell feature was added to TROTT to handle the large distortion problem near the plane of impact. The usual quadratic cells become excessively distorted in the large shear flows near the front and they either halt the calculation or require rezoning of the cells.

The triangular cells are very resistant to cell distortion and therefore can follow the impact somewhat better. The triangular cells were constructed by simply dividing quadrilateral cells in two, and computing strain and stress separately for each half. The analysis followed the lines suggested by Johnson<sup>6</sup> for impact calculations.

Following incorporation of the triangular cells, we performed several short calculations with only a few cells to examine the new properties. The study, though not exhaustive, was adequate to guide our use of the triangular cells and to interpret the results. It revealed the following:

- The triangle Q artificial viscosity stresses used with quadrilateral cells are also needed with triangular cells to reduce oscillations.
- The time steps required for stability of triangular cell calculations are the same as those of the quadrilateral cell:

$$\Delta t = 0.9 \frac{\Delta X}{C}$$

where  $\Delta X$  is the length of the shortest side,  $C$  is the sound speed augmented to account for artificial viscosity, and 0.9 is the safety factor.

- In pure compression a pair of triangular cells each give stresses identical to the quadrilateral cell from which they were made.
- In shear, one of the triangular cells in a pair goes into tension, the other into compression, with the average of the two stresses being about that of a single quadrilateral cell. These stresses are often quite large, thus giving a misleading picture of the stress state.

The last item above shows that only simple equations of state should be used for the triangular cells. More complex constitutive relations with threshold levels and extreme nonlinearities would only give misleading results. Hence, in our impact calculations we used the triangular cells only for the first few rows of cells at the head of the projectile and permitted only elastic-plastic behavior in them.

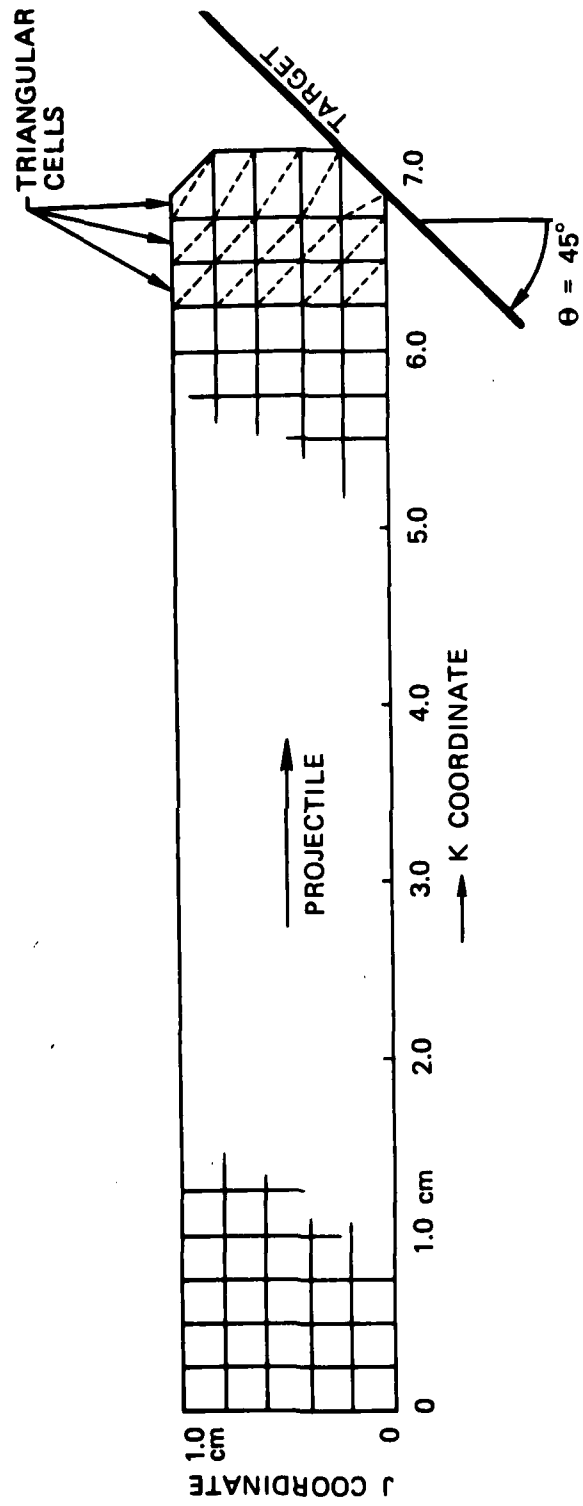
#### B. Simulations

The geometry used in the calculations is shown in Figure 30. Two-dimensional plane strain conditions are used. The projectile slab has a rounded nose as shown so that one side of one cell is in continuous contact with the target at impact. A projectile velocity of  $1 \text{ mm}/\mu\text{sec}$  was used in all cases. The projectile slab, which is Armco iron, is treated as an elastic-plastic material in compression and with brittle fracture (BFRAC subroutine) in tension. In addition to the usual stress and motion results, moments and forces in the impacting slab were computed.

The resulting shapes of some of the projectiles after  $14 \mu\text{sec}$  is shown in Figures 31 to 36.

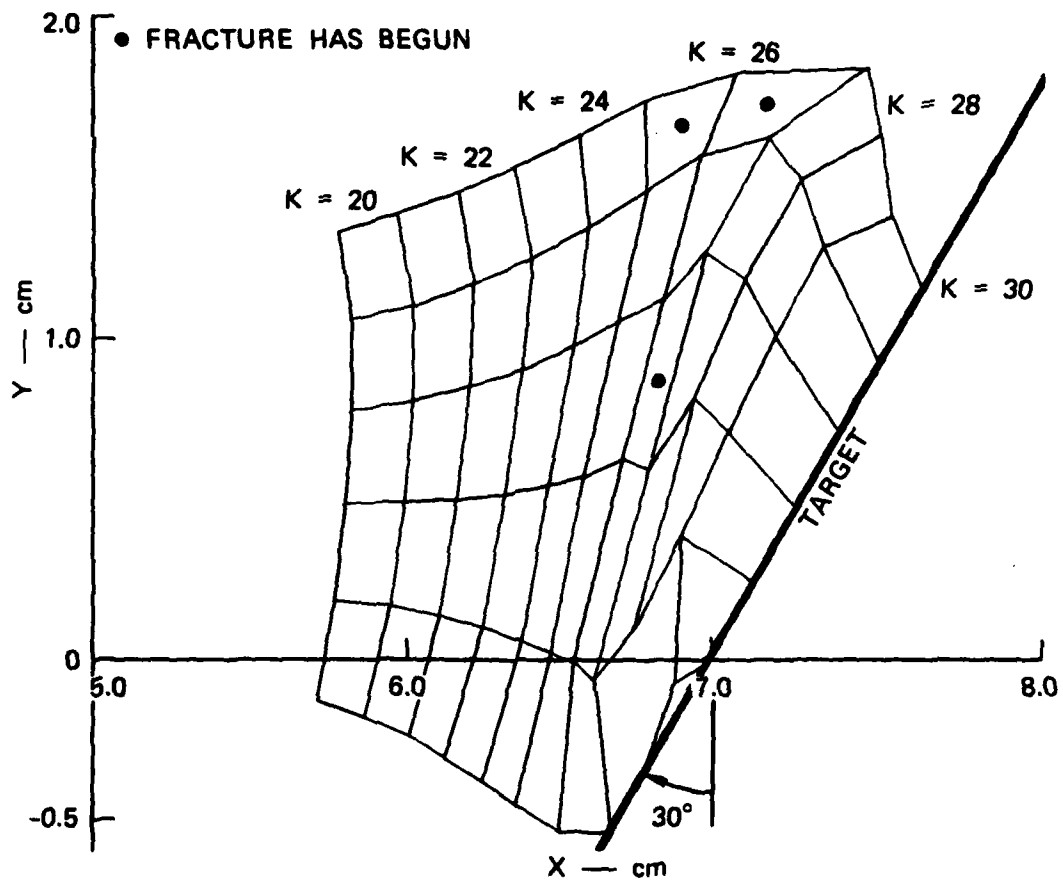
Following impact, the projectile is gradually deformed so that it is in contact with the target over the entire projectile nose and for some distance along the side nearest the target. Projectile deformations appear as high shears that distort the impact-plane cells and elongate the cells just behind the impact. The cells are elongated through the thickness, suggesting a tendency toward splitting. Cells on the side of the projectile farthest from the target are also elongated in the axial direction, indicating a tendency to break in bending.

In all cases, the projectile tends to enlarge radially. This expansion is more evident for the shallower angles of impact. Associated with this is fracture in the radial direction by cells near the center of the projectile and axial fracture on the projectile surface farthest from impact.



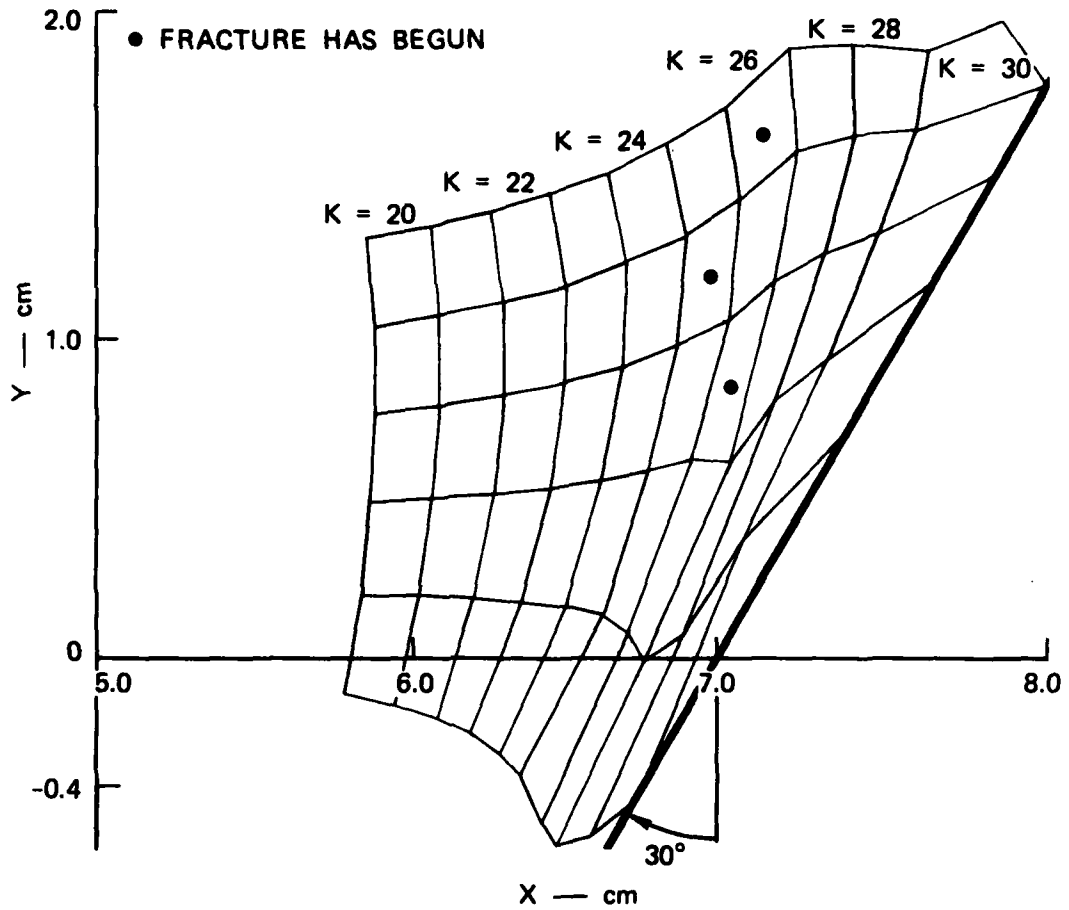
MA-5084-31

FIGURE 30 GEOMETRY FOR SIMULATIONS OF PROJECTILE PLATE IMPACTING A WALL AT AN OBLIQUE ANGLE



MA-5084-32

FIGURE 31 DISTORTION AND DAMAGE NEAR FRONT OF PROJECTILE PLATE FOR 30° OBLIQUITY, NO SLIPPING



MA-5084-33

FIGURE 32 DISTORTION AND DAMAGE NEAR FRONT OF PROJECTILE PLATE FOR 30° OBLIQUITY, SLIPPING

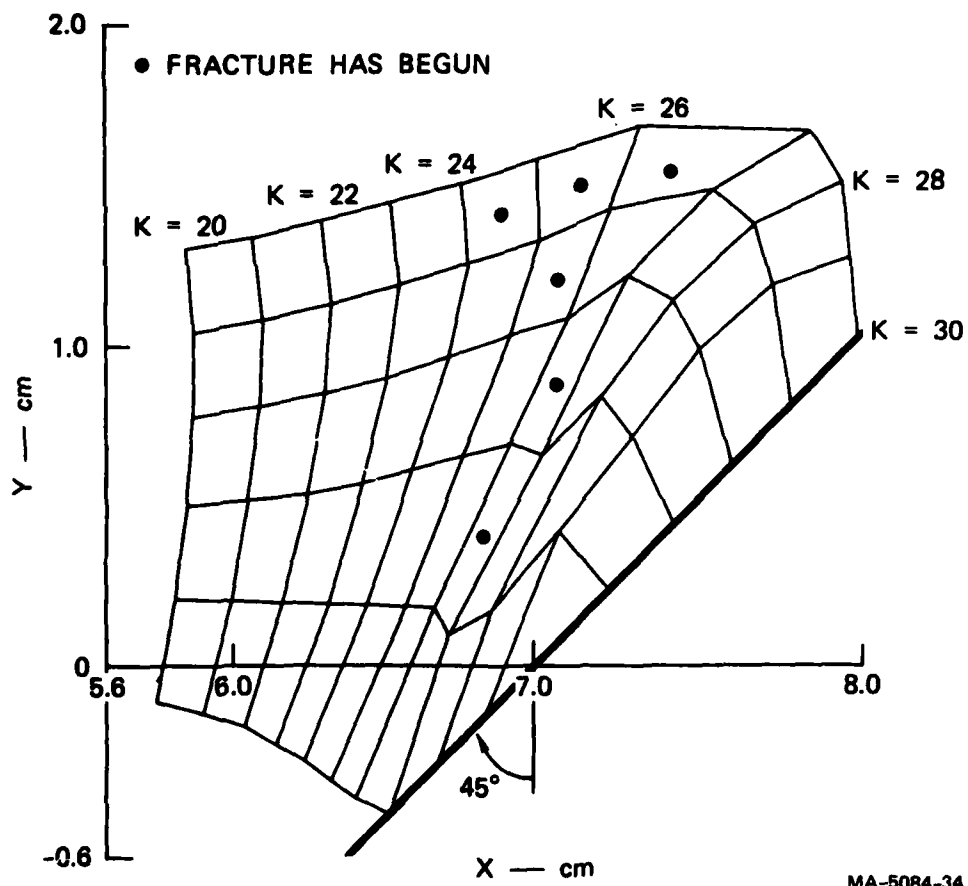


FIGURE 33 DISTORTION AND DAMAGE NEAR FRONT OF PROJECTILE PLATE FOR 45° OBLIQUITY, NO SLIPPING

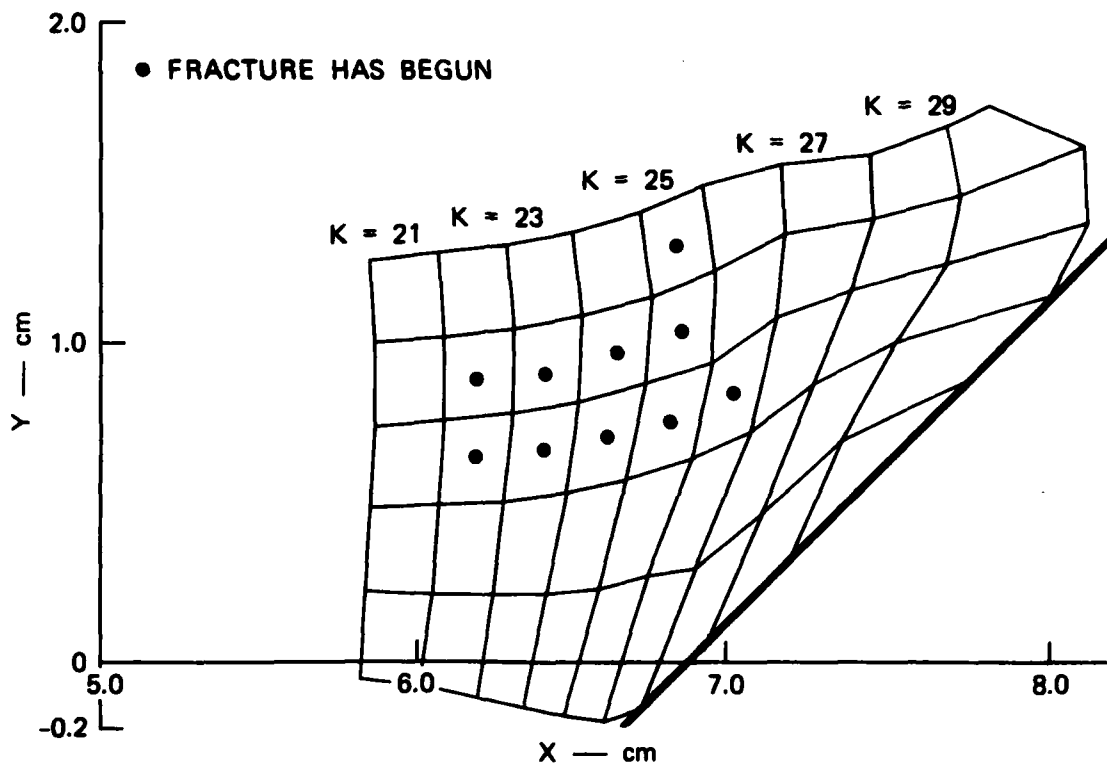
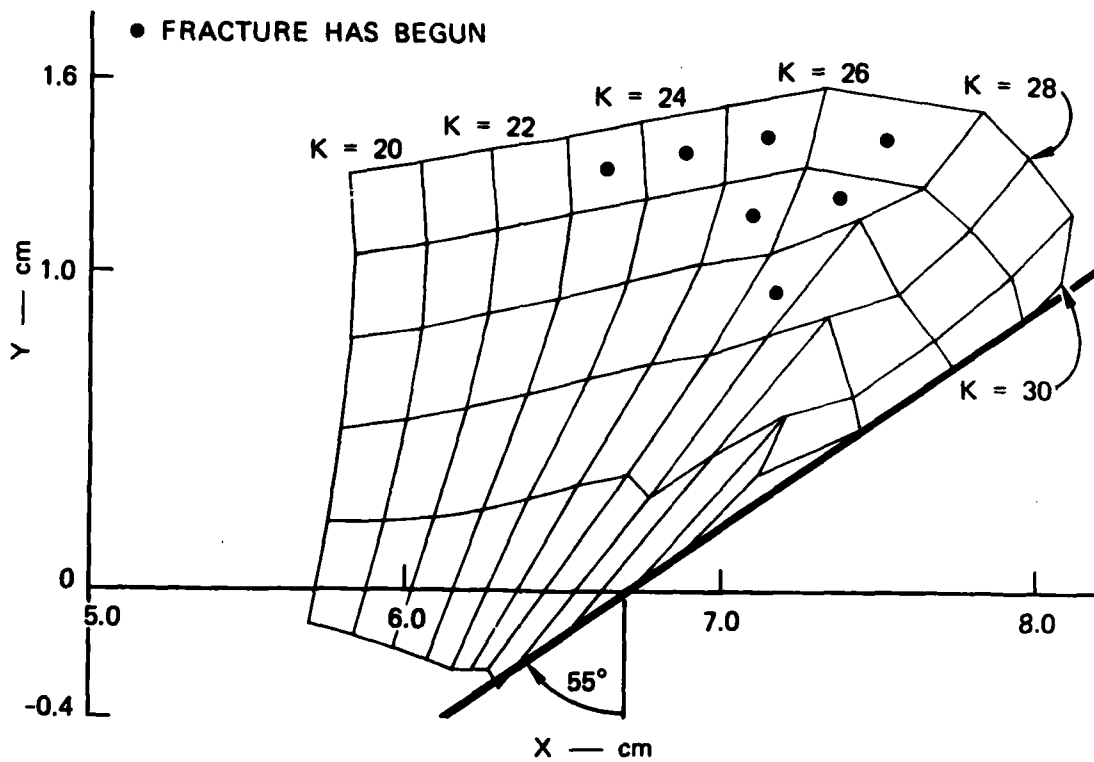


FIGURE 34 DISTORTION AND DAMAGE NEAR FRONT OF PROJECTILE PLATE FOR 45° OBLIQUITY, SLIPPING



MA-5084-36

FIGURE 35 DISTORTION AND DAMAGE NEAR FRONT OF PROJECTILE PLATE FOR 55° OBLIQUITY, NO SLIPPING

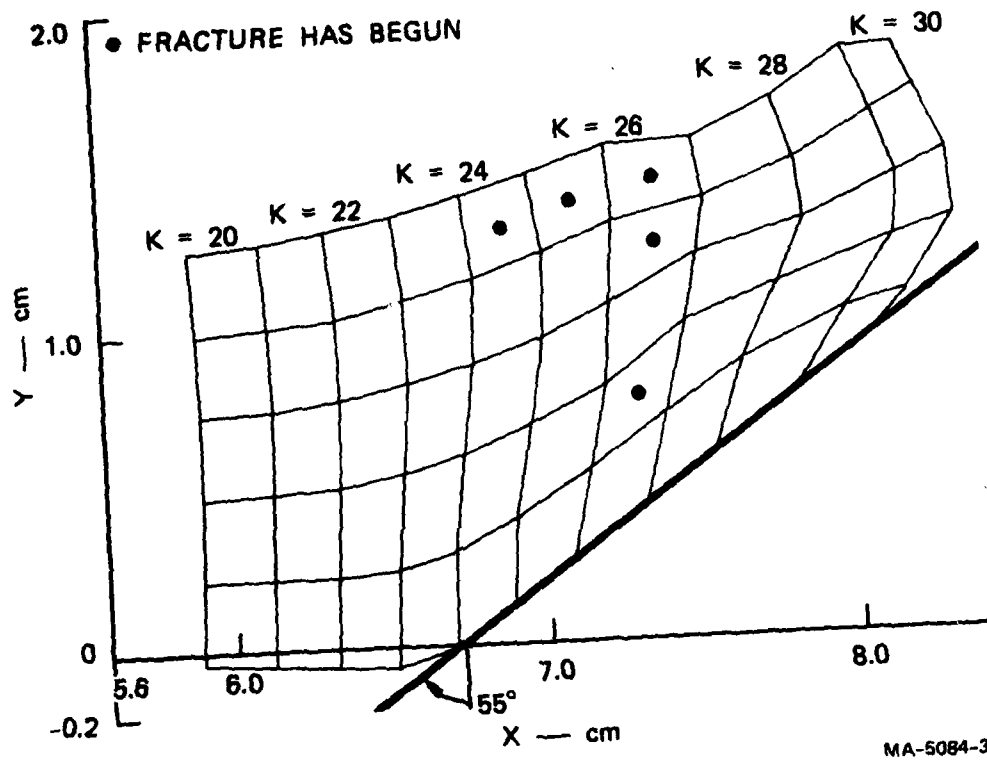
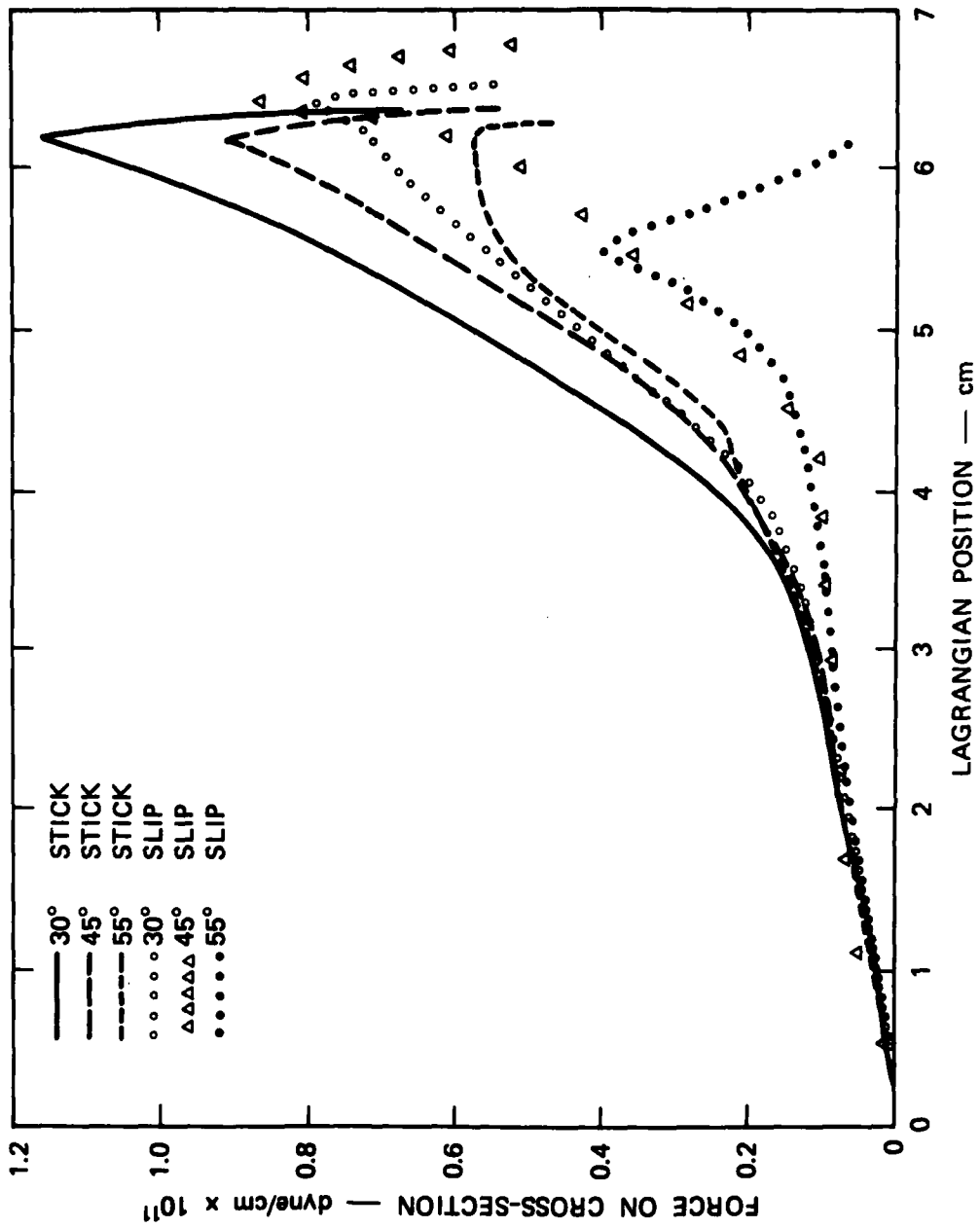


FIGURE 36 DISTORTION AND DAMAGE NEAR FRONT OF PROJECTILE PLATE FOR 55° OBLIQUITY, SLIPPING

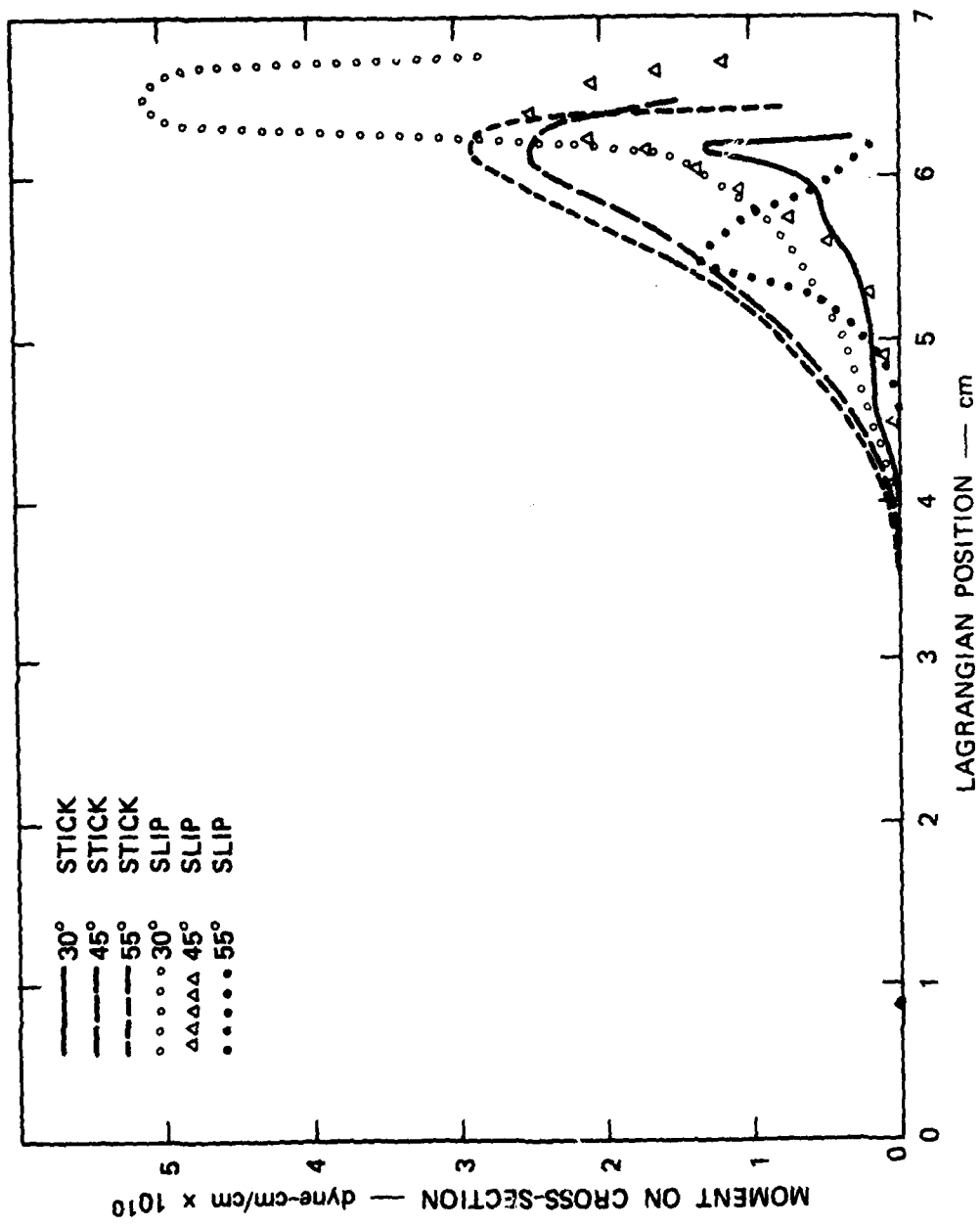
Graphs of the forces and bending moments on sections through the projectile at 14  $\mu$ sec are shown in Figures 37 and 38. These values are computed by summing stresses from cells with the same initial Lagrangian position. The force and moment distributions build up gradually with time toward the configurations shown in Figures 37 and 38, but they are fairly constant by 14  $\mu$ sec. A comparison of forces in these figures shows that the forces have a higher amplitude and extend deeper into the projectile for the sticking case. The moments show a similar trend for the 45° and 55° impacts, but a contrasting trend is shown at 30°. These moment variations should be studied further with calculations performed for longer durations. The results also shed light on the SRI oblique impact experiments reported in the previous section. Comparison of Figures 32, 34, and 36 show that the shear strain in the projectile nose is dramatically less for the 55° (slipping) impact than for impacts at lower angles. Thus, shear banding should become less prevalent at higher impact angles.

Future work should include the shear banding model as well as the tensile fracture model, and would help us gain an understanding of the interaction of these competitive failure modes.



MA-5084-38

FIGURE 37 FORCE TRANSMITTED BY THE IMPACTING PLATE AS A FUNCTION OF DISTANCE ALONG THE PLATE



MA-5084-39

FIGURE 38 BENDING MOMENTS IN THE IMPACTING PLATE AS A FUNCTION OF DISTANCE ALONG THE PLATE

## APPENDIX A

### EQUIVALENT PLASTIC STRAIN FOR A RADIALLY EXPANDING CYLINDRICAL TUBE

Consider a cylindrical tube, loaded by an internal pressure, expanding radially outward with no motion in the axial direction. What is the equivalent plastic strain, averaged across the wall thickness, that the cylinder has undergone after expansion and after the internal pressure has been relieved?

Consider the portion of a cylindrical tube shown in Figure 39. Let  $r \equiv$  radius of the inner surface,  $R \equiv$  radius of outer surface,  $a = R - r \equiv$  wall thickness, and  $x = \frac{1}{2}(R+r) \equiv$  radius of the midpoint. Furthermore let subscripts  $o$  and  $f$  refer to the original and final dimensions, respectively.

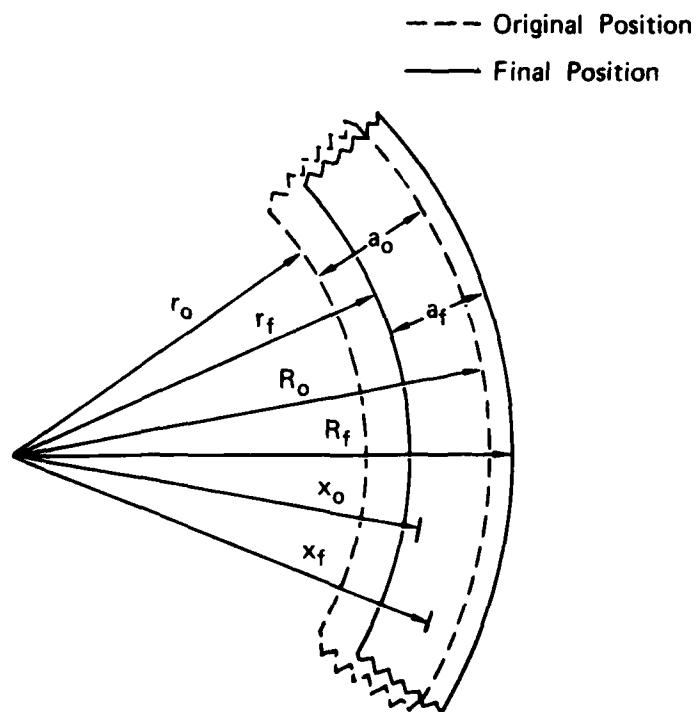
Our assumptions are that there is no axial strain ( $\epsilon_z = 0$ ) and that the final volume strain is zero ( $\epsilon_r + \epsilon_\theta + \epsilon_z = 0$ ). Therefore,  $\epsilon_r = -\epsilon_\theta$ , and furthermore, the cross-sectional area of the tube remains constant (i.e.,  $a_o x_o = a_f x_f$ , or  $\frac{a_f}{a_o} = \frac{x_o}{x_f}$ ).

\*  
Now we define the equivalent plastic strain:

$$\bar{\epsilon}^P \equiv \sqrt{\frac{3}{2}} \cdot \sqrt{(\epsilon_r^P)^2 + (\epsilon_\theta^P)^2 + (\epsilon_z^P)^2}$$

where the superscript P on the strain terms denotes plastic strains,

\* This definition of equivalent plastic strain coincides with the definition of the differential  $d\bar{\epsilon}^P$  in Eq. 4 if the ratios  $d\epsilon_\theta^P/d\epsilon_r^P$  and  $d\epsilon_z^P/d\epsilon_r^P$  are constant throughout the flow. For  $\epsilon_z = 0$ , the ratios are constant.



MA-5084-22

FIGURE 39 GEOMETRY AND NOMENCLATURE FOR EQUIVALENT PLASTIC STRAIN DERIVATION

AD-A084 029

SRI INTERNATIONAL MENLO PARK CA F/G 12/1  
DEVELOPMENT AND APPLICATION OF A COMPUTATIONAL SHEAR BAND MODEL--ETC(U)  
MAR 80 D C ERLICH, L SEAMAN, D A SHOCKEY DAAD05-76-C-0762

UNCLASSIFIED

ARBRL-CR-00416

NL

2 of 2

60

10/10/79

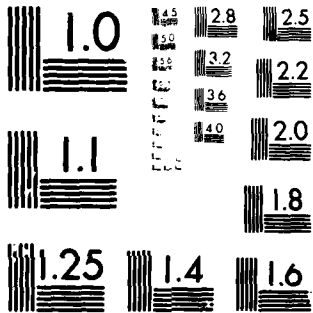
■

END

DATE

FILED

DTIC



MICROCOPY RESOLUTION TEST CHART  
NATIONAL BUREAU OF STANDARDS-1963-A

which are equal to the final strains, since there are no residual stresses. The strains may now be computed based on the change of wall thickness, or on the change of radius. A change in thickness causes a change in radial strain,  $d\epsilon_r = da/a$ . Then

$$\epsilon_r = \int_{a_0}^{a_f} \frac{da}{a} = \ln \left( \frac{a_f}{a_0} \right) = \ln \left( \frac{R_f - r_f}{R_0 - r_0} \right)$$

Similarly a change in radius alters the circumference and induces a circumferential strain  $d\epsilon_\theta = dr/r$ .

$$\epsilon_\theta = \frac{dr}{r} = \ln \left( \frac{r_f}{r_0} \right) = \ln \left( \frac{R_f + r_f}{R_0 + r_0} \right)$$

In these expressions  $\epsilon_r$  and  $\epsilon_\theta$  represent average strains through the wall thickness. The equivalent plastic strain is then

$$\begin{aligned} \bar{\epsilon}^P &= \sqrt{3} |\epsilon_r| \\ &= \sqrt{3} |\epsilon_\theta| \end{aligned}$$

For intact material the strains based on thickness or radius changes are equivalent. But for fracturing material, the thickness measurement gives the homogeneous plastic strain, whereas the radius gives the total plastic strain (homogeneous plus that takes by the bands).

## APPENDIX B

### USE OF THE SHEAR BANDING SUBROUTINE IN WAVE PROPAGATION CALCULATIONS

The shear band subroutine SHEAR2 is used in one- and two-dimensional wave propagation codes to predict shear banding and fracture under high rate loadings. The procedure for inserting the subroutine into wave propagation codes is described below. A brief outline of the subroutine is given, but the basic equations are derived in Chapter IV. The shear banding parameters are described and some guidance is given for choice of values. The subroutine input data and output are described and samples are given, together with a listing of the subroutine.

#### 1. Insertion Procedure

A wave propagation code normally has four main categories of operations: reading the input data, initializing a finite difference grid, performing calculations for each time increment at each grid point, and printing the computed information. The subroutine SHEAR2 is written to correspond with this organization; it has parts for reading data and initializing, for calculating stresses and damage, and for printing the results. The part of SHEAR2 to be used at each CALL is indicated by the parameter NCALL. NCALL can have the following values:

- 0 Read data, initialize, and choose the weighting distribution of crack orientations in the solid angles according to the value of NANG, which is read in the BFR array.
- 1 Read data and initialize only for one material.
- 2 Calculate only.
- 3 Calculate and print.
- 4 Print only.

For each material, SHEAR2 must be called once to read data and initialize variables. For the first of these calls, NCALL = 0; for subsequent ones, NCALL = 1. This CALL could appear anywhere in the initialization phase of the calculations; it occurs in INPUT3 of TOODY and in GENRAT of PUFF. These CALLS are placed so that the SHEAR2 data appear with the other data for the material. SHEAR2 can then be called for stress calculations alone, printing alone, or calculations and printing together. These latter CALLS should appear after the strain increment has been determined for each cell. In TOODY3, the second call is for calculation and printing and is within the loops over each cell and each time increment in the main program. In PUFF the computing and printing CALL is in HSTRESS, the subroutine that controls all stress calculations. There NCALL is normally set to 2, but on print cycles, NCALL is set to 3. The print CALL is made in conjunction with the computing CALL so that certain temporary variables that are computed can also be printed without the necessity of storing them.

The formal parameters of the subroutine are listed below in the order that they appear in the CALL statement:

SUBROUTINE SHEAR2 (NCALL, IN, M, K, J, IH3, SX, SY, SZ, SKY, P, TAU, DH, DOLD, DTO, EH, EOLD, EN, EMELT, EP, EX, EY, EZ, EXY, F, YHL, PLEN, ROT, DROT, ESC, CN).

Only the first three parameters are required for the calls in which NCALL = 0 or 1. The meaning of the parameters is given in Tables 3 and 4. Some parameters are further described in Section 4 of this Appendix.

## 2. Outline of the Subroutine

The subroutine is written in three parts for reading, computing stresses and damage, and printing. In the reading portion, the BFR and NSIZE arrays are read, NSIZT and the two sign factors SS and SSE are set, and the weighting factors FNUC are initialized.

In the second part, the stresses and damage are computed. First, the  $\tau_z$  array is constructed from the existing damage quantities. The  $\tau_z$  values are used to transform the external stresses and strains to internal values. Then new stresses are computed on an elastic basis. If yielding occurs, the equivalent plastic strain, plastic work, and plastic shear strains in each band orientation are computed. Then existing bands are allowed to grow in proportion to the plastic shear strain. If some strain remains after growth, nucleation of new bands is computed. Then  $\tau_z$  is recomputed. Finally the internal stresses are transformed back to the external sign convention and orientation. A special zero-stress route is provided if fragmentation has occurred.

The final part of the subroutine contains the printing. Printing occurs only if there has been some nucleation of shear bands in the cell. This output is described in Section 6 of the Appendix.

## 3. Descriptions of Parameters

All the formal parameters and input quantities are defined in Tables 3 and 4. The subroutine calculations and variable names closely follow the derivation in Chapter IV so that internal variables should be

Table 3

DEFINITION OF FORMAL PARAMETERS IN SHEAR2

NCALL	An indicator for the type of calculations required; see discussion in part 2 of this Appendix
IN	Data input file number (usually 5)
M	Material number
K	Cell number in the K direction
J	Cell number in the J direction
IH3	A damage indicator ( $20 \cdot \text{TAU} + 2.9$ ), output only; initialized at 2. Set to 25 at full separation.
SX	Deviator stress in the X direction ( $\text{dyn/cm}^2$ )
SY	Deviator stress in the Y direction ( $\text{dyn/cm}^2$ )
SZ	Deviator stress in the Z direction ( $\text{dyn/cm}^2$ )
SXY	Shear stress ( $\text{dyn/cm}^2$ )
P	Pressure calculated for the cell ( $\text{dyn/cm}^2$ )
TAU	Damage ( $\sum \text{NR}^3$ ) in the cell calculated on the last cycle; ranges from 0 to 1
DH	New incoming density ( $\text{g/cm}^3$ )
DOLD	Cell density determined on the last cycle ( $\text{g/cm}^3$ )
DTO	Time step (sec)
EH	Internal energy of the cell in the present cycle (erg/g)
EOLD	Energy of cell in previous cycle (erg/g)
EN	Total number of shear bands in the cell ( $\text{number/cm}^3$ )
EMELT	Value of internal energy at which material will melt
EP	Total effective plastic strain
EX	Strain increment in the X direction
EY	Strain increment in the Y direction
EZ	Strain increment in the Z direction

**EXY**            Tensor shear strain increment  
**F**                Thermal softening factor; varies from 0 to 1  
**YHL**            Yield value calculated on last cycle (remains unchanged  
(1) if the yield has not been exceeded, or (2) if it has  
been exceeded and work hardening is zero) (dyn/cm<sup>2</sup>)  
**PLEN**           Work devoted to plastic strain on previous cycle (erg/g)  
**ROT**            Total angle of cell rotation as of the previous cycle  
**DROT**           Additional angle of cell rotation since the last cycle  
**ESC**            Equation of state variables (array (6,20) must be dimen-  
sioned in the calling routine; some of the elements of this  
array are not used in SHEAR2)  
  
**ESC(M,1)**       Original density (g/cc)  
**ESC(M,2)**       Bulk modulus, C(dyn/cm<sup>2</sup>)  
**ESC(M,3),**  
**ESC(M,4)**       D and S in the pressure equation:  
  

$$P = C\mu + D\mu^2 + S\mu^3, \text{ where } \mu = DH/ESC(M,1) - 1.$$
  
**ESC(M,5)**       Shear modulus (dyn/cm<sup>2</sup>)  
**ESC(M,9)**       Gruneisen's ratio,  
  
**CN**             Array contains numbers of shear bands, band lengths, and  
other damage factors for each cell. The number of array  
elements required for each cell is  $2\sum NSIZE(i) + NANG$ ;  
array must be dimensioned in the calling routine.

Table 4

INPUT DATA FOR SHEAR2

BFR array	Nucleation and growth parameters for shear bands
BFR(M,22)	Growth coefficient, $C_G$
BFR(M,23)	Growth threshold, $\epsilon_{go}$ (unused)
BFR(M,24)	Nucleation size parameter, $R_n$ in the relation $N_g = N_o \exp(-R/R_n)$ (cm)
BFR(M,25)	Nucleation rate coefficient, $C_N$ ( $\text{sec}^2/\text{cm}^3$ )
BFR(M,26)	Nucleation threshold, $\epsilon_{no}$
BFR(M,27)	Ratio of displacement to band radius, b
BFR(M,28)	Maximum nucleation band size (cm)
BFR(M,29)	Ratio of successive intervals between band sizes
BFR(M,30)	Time constant for deviator stress relation, T (sec)
BFR(M,31)	Work hardening modulus, $Y_D$ ( $\text{dyn}/\text{cm}^2$ )
BFR(M,32)	Number of orientations used, NANG
BFR(M,33)	Thermal conductivity ( $\text{erg}/\text{sec}/\text{cm}^2$ ) (unused)
BFR(M,34)	Specific heat at constant volume ( $\text{erg}/\text{g}/^\circ\text{K}$ ) (unused)
BFR(M,35)	Critical internal energy required in the shear banding material to permit motion of the band, $E_{cr}$ ( $\text{erg}/\text{g}$ )
NSIZE array	Number of size groups for each orientation

identifiable. However, some additional description is given here of the parameters involved in the size groups and of the nucleation threshold.

$BFR(M,32) = NANG$  is the number of orientations that may contain shear bands. We have chosen six orientations for the present cylindrically symmetric and axisymmetric problems. In some problems fewer could be chosen if some orientations would not be activated because of symmetry. The six chosen are for bands whose planes are normal to the radial, circumferential, and axial directions, and at  $45^\circ$  between radial and circumferential, between radial and axial, and between circumferential and axial. Since only the latter three are active in the cylindrically symmetric cases,  $NSIZE$  was set to zero for the first three orientations. The direction of most interest is at  $45^\circ$  between radial and circumferential. Probably satisfactory results would be obtained for the cylinders if only that orientation were provided. Currently only six orientations are fully implemented in the subroutine. More are probably not needed until complete 3D problems are attempted.

In each orientation a number of size groups is provided. The number of size groups,  $NSIZE$ , should be large (say 8 or 10) if considerable detail is desired in the shear band size distribution for that orientation; however,  $NSIZE$  could be 2 or 3 for less important orientations. For all shear bands in a material there is a maximum band size for nucleation,  $BFR(M,28)$ . The choice of maximum band size should be larger than needed so that the results do not significantly depend on this choice. In a shear band calculation if  $NR^3$  from the largest size group is a small fraction of  $\sum NR^3$ , then the computed results are not dependent on the largest radius size selected.

The radii of the bands are initialized so that the ratio of successive intervals between radii is equal to  $BFR(M,29) = X$ , an input quantity. Then if the maximum radius is  $R_N = BFR(M,28)$ , the  $(N-1)^{th}$  radius is

$$R_{N-1} = R_N (1 - X^{N-1}) / (1 - X^N).$$

The values of NSIZE and BFR(M,29) should be coordinated to give an accurate treatment of the band size distribution. A small ratio of say 1.2 to 1.6 could be used with large values of NSIZE. A small NSIZE would require a large BFR(M,29) to span the range of radii.

The threshold plastic shear strain is BFR(M,26), the value of strain that must occur in each orientation before nucleation can begin there. The threshold does not apply to the equivalent plastic strain,  $\bar{\epsilon}^P$ , but it applies to each element of the tensor  $\epsilon_{\theta\theta}^{PS}$ . We note that  $\epsilon_{\theta\theta}^{PS}$  is only the shearing portion of the deviatoric plastic strain.

This shearing strain is obtained from the flow rule or proportionality between plastic strain rate and deviator stress.

$$d\epsilon_{ij}^P = \sigma'_{ij} d\lambda$$

By squaring this equation and summing contributions from all the ij combinations, we obtain

$$\sum d\epsilon_{ij}^P d\epsilon_{ij}^P = (d\lambda)^2 \sum \sigma'_{ij} \sigma'_{ij}$$

But these sums are proportional to the squares of the effective stress and strain quantities ( $\bar{\sigma}$  and  $\bar{\epsilon}^P$ ) defined in Equations 4 and 5.

Hence

$$d\lambda = d\bar{\epsilon}^P / \bar{\sigma}$$

so the flow rule can be written

$$d\epsilon_{ij}^P = d\bar{\epsilon}^P \frac{\sigma'_{ij}}{\bar{\sigma}} \quad \text{or} \quad d\epsilon_{ij}^{PS} = d\bar{\epsilon}^P \frac{\sigma'^S_{ij}}{\bar{\sigma}}$$

where  $\bar{\sigma}$  is the equivalent or von Mises shear stress and  $\sigma'^S_{ij}$  is the shearing component of the deviator stress. This shear component

is found by taking the vector difference between the total deviator  $S$  and the normal component  $S_n$ :

$$\sigma'_{ij} = \sqrt{S^2 - S_n^2}$$

In general,  $S$  and  $S_n$  are defined as

$$S = \left( S_x^2 + S_y^2 + S_z^2 \right)^{\frac{1}{2}}$$

$$S_n = l S_x + m S_y + n S_z$$

$$S_x = l \sigma_x + m \sigma_{yx} + n \sigma_{xz}$$

$$S_y = l \sigma_{xy} + m \sigma_y + n \sigma_{yz}$$

$$S_z = l \sigma_{xz} + m \sigma_{yz} + n \sigma_z$$

where  $\sigma_x, \sigma_y, \sigma_z, \sigma_{xy}, \sigma_{xz}, \sigma_{yz}$  are the stress tensor components and  $l, m, n$  are direction cosines to the plane of interest.  $S_x, S_y, S_z$  are  $x, y, z$  components of the stress acting on the plane. A standard mechanics text should be referred to for details of this transformation.

As a guide in selecting values of BFR(M,26) based on measured thresholds for  $\bar{\epsilon}^P$ , consider the case where  $d\epsilon_2 = -d\epsilon_1$  and  $d\epsilon_3 = 0$ . This strain configuration is approximated in the cylindrically symmetric calculations. For this case the shear strain at  $45^\circ$  between the directions 1 and 2 is  $d\epsilon_{12}^{PS} = d\bar{\epsilon}^P / \sqrt{3}$ . Hence, for an observed threshold of  $\bar{\epsilon}^P = 0.28$ , the appropriate value of BFR(M,26) is  $0.28 / \sqrt{3} = 0.16$ .

The major new material parameters are  $C_G, R_n, C_n, \epsilon_{no}$  and  $b$ ; each represents a well-defined physical process or quantity. From the present

computed results, it appears that  $C_n$  is the most important for determining the shape of the fragment size distribution.

#### 4. Transformations

As they enter the subroutine, all stress and strain quantities undergo two transformations--one in orientation and one in sign. The orientation transformation allows all computations in the subroutine to occur in a coordinate system that rotates with the material. (The shear band size groups and the cumulative plastic strain tensor also rotate with the material.) The sign transformation occurs so that the internal sign convention need not match the sign convention of the calling program.

Material rotation is provided by the calling program with two variables:  $\psi$  and  $\Delta\psi$  (positive counterclockwise). The  $\psi$  is cumulative and must be stored external to the subroutine. Transformations use the angle  $\psi' = \psi + \Delta\psi/2$ . Stresses are transformed from  $\sigma_x, \sigma_y, \sigma_z, \sigma_{xy}$  to the starred quantities inside the subroutine by the following equations:

$$\sigma_x^* = \frac{\sigma_x + \sigma_y}{2} + \frac{\sigma_x - \sigma_y}{2} \cos 2\psi' + \sigma_{xy} \sin 2\psi' \quad (36)$$

$$\sigma_y^* = \frac{\sigma_x + \sigma_y}{2} - \frac{\sigma_x - \sigma_y}{2} \cos 2\psi' - \sigma_{xy} \sin 2\psi' \quad (37)$$

$$\sigma_z^* = \sigma_z \quad (38)$$

$$\sigma_{xy}^* = -\frac{\sigma_x - \sigma_y}{2} \sin 2\psi' + \sigma_{xy} \cos 2\psi' .$$

At the end of the calculation the internal stresses are rotated back to the external configuration. The equations for this final transformation are the same as Eqs. 36 to 38 with the starred and unstarred quantities interchanged and  $\psi'$  changed to  $-\psi'$ .

The strain increments are also rotated to the material directions, and the same transformation equations are used for strain as for stress.

The sign transformation is made to account for a different sign convention. The internal convention is positive in compression for stress, pressure, and strain. If the convention matches the external one, SS and SSE (for stress and strain, respectively) are set to +1. If the external convention is that tension is positive, then the appropriate factor, SS or SSE is set to -1 in the DATA statement in SHEAR2. It is assumed that pressure is always positive in compression.

### 5. Output of the Subroutine

A sample of the output from the subroutine for four cells is given in Figure 40. This output is from a PUFF run with cylindrical symmetry in which orientations 4, 5, and 6 are activated. The parameters have the following meanings.

CN	Cumulative number of bands in an orientation. The bands at each radius are stored and used in computations, but the cumulative values are printed for ease in examining fragment size distributions.
CL	Shear band radius
TAUZ	$\sum NR^3$ in each orientation, summed over size groups
TAU	$\sum$ TAUZ summed over all orientations
EP	$\sum \Delta \bar{\epsilon}^P$ imposed on the material, summed over time.
Cumulative plastic strain	$\sum \Delta \epsilon_{\theta}^{PS}$ in each orientation, summed over time.
EN	Total number of shear bands in all orientations.
K, J	Coordinate designators, used for printout only.



## 6. Input Data

Four sets of input data are provided in Figure 41 as samples of the use of the subroutine SHEAR2. All were used with SRI PUFF8 in the one-dimensional cylindrical-symmetry mode.

In Shot 5084-3, the explosive pressure is simulated by an exponentially decaying pressure on the inner boundary. The expression used is  $P = P_6 \exp(T/T_6)$ , where  $P$  is applied pressure and  $T$  is time. The parameters  $P_6$  (initial pressure) and  $T_6$  (time constant) are given in the NAMELIST statement at the end of the deck. For Shot 5084-4, the low density PETN explosive is modeled by a pressure-volume relation given in tabular form. The two experiments of Crowe<sup>4</sup> contain COMP B explosive, which is treated by a polytropic gas law following a simultaneous detonation. Input units are in the dyn, cm, g, sec CGS system.

Each data set contains three parts. First is the general running and printing information including JCYCS and TS, the number of computational cycles, and the problem time at which the calculation is halted. In the second part, the data for each material is given. The EQST card contains the Mie-Grüneisen quantities  $C$ ,  $D$ ,  $E_{\text{sub}}$ ,  $\Gamma$ ,  $H$ , and  $S$  where  $C$ ,  $D$ , and  $S$  are the Hugoniot coefficients;  $E_{\text{sub}}$  is the sublimation energy; and  $\Gamma$  and  $H$  are Grüneisen's ratio in the solid and vapor states. The SH cards contain the 14 BFR numbers in order. Yield strength and shear modulus are on the YIELD card.

The layout of the materials and cells is handled in the final set of cards: NLayer is the number of layers, and JMAT gives the material number in each layer. After the NLayer card is a card for each layer describing the size and number of cells in that layer. In these samples the cell sizes are uniform in each layer.

## 7. Listing of SHEAR2

The subroutine SHEAR2 is listed in Figure 42.

```

IDENT FRAG RND FOR ERLICH-3
NTEDT = 0 NJEDIT = 2 NALPHA = 2
JEDITS = 1 3 5 7 9 11 12 13 14 15 18 22 27 30
JEDIT 2 S2,P,COM3, 1.1,1.3,1.5,1.7
NEDIT = 10 JCYCS = 300 CKS = 3.000E+01 TS = 8.000E-05
NMTRLS = 4 MATFL = -2 UZERO = 0 NSCRB = 0000111111
HF-1 SH BAND RHOS = 7.85E0 CFP = 030 DPY = 002 NVAR = 58 NCON = 0
EQST = 1.589E+12 5.170E+12 7.360E+10 1.69E0 0.25E0 5.170E+13
SHZ 3.000E+01 2.000E+00 1.100E+02 1.000E-03 0.17 0.070E+00 0.070E+00
1.4 3.000E-08 3.000E+08 6. .2 .17 7.000E+09
NSIZE 0 0 0 0 0 0 0 0 0 0
YIELD = 1.030E+10 8.190E+11
MELT = 1.085E+10 1.000E+08 0.E0 9.975E-01 1.000E-01
PMMA-BKR (BAKKER) RHOS = 1.184E+00 CFP = 000 DPY = 001
EQST = 7.000E+10 4.050E+11 1.000E+10 1.000E+00 2.500E-01 39640E+11
YIELD = 1.000E+06 1.950E+10 2.850E+09
HF-1 RHOS = 7.85E0 CFP = 000 DPY = 002 NCON = 0
EQST = 1.589E+12 5.170E+12 7.360E+10 1.69E0 0.25E0 5.170E+13
YIELD = 1.030E+10 8.190E+11
MELT = 1.085E+10 1.000E+08 0.E0 9.975E-01 1.000E-01
LEAD (KOMN) RHOS = 11.355 CFP = 000 DPY = 000
EQST = 5.000E+11 4.986E+11 9.155E+09 2.2 0.25 2.019E+12
NLAYERS = 5 JMAT = 0 1 2 3 4
NZONES = 1 5 CELLS IN 1.512E+00 INCH
NZONES = 1 5 CELLS IN 8.750E-01 INCH
NZONES = 1 5 CELLS IN 0.500E+00 INCH
NZONES = 1 10 CELLS IN 2.500E+00 INCH
NZONES = 1 5 CELLS IN 1.000E+00 INCH
EXTRA
SNLIST P6(1)=8).5E9,T6(1)=-1.36E-55

```

FIGURE 41 INPUT DATA FOR 4 CYLINDRICAL PUFF CALCULATIONS OF FRAGMENTING ROUNDS INCLUDING SHEAR BANDING

**THIS PAGE IS BEST QUALITY PRACTICABLE**

IDENT FRAG RND FOR ERLICH-4  
 NTEDT = 0 NJEDIT = 1 NALPHA = 2  
 JEDIT = 91.92.COM3: 2.1,2.3,2.5,2.7  
 NEDIT = 100 JCYS = 500 CFS = 3.000E+01 TS = 3.000E-04  
 NNTLS = 5 MATFL = 1 UZERO = 0. NSCWH = 000111111  
 PETN RHOS = 1.050E+00 CFP = 000 DPY = 060  
 EQST = 1.019E+11  
 IMAX = 21  
 RHO: P =

.100E+01	.801E+11	.794E+00	.300E+11	.633E+00	.103E+11
.500E+00	.114E+11	.390E+00	.725E+10	.316E+00	.469E+10
.291E+00	.309E+10	.200E+00	.207E+10	.154E+00	.140E+10
.126E+00	.967E+09	.100E+00	.675E+09	.754E-01	.477E+09
.633E-01	.341E+09	.800E-01	.845E+09	.300E-01	.102E+09
.316E-01	.130E+09	.291E-01	.960E+08	.200E-01	.711E+08
.199E-01	.530E+08	.126E-01	.397E+08	.100E-01	.299E+08

HF-1 SH BAND RHOS = 7.85E0 CFP = 030 DPY = 002 NVAR = 5R NCON = 0  
 EQST = 1.589E+12 5.170E+12 7.360E+10 1.69E0 0.25F0 5.170E+13  
 SH2 3.000E+01 .200E+00 1.100E-02 1.000E-03 0.17 0.070E+00 0.070E+00  
 1.4 3.000E-08 3.000E+08 6. .2 .17 7.000E+09  
 NSIZE 0 0 0 0 0 0  
 YIELD = 1.030E+10 8.190E+11  
 MELT = 1.085E+10 1.000E+08 0.E0 9.975E-01 1.000E-01  
 PMMA-RKB (HANKER) RHOS = 1.194E+00 CFP = 000 DPY = 001  
 EQST = 7.000E+10 4.050E+11 1.000E+10 1.000E+00 2.500E-01 39644E+11  
 YIELD = 1.000E+06 1.950E+10 2.850E+09  
 HF-1 RHOS = 7.85E0 CFP = 000 DPY = 002 NCON = 0  
 EQST = 1.589E+12 5.170E+12 7.360E+10 1.69E0 0.25E0 5.170E+13  
 YIELD = 1.030E+10 8.190E+11  
 MELT = 1.085E+10 1.000E+08 0.E0 9.975E-01 1.000E-01  
 LEAD (KOHN) RHOS = 11.355 CFP = 000 DPY = 000  
 EQST = 5.000E+11 4.906E+11 9.155E+09 2.2 0.25 2.019E+12  
 NLAYERS = 5 JMAT = 1 2 3 4 5  
 NZONES = 1 3 CELLS IN 1.512E+00 INCH  
 NZONES = 1 4 CELLS IN 8.750E-01 INCH  
 NZONES = 1 3 CELLS IN 1.125E+00 INCH  
 NZONES = 1 3 CELLS IN 2.500E+00 INCH  
 NZONES = 1 2 CELLS IN 1.000E+00 INCH  
 EXTRA  
 SNLIST U(2)=1.0+0.,1.0+0.,1.0+0.,1.0+0.,1.0+0.,1.0+0.

FIGURE 41 INPUT DATA FOR 4 CYLINDRICAL PUFF CALCULATIONS OF FRAGMENTING ROUNDS INCLUDING SHEAR BANDING (Continued)

THIS PAGE IS BEST QUALITY AVAILABLE  
 FROM COPY FURNISHED TO DDG

```

IDENT FR 4 FRAGMENT ROUND OF HF-1 TO SIMULATE CROWES TESTS 1 AND 2.
NTEDT = 0 NJEDIT = 1 NREZON = 0 NALPHA = 2
JEDIT = S1,S2,COM3, 2.1,2.3,2.5,2.7,2.9
NEDIT = 100 JCYCS = 300 CKS = 30.E0 TS = 4.00E-05
NMTRLS = 2 MATFL = 1 UZERO = 0.E0 NSCRH =
COMPU RHOS = 1.72E0 CFP = 000 DPY = 012
EQST = 1.E0 0.E0 1.E0 1.841E0 1.841E0
QEXPL = 4.469E+10
TENS = -1.000E+09 0.E0 -1.E0
MELT = -1.E0
HF-1 SH BAND RHOS = 7.85E0 CFP = 030 DPY = 002 NVAR = 58 NCON = 0
EQST = 1.589E+12 5.170E+12 7.360E+10 1.69E0 0.25E0 5.17E+13
SH2 3.000E+01 .200E+00 1.100E-02 1.000E-03 0.17 0.070E+00 0.070E+00
1.4 3.000E-08 3.000E+08 6. .2 .17 7.000E+09
NSIZE 0 0 0 8 8 0 0 0
YIELD = 1.030E+10 8.190E+11
MELT = 1.085E+10 1.000E+09 0.E0 9.975E-01 1.000E-01
NLAYERS = 2 JMAT = 1 2
NZONES = 1 10 CELLS IN 1.5 INCH
NZONES = 1 10 CELLS IN 8.750E-01 INCH

```

```

IDENT FR 5 FRAG ROUND OF ARMCO IRON TO SIMULATE CROWES TESTS 3 AND 4
NTEDT = 0 NJEDIT = 1 NREZON = 0 NALPHA = 2
JEDIT = S1,S2,S3,COM3, 2.1, 2.2, 2.3, 2.4, 2.5, 2.6, 2.7, 2.8, 2.9
NEDIT = 100 JCYCS = 300 CKS = 3.000E+01 TS = 4.000E-05
NMTRLS = 2 MATFL = 1 UZERO = 0.
COMPU RHOS = 1.72 CFP = 000 DPY = 012
EQST = 1. 0. 1. 1.841 1.841 0. 0.
QEXPL = 4.469E+10
TENS = -1.000E+09 0. -1.
MELT = -1.
ARMCO SH BAND RHOS = 7.85E0 CFP = 030 DPY = 002 NVAR = 58 NCON = 0
EQST = 1.589E+12 5.170E+12 7.360E+10 1.69E0 0.25E0 5.17E+13
SH2 3.000E+01 .200E+00 1.100E-02 3.000E-04 0.17 0.070E+00 0.070E+00
1.4 3.000E-08 3.000E+08 6. .2 .17 7.000E+09
NSIZE 0 0 0 8 8 0 0 0
MELT = 1.085E+10 6.460E+09 5.700E-01 7.000E-01 1.850E-01
YIELD = 2.000E+09 8.190E+11
NLAYERS = 2 JMAT = 1 2
NZONES = 1 10 CELLS IN 1.5 INCH
NZONES = 1 10 CELLS IN 0.75 INCH

```

FIGURE 41 INPUT DATA FOR 4 CYLINDRICAL PUFF CALCULATIONS OF FRAGMENTING ROUNDS INCLUDING SHEAR BANDING (Concluded)

THIS PAGE IS BEST QUALITY PRACTICABLE  
FROM COPY FURNISHED TO DDC





```

C*****
C          YIELD AND PLASTIC STRAIN CALCULATIONS
C*****
      EXPT = EXP(-DT0/BFR(M,30)/NSTEP)
      YEQ=(Y1+BFR(M,31)*SN/2./G2)/(1.+BFR(M,31)/2./G2)/SN
      DO 180 I=1,3
100    SE(I)=(ST(I)-P)*EXPT+(YEQ*SE(I)+BFR(M,30)*(SE(I)-ST(I)+P)/
      10TO*NSTEP)*(1.-EXPT)
      SE(4)=ST(4)*EXPT+(YEQ*SE(4)+BFR(M,30)*(SE(4)-ST(4))/DT0*NSTEP)*
      1(1.-EXPT)
      DO 200 I=1,3
200    DEP(I)=ES(I)-EBAR/NSTEP-(SE(I)-ST(I)+P)/G2
      DEP(4)=ES(4)-(SE(4)-ST(4))/G2
      DGAMMA=SQRT(1.5*(DEP(1)**2+DEP(2)**2+DEP(3)**2)+0.75*DEP(4)
      1**2)
      YHL=YHL+BFR(M,31)*DGAMMA
      DPLENR=((SE(1)-ST(1)-P)*DEP(1)+(SE(2)-ST(2)-P)*DEP(2)+(SE(3)-S
      1T(3)-P)*DEP(3)+(SE(4)-ST(4))*DEP(4))/2./DMN*AMAX1(0.,1.-IAU)
      DPLENR=ABS(DPLENR)
      EP=EP+DGAMMA
      PLEN=PLEN+DPLENR
C*****
C          COMPUTE PLASTIC STRAIN IN EACH ORIENTATION
C*****
      STR1=ABS(SE(4))
      STR2=ABS(SE(4))
      STR3=0.
      STR4=ABS(SE(1)-SE(2))/2.
      STR5=SQRT((SE(1)-SE(3))**2+2.*SE(4)**2)/2.
      STR6=SQRT((SE(2)-SE(3))**2+2.*SE(4)**2)/2.
      SN=SQRT(1.5*(SE(1)**2+SE(2)**2+SE(3)**2+2.*SE(4)**2))
      TEP(1)=DGAMMA/SN*STR1
      TEP(2)=DGAMMA/SN*STR2
      TEP(3)=DGAMMA/SN*STR3
      TEP(4)=DGAMMA/SN*STR4
      TEP(5)=DGAMMA/SN*STR5
      TEP(6)=DGAMMA/SN*STR6
C*****
C          GROWTH PROCESS
C*****
      NTOT=2*NSIZT(M)
      DO 250 I=1,NTOT
250    CNA(I)=CN(I)
      IF (EN .EQ. 0) GO TO 300
      JN=0
      DC=VMAX(M)*DT0/NSTEP
      DO 350 NG=1,NANG
      DGAM=0.
      IF (NSIZE(M,NG) .EQ. 0. .OR. CN(JN+1) .EQ. 0 .OR. TEP(NG) .LE. 0.)
      1 GO TO 345
      EXPE=EXP(BFR(M,22)*TEP(NG))
      NSIZE=NSIZE(M,NG)
      DO 300 I=1,NSIZE
      JN2=JN+2*(NSIZE(M,NG)+1-I)
      CLA(JN2)=AMINI(CN(JN2)*EXPE,CN(JN2)+DC)
300    NGAM=DGAM*CN(JN2-1)*3.14*BFR(M,27)*(CLA(JN2)**3-CN(JN2)**3)
      IF (DGAM .LE. TEP(NG)) GO TO 345
      RH=TEP(NG)/DGAM
      DCR=DC*RH
      FXPE=EXPE**RH
      NSIZE=NSIZE(M,NG)
      DO 340 I=1,NSIZE
      JN2=JN+2*(NSIZE(M,NG)+1-I)
      SHEAR2 126
      SHEAR2 127
      SHEAR2 128
      SHEAR2 129
      SHEAR2 130
      SHEAR2 131
      SHEAR2 132
      SHEAR2 133
      SHEAR2 134
      SHEAR2 135
      SHEAR2 136
      SHEAR2 137
      SHEAR2 138
      SHEAR2 139
      SHEAR2 140
      SHEAR2 141
      SHEAR2 142
      SHEAR2 143
      SHEAR2 144
      SHEAR2 145
      SHEAR2 146
      SHEAR2 147
      SHEAR2 148
      SHEAR2 149
      SHEAR2 150
      SHEAR2 151
      SHEAR2 152
      SHEAR2 153
      SHEAR2 154
      SHEAR2 155
      SHEAR2 156
      SHEAR2 157
      SHEAR2 158
      SHEAR2 159
      SHEAR2 160
      SHEAR2 161
      SHEAR2 162
      SHEAR2 163
      SHEAR2 164
      SHEAR2 165
      SHEAR2 166
      SHEAR2 167
      SHEAR2 168
      SHEAR2 169
      SHEAR2 170
      SHEAR2 171
      SHEAR2 172
      SHEAR2 173
      SHEAR2 174
      SHEAR2 175
      SHEAR2 176
      SHEAR2 177
      SHEAR2 178
      SHEAR2 179
      SHEAR2 180
      SHEAR2 181
      SHEAR2 182
      SHEAR2 183
      SHEAR2 184
      SHEAR2 185
      SHEAR2 186
      SHEAR2 187
      SHEAR2 188

```

FIGURE 42 LISTING OF SUBROUTINE SHEAR2 (Continued)

340	CLA(JN2)=AMIN1(CN(JN2)*EXPE,CN(JN2)+DCR)	SHEAR2	184
345	TEP(NG)=AMAX1(0.,TEP(NG)-DGAM)	SHEAR2	190
350	JN=JN+NSIZE(M,NG)*2	SHEAR2	191
360	CONTINUE	SHEAR2	192
	DO 365 NG=1,NANG	SHEAR2	193
365	CN(NTOT+NG)=CN(NTOT+NG)+TEP(NG)	SHEAR2	194
	C*****	SHEAR2	195
	C NUCLEATION PROCESS	SHEAR2	196
	C*****	SHEAR2	197
	TEPM=0.	SHEAR2	198
	DO 370 NG=1,NANG	SHEAR2	199
370	TEPM=AMAX1(TEPM,CN(NTOT+NG)+TEP(NG))	SHEAR2	200
	IF (TEPM .LT. BFR(M,26)) GO TO 500	SHEAR2	201
	JN=0	SHEAR2	202
	DO 450 NG=1,NANG	SHEAR2	203
	IF (NSIZE(M,NG) .EQ. 0) GO TO 450	SHEAR2	204
	IF (CN(NTOT+NG)+TEP(NG) .LT. BFR(M,26) .OR. TEP(NG) .LT. 1.E-5)	SHEAR2	205
	GO TO 450	SHEAR2	206
	DNQ=TEP(NG)*BFR(M,25)*FNUC(NG)*(DPLENR/DI0*NSTEP/BFR(M,35))**2	SHEAR2	207
	CNR=0.	SHEAR2	208
	NSIZEM=NSIZE(M,NG)	SHEAR2	209
	DO 440 I=1,NSIZEM	SHEAR2	210
	II=NSIZE(M,NG)+1-I	SHEAR2	211
	JNI=JN+2*II	SHEAR2	212
	IF (CLA(JNI) .NE. 0.) GO TO 420	SHEAR2	213
	CLA(JNI)=BFR(M,28)*(1.-BFR(M,29)**II)/(1.-BFR(M,29)**NSIZE(M,NG))	SHEAR2	214
	CN(JNI)=CLA(JNI)	SHEAR2	215
420	CNL=DNQ*EXP(-(CLA(JNI)+CN(JNI))/2./BFR(M,24))	SHEAR2	216
	JNN=JN+2*II-1	SHEAR2	217
	CNA(JNN)=CNL-CNR+CN(JNN)	SHEAR2	218
440	CNR=CNL	SHEAR2	219
	EN=EN+CNL	SHEAR2	220
450	JN=JN+NSIZE(M,NG)*2+JN	SHEAR2	221
470	CONTINUE	SHEAR2	222
	C*****	SHEAR2	223
	C COMPUTE TAU AND REFILL MAIN ARRAYS	SHEAR2	224
	C*****	SHEAR2	225
	TAU=0.	SHEAR2	226
	JN=0	SHEAR2	227
	IF (EN .EQ. 0.) GO TO 500	SHEAR2	228
	DO 490 NG=1,NANG	SHEAR2	229
	TAUZ(NG)=0.	SHEAR2	230
	IF (NSIZE(M,NG) .EQ. 0 .OR. CNA(JN+1) .EQ. 0.) GO TO 490	SHEAR2	231
	NSIZEM=NSIZE(M,NG)	SHEAR2	232
	DO 480 I=1,NSIZEM	SHEAR2	233
	JNN=JN+2*I-1	SHEAR2	234
	CN(JNN+1)=CLA(JNN+1)	SHEAR2	235
	CN(JNN)=CNA(JNN)	SHEAR2	236
480	TAUZ(NG)=TAUZ(NG)+CNA(JNN)*CLA(JNN+1)**3	SHEAR2	237
	TAU=TAU+TAUZ(NG)	SHEAR2	238
490	JN=JN+NSIZE(M,NG)*2	SHEAR2	239
	IF (TAU+VFR(M) .GE. 1.) GO TO 800	SHEAR2	240
500	CONTINUE	SHEAR2	241
	P=PE	SHEAR2	242
	DO 550 I=1,3	SHEAR2	243
550	ST(I)=SE(I)*P	SHEAR2	244
	ST(4)=SE(4)	SHEAR2	245
600	CONTINUE	SHEAR2	246
	C*****	SHEAR2	247
	C TRANSFORMATION TO GLOBAL ORIENTATION	SHEAR2	248
	C*****	SHEAR2	249

FIGURE 42 LISTING OF SUBROUTINE SHEAR2 (Continued)

ST(4)=ST(4)*AMAX1(0.,(1.-1.5*(TAUZ(1)-TAUZ(2)))*3.*TAUZ(4))*VFR(M)	SHEAR2	252
1 ) )	SHEAR2	253
ST(1)=ST(1)*AMAX1(0.,(1.-1.5*(TAUZ(1)+1.5*(TAUZ(4)+TAUZ(5)))*VFR(M)	SHEAR2	254
1 ) )	SHEAR2	255
ST(2)=ST(2)*AMAX1(0.,(1.-1.5*(TAUZ(2)+1.5*(TAUZ(4)+TAUZ(6)))*VFR(M)	SHEAR2	256
1 ) )	SHEAR2	257
ST(3)=ST(3)*AMAX1(0.,(1.-1.5*(TAUZ(3)+1.5*(TAUZ(5)+TAUZ(6)))*VFR(M)	SHEAR2	258
1 ) )	SHEAR2	259
P=(ST(1)+ST(2)+ST(3))/3.	SHEAR2	260
SA=(ST(1)+ST(2))/2.	SHEAR2	261
SB=(ST(1)-ST(2))/2.*COR-ST(4)*SOR	SHEAR2	262
SXY=((ST(1)-ST(2))/2.*SOR+ST(4)*COR)*SS	SHEAR2	263
SX=(SA+SB-P)*SS	SHEAR2	264
SY=(SA+SB-P)*SS	SHEAR2	265
SZ=(ST(3)-P)*SS	SHEAR2	266
IF (PE .GT. 0.) P=P*PE*TAU	SHEAR2	267
INH=20.*TAU*2.9	SHEAR2	268
IF (NCALL .GE. 3) GO TO 900	SHEAR2	270
RETURN	SHEAR2	271
C*****	SHEAR2	272
C COMPLETE SEPARATION	SHEAR2	273
C*****	SHEAR2	274
800 EMU=DM/ESC(M,1)=1.	SHEAR2	275
PH=EMU*(ESC(M,2)+EMU*(ESC(M,3)+EMU*ESC(M,4)))	SHEAR2	276
PE=PH*(1.-ESC(M,9)*(DM/ESC(M,1)-1.)/2.)*DM*ESC(M,9)*EM	SHEAR2	277
P=AMAX1(PE,0.)	SHEAR2	278
SX=0.	SHEAR2	279
SY=0.	SHEAR2	280
SZ=0.	SHEAR2	281
SXY=0.	SHEAR2	282
INH=25	SHEAR2	283
IF (NCALL .GE. 3) GO TO 900	SHEAR2	284
RETURN	SHEAR2	285
C * * * * *	SHEAR2	286
C	SHEAR2	287
C PRINT DAMAGE ARRAYS	SHEAR2	288
C	SHEAR2	289
C * * * * *	SHEAR2	290
900 IF (EN .EQ. 0.) RETURN	SHEAR2	291
PRINT 8000,K,J,INH,ROT,EN,TAU,EP	SHEAR2	292
JN=0	SHEAR2	293
DO 1000 NG=1,NANG	SHEAR2	294
NS=NSIZL(M,NG)*2	SHEAR2	295
IF (NS .EQ. 0 .OR. CN(JN+1) .EQ. 0.) GO TO 1000	SHEAR2	296
II=JN+NS-1	SHEAR2	297
CNA(II)=CN(II)	SHEAR2	298
IF (NS .LE. 2) GO TO 975	SHEAR2	299
DO 970 I=3,NS,2	SHEAR2	300
II=NS-I+JN	SHEAR2	301
970 CNA(II)=CN(II)+CNA(II-2)	SHEAR2	302
975 CONTINUE	SHEAR2	303
PRINT 8500,NG	SHEAR2	304
PRINT 9001,(CNA(JN+I),I=1,NS,2)	SHEAR2	305
PRINT 9002,(CN(JN+I),I=2,NS,2)	SHEAR2	306
8000 FORMAT(3H K=I5,3H J=I5,5H INH=I5,5H ROT=E10.3,4H EN=E10.3,	SHEAR2	307
1 5H TAU=E10.3,4H EP=E10.3)	SHEAR2	308
8500 FORMAT(4H NG=I5)	SHEAR2	309
9991 FORMAT(4H CNA=I8(E10.3,2X))	SHEAR2	310
9002 FORMAT(4H CN=I8(E10.3,2X))	SHEAR2	311
1000 JN=JN+NS	SHEAR2	312
NTOT=2*NSIZT(M)	SHEAR2	313
PRINT 9003,(CN(NTOT+I),I=1,NANG)	SHEAR2	314
9003 FORMAT(16H TOT PL STRAIN =6F10.3)	SHEAR2	315
PRINT 1480,(TAUZ(I),I=1,NANG)	SHEAR2	316
1480 FORMAT(6H TAUZ= 6F10.0)	SHEAR2	317
RETURN	SHEAR2	318
END	SHEAR2	319

FIGURE 42 LISTING OF SUBROUTINE SHEAR2 (Concluded)

## REFERENCES

1. D. A. Shockey et al., "A Computational Model for Fragmentation of Armor Under Ballistic Impact," Phase I - Final Report No. DAAD05-73-C-0025, U.S. Army Ballistic Research Laboratories, Aberdeen Proving Ground, Maryland (December 1973).
2. L. Seaman, D. A. Shockey, D. R. Curran, and R. E. Tokheim, "Development of a Shear Band Model for Fragmentation in Exploding Cylinders," Final Report No. N00178-74-C-0450, Naval Surface Weapons Center, Dahlgren, Virginia (August 1975).
3. T. W. Barbee et al., "Dynamic Fracture Criteria for Ductile and Brittle Metals," *J. Materials*, JMLSA, 7, 3, 393-401 (September 1972).
4. C. R. Crowe, W. H. Holt, W. Mock, and O. H. Griffin, "Dynamic Fracture and Fragmentation of Cylinders," Naval Surface Weapons Center Report NSWC/DL TR-3449, Dahlgren, VA. 22448 (November 1976).
5. M. Cowperthwaite and W. H. Zwisler, "TIGER Computer Program Documentation," SRI Final Report for Lawrence Livermore Laboratory, (January 1973).
6. G. R. Johnson, "Analysis of Elastic-Plastic Impact Involving Severe Distortions," *J. Appl. Mech.*, 439 (1976).
7. L. Seaman, T. W. Barbee, Jr., and D. R. Curran, "Dynamic Fracture Criteria of Homogeneous Materials," Technical Report No. AFWL-TR-71-156, Air Force Weapons Laboratory, Kirtland Air Force Base, New Mexico (December 1971).

DISTRIBUTION LIST

<u>No. of Copies</u>	<u>Organization</u>	<u>No. of Copies</u>	<u>Organization</u>
12	Commander Defense Technical Info Center ATTN: DDC-DDA Cameron Station Alexandria, VA 22314	5	Commander US Army Watervliet Arsenal ATTN: Dr. T. Davidson Dr. M. A. Hussain Dr. S. L. Pu Mr. D. P. Kendall Dr. John Underwood Watervliet, NY 12189
4	Director Defense Advanced Research Projects Agency ATTN: Tech Info Dr. Ernest F. Blase Dr. Bement Dr. Ray Gogolewski 1400 Wilson Boulevard Arlington, VA 22209	1	Commander US Army Aviation Research and Development Command ATTN: DRSAV-E P. O. Box 209 St. Louis, MO 63166
1	Deputy Assistant Secretary of the Army (R&D) Department of the Army Washington, DC 20310	1	Director US Army Air Mobility Research and Development Laboratory Ames Research Center Moffett Field, CA 94035
1	Commander US Army Materiel Development and Readiness Command ATTN: DRCMDM-ST 5001 Eisenhower Avenue Alexandria, VA 22333	1	Commander US Army Communications Research and Development Command ATTN: DRDCO-PPA-SA Fort Monmouth, NJ 07703
6	Commander US Army Armament Research and Development Command ATTN: DRDAR-TSS (2 Cys) J. D. Corrie R. J. Weimer J. Beetle E. Bloore Dover, NJ 07801	1	Commander US Army Electronics Research and Development Command Technical Support Activity ATTN: DELSD-L Fort Monmouth, NJ 07703
1	Commander US Army Armament Materiel Readiness Command ATTN: DRSAR-LEP-L, Tech Lib Rock Island, IL 61299	1	Commander US Army Harry Diamond Labs ATTN: DRXDO-TI 2800 Powder Mill Road Adelphi, MD 20783
1	Director, USA ARRADCOM Benet Weapons Laboratory ATTN: DRDAR-LCB-TL Watervliet, NY 12189		

DISTRIBUTION LIST

<u>No. of Copies</u>	<u>Organization</u>	<u>No. of Copies</u>	<u>Organization</u>
3	Commander US Army Missile Research and Development Command ATTN: DRDMI-R DRDMI-YDL Dr. Raymond Conrad Redstone Arsenal, AL 35809	4	Commander US Army Research Office ATTN: Dr. Hermann Robl Dr. E. Saibel Dr. George Mayer Dr. James Murray P. O. Box 12211 Research Triangle Park NC 27709
3	Commander US Army Mobility Equipment Research & Development Cmd ATTN: DRDME-WC DRSME-RZT STSBF-MW, Dr. J. Bond Fort Belvoir, VA 22060	1	Commander US Army Research and Standardization Group (Europe) Box 65 ATTN: Dr. B. Steverding Box 65 FBO NY 09510
1	Commander US Army Tank Automotive Research & Development Cmd ATTN: DRDTA-UL Warren, MI 48090	1	Commander US Army War College ATTN: Lib Carlisle Barracks, PA 17013
1	Director US Army TRADOC Systems Analysis Activity ATTN: ATAA-SL, Tech Lib White Sands Missile Range NM 88002	1	Commander US Army Command and General Staff College ATTN: Archives Fort Leavenworth, KS 66027
5	Commander US Army Materials and Mechanics Research Center ATTN: DRXMR-ATL Dr. E. Wright Mr. R. Shea DRXMR-H, Dr. D. Dandekar DRXMR-T, Mr. J. Mescall Watertown, MA 02172	1	Commander US Military Academy ATTN: Library West Point, NY 10996
		1	Office of Naval Research ATTN: Code 402 Department of the Navy Washington, DC 20360
		1	Commander Naval Research Laboratory ATTN: Code 2020, Tech Lib Washington, DC 20375

DISTRIBUTION LIST

<u>No. of Copies</u>	<u>Organization</u>	<u>No. of Copies</u>	<u>Organization</u>
7	Commander Naval Research Laboratory Engineering Materials Division ATTN: E. A. Lange G. R. Yoder C. A. Griffis R. J. Goode R. W. Judy, Jr. A. M. Sullivan R. W. Crooker Washington, DC 20375	6	Sandia Laboratories ATTN: Tech Lib Dr. A. L. Stevens Dr. Lee Davison Dr. W. E. Warren Dr. L. D. Bertholf Dr. Marlin Kipp Albuquerque, NM 87115
1	Commander Naval Research Laboratory Metallurgy Division ATTN: W. S. Pellini Washington, DC 20375	7	SRI International ATTN: Dr. George R. Abrahamson Dr. Donald R. Curran Dr. Donald A. Shockey Dr. Lynn Seaman Dr. R. Caligiuri Mr. D. Erlich Mr. R. Burback 333 Ravenswood Avenue Menlo Park, CA 94025
2	Commander Naval Surface Weapons Ctr ATTN: Mr. W. H. Holt Tech Lib Dahlgren, VA 22445		<u>Aberdeen Proving Ground</u> Dir, USAMSAA DRXSJ-D ATTN: DRXSJ-MP, H. Cohen Cdr, USATECOM ATTN: DRSTE-TO-F Dir, Wpns Sys Concepts Team, Bldg. E3516, EA ATTN: DRDAR-ACW
2	Commander Naval Surface Weapons Ctr ATTN: Dr. Robert Crowe Tech Lib Silver Spring, MD 20910		
1	AFOSR(Dr. Alan H. Rosenstein) 1400 Wilson Boulevard Arlington, VA 22209		
1	AFWL(Tech Lib) Kirtland AFB, NM 87117		
1	Director Lawrence Livermore Laboratory ATTN: Dr. M. L. Wilkins P. O. Box 808 Livermore, CA 94550		

USER EVALUATION OF REPORT

Please take a few minutes to answer the questions below; tear out this sheet and return it to Director, US Army Ballistic Research Laboratory, ARRADCOM, ATTN: DRDAR-TSB, Aberdeen Proving Ground, Maryland 21005. Your comments will provide us with information for improving future reports.

1. BRL Report Number \_\_\_\_\_

2. Does this report satisfy a need? (Comment on purpose, related project, or other area of interest for which report will be used.)

\_\_\_\_\_  
\_\_\_\_\_  
\_\_\_\_\_

3. How, specifically, is the report being used? (Information source, design data or procedure, management procedure, source of ideas, etc.) \_\_\_\_\_

\_\_\_\_\_  
\_\_\_\_\_

4. Has the information in this report led to any quantitative savings as far as man-hours/contract dollars saved, operating costs avoided, efficiencies achieved, etc.? If so, please elaborate.

\_\_\_\_\_  
\_\_\_\_\_

5. General Comments (Indicate what you think should be changed to make this report and future reports of this type more responsive to your needs, more usable, improve readability, etc.) \_\_\_\_\_

\_\_\_\_\_  
\_\_\_\_\_  
\_\_\_\_\_

6. If you would like to be contacted by the personnel who prepared this report to raise specific questions or discuss the topic, please fill in the following information.

Name: \_\_\_\_\_

Telephone Number: \_\_\_\_\_

Organization Address: \_\_\_\_\_

\_\_\_\_\_  
\_\_\_\_\_